Filtering Impulses in Dynamic Noise in The Presence of Large Measurement Noise

---

A Dissertation
Presented to
the Graduate School of
Clemson University

In Partial Fulfillment
of the Requirements for the Degree
Doctor of Philosophy
Electrical Engineering

---

by
Jungphil Kwon
August 2015

Accepted by:
Dr. Adam Hoover, Committee Chair
Dr. Ian Walker
Dr. Kumar Venayagamoorthy
Dr. Jacob Sorber

Abstract

This work considers the problem of filtering a system in which the dynamic noise occasionally has an impulse value that is an order of magnitude or more larger than its typical expected distribution. This is particularly challenging when the ratio of measurement noise to typical dynamic noise is large enough that the impulse dynamic noise cannot be easily distinguished from a large random occurrence of measurement noise. A new filter model is proposed using a multiple model approach in which one of the models is an impulse. The implementation of the model is demonstrated in a Kalman filter framework. Simulation results show the improvement of the new filter over existing methods across a range of measurement, typical, and impulse dynamic noises. The filter is then applied to three different problems: 2D human motion tracking using ultra-wideband (UWB) position measurements, power system state estimation on a coupled bus, and handling outlier measurement noise in UWB tracking. In each case the new filter demonstrates a 2-4% improvement over existing state-of-the-art techniques.

Acknowledgments

Many people have contributed my dissertation in different ways, but first I would like to sincerely thank my advisor, Dr. Adam Hoover. With his advices and cares, I was able to learn how to approach research topics in general and to successfully complete my PhD at Clemson. It was the miracle to me that I met you at the desperate moment of my life. I also want thank Dr. Ian Walker, Dr. Kumar Venayagamoorthy, and Dr. Jacob Sorber for serving as my committee members and providing valuable feedback on my dissertation. Finally, I like to thank my wife, Ye-Jin, for supporting me to continue PhD at Clemson. We have went throught many difficult situations together while doing PhD, so it is your PhD, too.

Table of Contents

List of Tables

List of Figures

Figure **Page**

List of Algorithms

Chapter 1

Introduction

This work considers the problem of filtering a system in which the dynamic noise occasionally has an impulse value that is an order of magnitude or more larger than its typical expected distribution. This is particularly challenging when the ratio of measurement noise to typical dynamic noise is large enough that the impulse dynamic noise cannot be easily distinguished from a large random occurrence of measurement noise. A new filter model is proposed using a multiple model approach in which one of the models is an impulse. The implementation of the model is demonstrated in a Kalman filter framework. Simulation results show the improvement of the new filter over existing methods across a range of measurement, typical, and impulse dynamic noises. The filter is also demonstrated on real ultra-wideband (UWB) position tracking data and simulated power system data, showing an improvement over existing methods. Finally, it is shown how the same idea can be applied to measurement noise to address the outlier measurement problem in UWB position tracking data, yielding a similar improvement.

The following example demonstrates the concept. The system in this example is position over time. The dynamic noise of the system is represented by variations in velocity. The importance of measurement noise and dynamic noise is demonstrated in the following figures. Figure 1.1 shows an example trajectory of the system and demonstrates two different levels of measurement noise. The measurement noise on the right is higher than the measurement noise on the left. Figure 1.2 shows a trajectory affected by a typical distribution of dynamic noise, visible as changes in the slope of the trajectory over time. The figure shows the same trajectory with two different amounts of measurement noise to emphasize that it is the *ratio* of measurement-to-dynamic noise that is

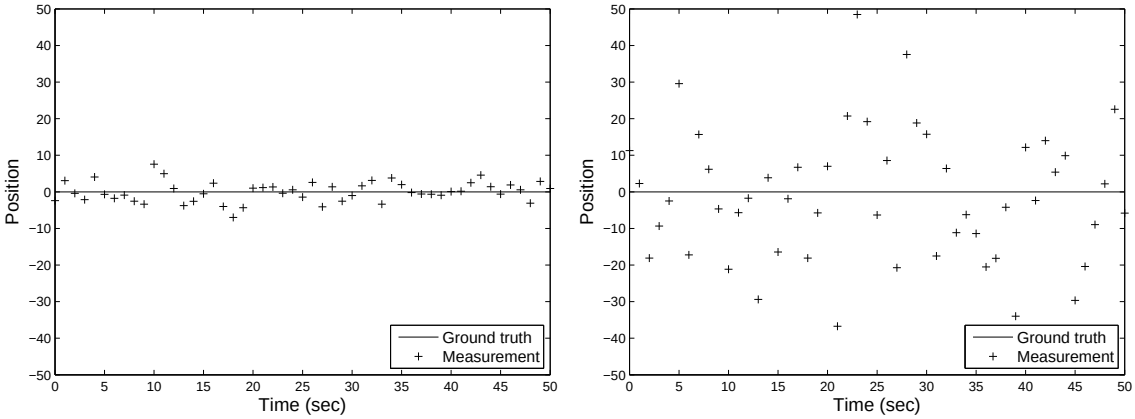

(a) Low measurement noise (b) High measurement noise

Figure 1.1: Measurement noise

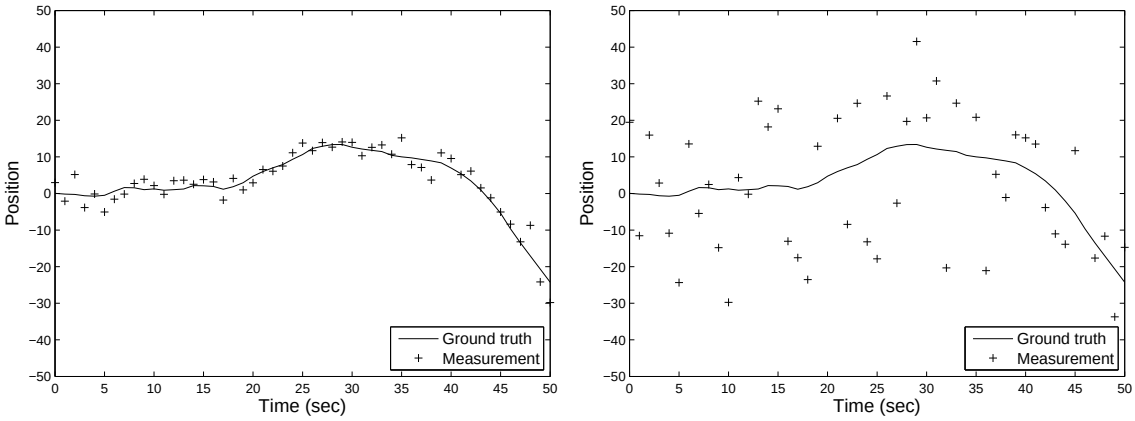

(a) Typical dynamic noise with low measurement noise (b) Typical dynamic noise with high measurement noise

Figure 1.2: Typical dynamic noise

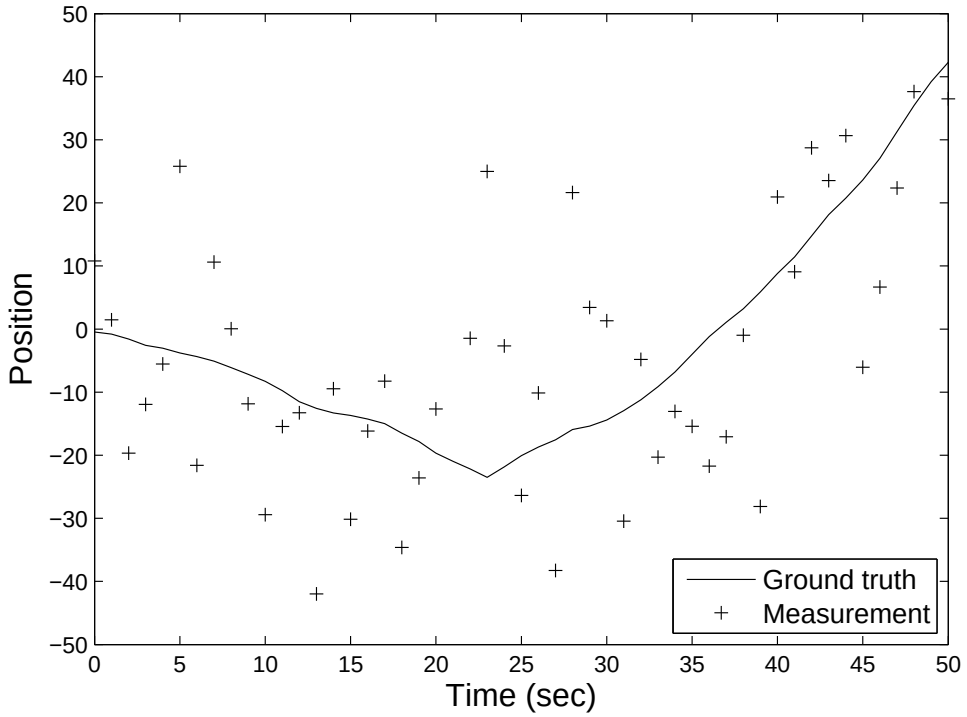

Figure 1.3: An impulse in dynamic noise in a system with large measurement-to-dynamic noise

important in designing a filter. Figure 1.3 demonstrates an occurrence of an impulse in dynamic noise, visible as a sudden larger change in trajectory. In the presence of a large ratio of measurement-to-dynamic noise, the impulse creates a unique challenge.

Figure 1.4a demonstrates filtering on this type of data. For most of the time, the dynamic noise is small enough that the slope of the data is changing very little, except at time 163 sec, when there is a large impulse of dynamic noise. Measurements are being taken every second and have relatively large measurement noise. The common solution to large measurement noise is to filter with a measurement-to-dynamic noise ratio that is large enough that the filter output exhibits strong smoothing, as shown in Figure 1.4b. Doing this however causes a delay in the presence of the impulse dynamic noise; in this case the filter output can be seen to lag after time 163 sec. Conversely, the measurement-to-dynamic noise ratio of the filter can be lowered so that the filter output responds more quickly, as in Figure 1.4c. However, in this case the benefit of smoothing the measurement noise is greatly reduced. The goal of this work is the development of a filter that behaves as shown in Figure 1.4d. This filter combines the effect of strong smoothing in the presence of a large measurement-to-dynamic noise ratio with the benefit of a quick response to an occasional

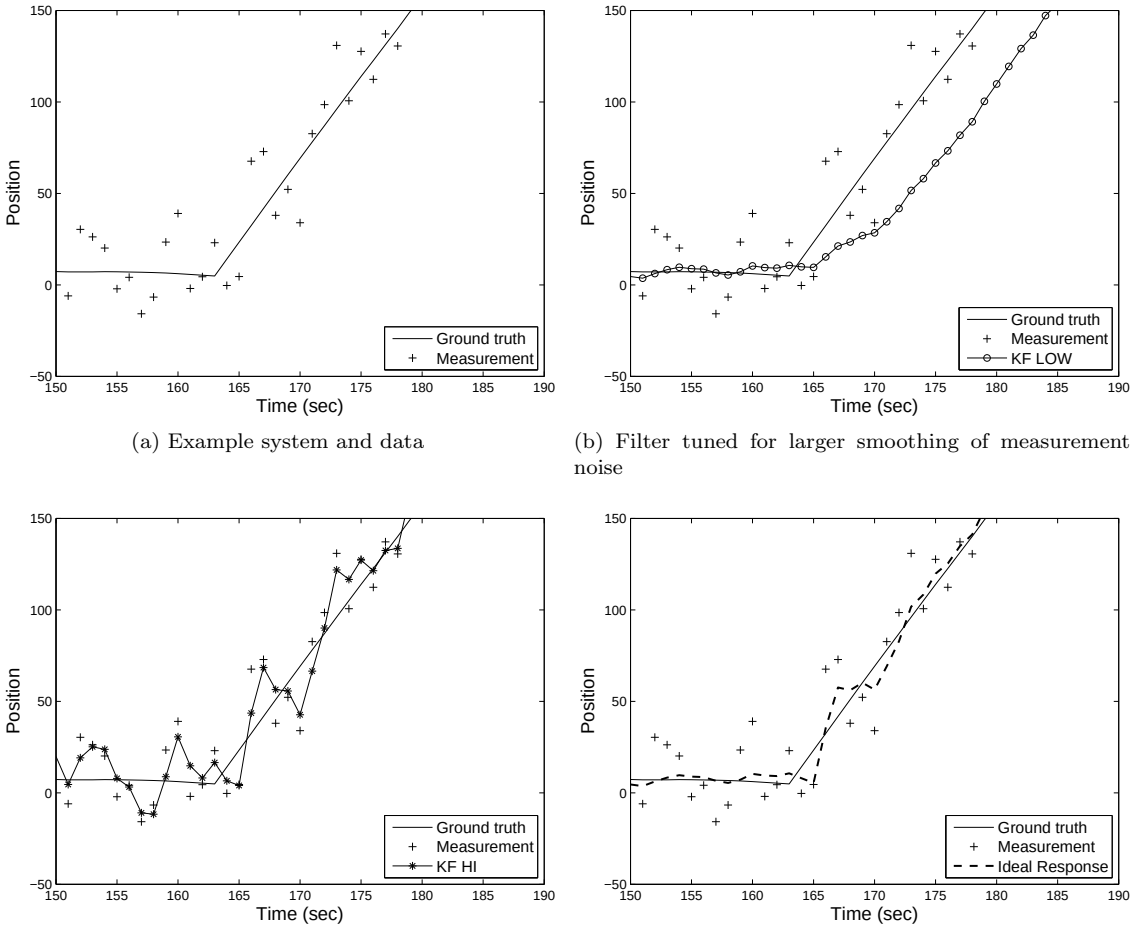

(a) Example system and data

(b) Filter tuned for larger smoothing of measurement noise

(c) Filter tuned for quicker response to dynamic noise

(d) Filter response sought in this work

Figure 1.4: An example problem showing a large ratio of measurement-to-dynamic noise at all times except t=163 sec when an impulse in dynamic noice occurs.

impulse in dynamic noise.

This work is motivated by the observation of human motion tracking using UWB sensing. The accuracy of UWB sensing in an indoor environment is typically in the range of 30-100 cm [62]. Normal human motion involves a typical dynamic motion where changes in velocity and direction of motion are relatively small, but with occasional impulse dynamic motion where acceleration is much larger. The latter occurs for example when a person starts or stops moving, or drastically changes direction. This work suggests modeling this type of system using a multiple-model filter where one model describes a lower range of typical dynamic noise, and a second model describes a higher range of impulse dynamic noise. The impulse in dynamics is assumed to happen with low frequency.

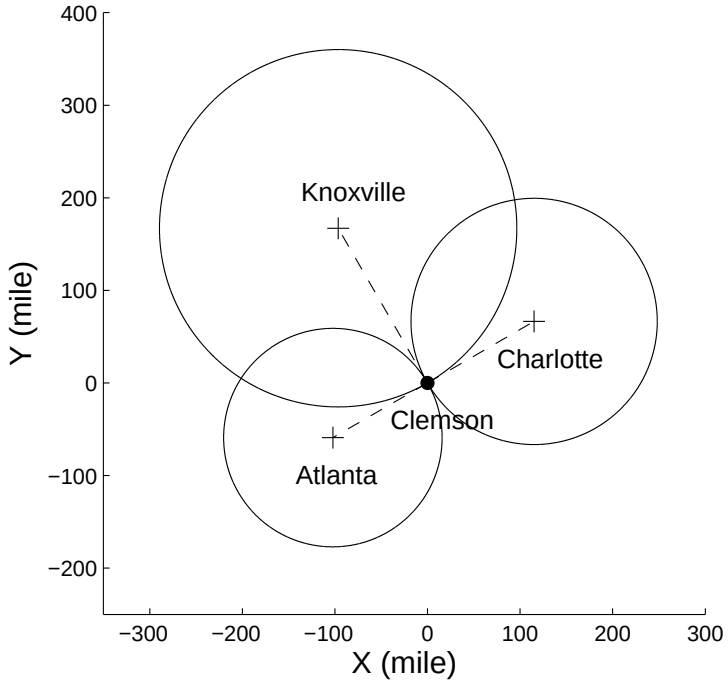

Figure 1.5: Example of trilateration to estimate position

The following sections provide background on related tracking systems that inspire this work, general filtering background, and previous works in filtering related to the proposed new method.

1.1 Global Navigation Satellite System

The type of tracking system that inspired this work is exemplified by a global navigation satellite system (GNSS). A GNSS is a multiple-satellite system which provides global position information to moving objects. The Global Positioning System (GPS) is the most famous GNSS, with others having since been developed by Russia, the European Union, and China [40]. A GNSS works by calculating ranges or distances from multiple satellites to a receiver and then finding an intersection point of 3D spheres placed on those satellites. This process is called multilateration. For example, Figure 1.5 shows trilateration, a type of multilateration in a two-dimensional space, using the positions of the cities around Clemson and their distances to Clemson. A range estimate between a satellite and a receiver is computed by multiplying the travel time of a radio frequency

(RF) signal from a satellite to a receiver by the speed of light [42]. In general, the travel time of the RF signal, also known as time of arrival (TOA), is used in range computations, but other quantities can be used to compute range estimates such as time difference of arrival (TDOA) or angle of arrival (AOA) and the overall processes are similar.

The intersection point of a multilateration is affected by errors in range estimates, which in turn can be caused by many different noise sources such as geometric satellite positions, clock errors, ephemeris errors, atmospheric distortion, relativistic effects, radio signal inferences, and multipath [40]. For example, line-of-sight is not guaranteed in a highly cluttered city area, and this non-line-of-sight condition affects the travel time of the RF signal from a satellite to a receiver and thus corrupts range estimates. The current GNSSs systematically model these noise sources and use various filter frameworks to mitigate measurement noise to improve the accuracy of position tracking [54].

Measurements from different types of sensors can be fused to improve position tracking accuracy. For example, in the differential GPS, a network of fixed ground-based reference stations can be used for range error corrections. The positions of the stations are precisely surveyed and are closer to the receiver, thus having less error in range estimates. The stations broadcast bias estimates of their surveyed locations relative to their GPS derived position estimates to receivers to help correct for errors in GPS position measurements [54]. Other types of sensors commonly fused with a GNSS include an inertial measurement unit (IMU) [56], gyroscope, mobile tower, and road map [15, 60, 63]. As a result of noise modeling and augmentations, the GNSS measurement accuracy has been improved to better than 1 m [57].

1.2 Ultra-wideband Position Tracking System

An ultra-wideband (UWB) position tracking system is a type of local positioning system (LPS). An LPS operates using the same basic principles as a GNSS, i.e. multilateration, but is intended to work in an indoor building-sized area. An LPS suffers from similar measurement noise sources as a GNSS, including non-line of sight (NLOS), multipath, and satellite constellation. It is expected that NLOS conditions and multipath effects will be more common than for a GNSS due to the nature of an indoor environment. Therefore, LPS transmitters should broadcast signals with enough power to be able to penetrate through any internal obstacles and then to be detected by LPS receivers. Several technologies have been investigated for indoor position tracking, such as

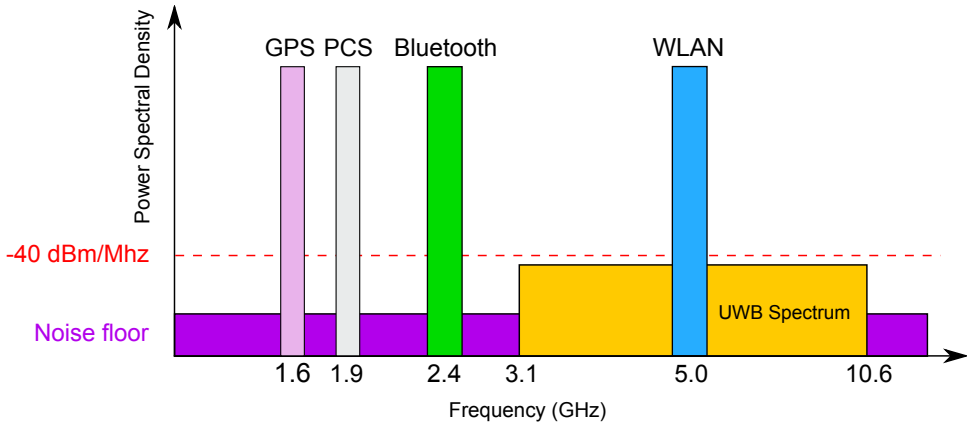

Figure 1.6: UWB signal frequency spectrum

RFID [58], Bluetooth [16], infrared, ultrasound, wireless local area network (WLAN) [73], and UWB [25, 44].

This work is inspired by UWB position tracking. UWB signals have a wide frequency spectrum as shown in Figure 1.6, making them more likely to penetrate internal obstacles with enough power for range estimation [41]. A UWB signal is a very short duration RF signal at low energy. Its usage has been extended from non-cooperative radar imaging to communication [74], sensor data collection, and precise position tracking. The U.S. Federal Communications Commission began regulating the use of UWB signals for public use in 2002 [22]. The power of a UWB signal is strictly limited at low level compared to other RF signals as shown in Figure 1.6 [27], to prevent it from interfering with other RF signals or wireless networks. Like a GNSS, a UWB position tracking system uses multilateration to compute position measurements, but the roles of a transmitter and receiver are switched. Specifically, a human to be tracked carries a transmitter called a tag, which periodically emits a UWB signal while moving, and then fixed multiple receivers detect the UWB signal and compute range estimates using TOA.

The sources of measurement noise in a UWB tracking system are very similar to those in a GNSS. However, at least three sources more prevalent and deserve some explanation. Figure 1.7 depicts NLOS and multipath measurement noise. Under the assumption that a direct path between a transmitter and receiver is established and UWB signals propagate through open space, the speed of light (299,792,458 m/s) can be used in range calculations. However, this assumption is violated by NLOS conditions, in which UWB signals have been propagated through wall or furniture which

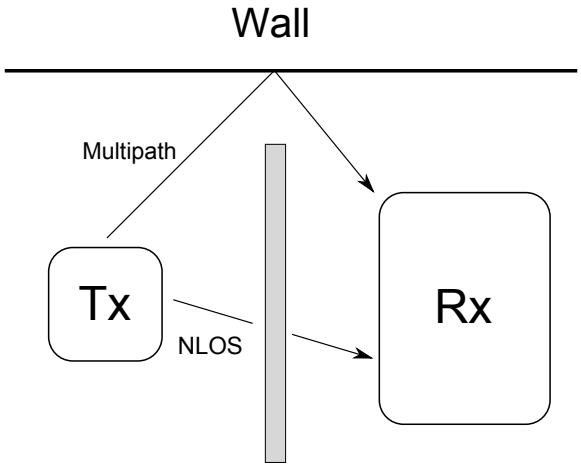

Figure 1.7: NLOS and multipath

attenuates the velocity according to the dielectric properties of the material. As a result, range estimates are affected by errors and UWB position measurements are also corrupted.

When NLOS conditions are present, reflected UWB signals, which propagated through an alternative path instead of a direct path, can also be detected by UWB receivers. The alternate path usually causes delay in the travel time of the UWB signals and therefore adds errors in range estimates. This noise source is called multipath.

Finally, a UWB system typically determines which range estimates to use from all its available receivers based upon received signal strength. This work makes use of a commercial UWB system produced by Ubisense Inc. This system selects the five UWB receivers with the strongest received signal strength. This *sensor set* is independently determined at each point in time (for each new position calculation). This allows the sensor set to change over time even when a target object stands still, causing a type of noise referred to as sensor set switching noise [5]. Figure 1.8 demonstrates the effect of sensor set switching noise in a two-dimensional space. It can be observed from the figure that even though the target object stands still, the UWB position measurements can appear to jump back-and-forth over time.

1.3 Filtering

Filtering is the process of estimating latent or unobservable states of a system from their indirect noisy measurements. Typically, there are two main equations in filtering, called a state

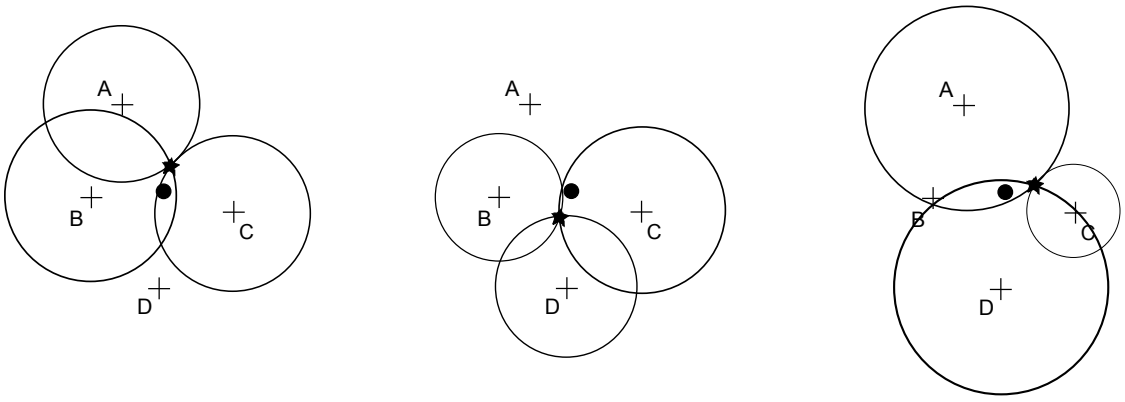

(a) time t (b) time $t+1$ (c) time $t+2$

Figure 1.8: UWB sensor set switching noise example. The true position of an object of interest is marked as the filled circle, and the position measurement from a UWB position tracking system is marked as the filled star. All the plus signs represent UWB receivers.

transition equation and measurement equation. A state transition equation describes how the state of a system can be expected to evolve over time. A measurement equation describes how indirect noisy measurements can be expected to be obtained from a given state. Note that these equations do not have to be perfect amalgams of the actual system behavior; filtering can tolerate approximate models, but more accurate models tend to yield more accurate filtering results. The following sections describe a filter model, recursive Bayesian filtering, the Kalman filter, and asynchronous Kalman filtering.

1.3.1 Filter Model

In filtering, a state represents any number of variables of interest in a system. They are traditionally written in a vector form. Equation 1.1 shows an example of a state vector at time t, $\mathbf{X}_t$, where x_t is a position and $\dot{x}_t$ is a velocity in a one-dimensional space.

$$\mathbf{X}_t = \begin{bmatrix} x_t \\ \dot{x}_t \end{bmatrix} \tag{1.1}$$

Another aspect of filtering is that it estimates a state vector with *uncertainty* (or degree of belief). This uncertainty is generally expressed as a probability distribution. A state vector with the highest probability in the distribution is the best estimate that a filtering process usually makes. For example, Figure 1.9 shows this concept when the probability distribution is a Gaussian, and $\hat{\mathbf{X}}_t$

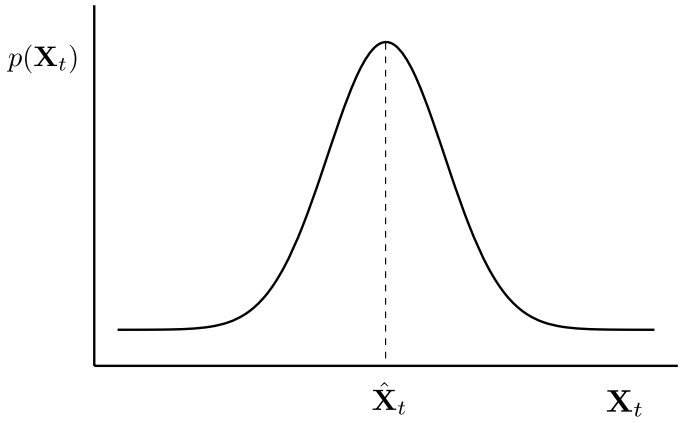

Figure 1.9: Gaussian distribution and its best estimate

is the best state vector estimate with the highest probability.

A state transition equation $\mathbf{f}(\cdot)$ can be possibly a time-varying, non-linear function of a state vector $\mathbf{X}_t$ and random dynamic noise vector $\mathbf{w}_t$ as shown in Equation 1.2 where $\mathbf{w}_t$ represents uncertainties in a state transition process.

$$\mathbf{f}_t(\mathbf{X}_t, \mathbf{w}_t) \tag{1.2}$$

If a constant velocity model is selected to describe state evolution in 1D position tracking, a state transition equation can be simplified to a time-invariant, linear function like Equation 1.3, where a random variable w_t represents acceleration uncertainty acting on a velocity $\dot{x}_t$ and Δt is a sampling interval. Their matrix form is also present in Equation 1.4, where Φ is called a state transition matrix.

$$\mathbf{f}(\mathbf{X}_t, \mathbf{w}_t) = \begin{bmatrix} x_t = x_{t-1} + \dot{x}_{t-1} \cdot \Delta t \\ \dot{x}_t = \dot{x}_{t-1} + w_t \end{bmatrix} \tag{1.3}$$

$$\mathbf{f}(\mathbf{X}_t, \mathbf{w}_t) = \Big[\mathbf{X}_t = \Phi \mathbf{X}_{t-1} + \mathbf{w}_t\Big] \tag{1.4}$$

$$\Phi = \begin{bmatrix} 1 & \Delta t \\ 0 & 1 \end{bmatrix} \tag{1.5}$$

$$\mathbf{w}_t = \begin{bmatrix} 0 \\ w_t \end{bmatrix} \tag{1.6}$$

Likewise, a measurement equation $\mathbf{g}(\cdot)$ can be possibly a time-varying, non-linear function of a state vector $\mathbf{X}_t$ and measurement noise vector $\mathbf{v}_t$ as shown in Equation 1.7 where $\mathbf{v}_t$ represents uncertainties in a measurement process.

$$\mathbf{g}_t(\mathbf{X}_t, \mathbf{v}_t) \tag{1.7}$$

If additive measurement noise to a position is assumed to describe a measurement process in 1D position tracking, then a measurement equation can be expressed by a time-invariant, linear function as shown in Equation 1.8, where a random variable v_t additively corrupts a position. Their matrix form is also present in Equation 1.9, where $\mathbf{H}$ is called an observation matrix.

$$\mathbf{g}(\mathbf{X}_t, \mathbf{v}_t) = \begin{bmatrix} z_t = x_t + v_t \end{bmatrix} \tag{1.8}$$

$$\mathbf{g}(\mathbf{X}_t, \mathbf{v}_t) = \begin{bmatrix} z_t = \mathbf{H}\mathbf{X}_t + \mathbf{v}_t \end{bmatrix} \tag{1.9}$$

$$\mathbf{H} = \begin{bmatrix} 1 & 0 \end{bmatrix} \tag{1.10}$$

$$\mathbf{v}_t = \begin{bmatrix} v_t \end{bmatrix} \tag{1.11}$$

1.3.2 Recursive Bayesian Filtering

A state estimation problem can be written in a general recursive form using Bayes' theorem [4]. Equation 1.12 shows the form, where $\mathbf{X}_{0:t}$ is a sequence of state vectors and $\mathbf{z}_{1:t}$ is a set of available measurements at time t. The left side of the equation represents a probability of a possible sequence of state vectors given all measurements at time t. The goal of this general problem is to

find the most probable sequence of state vectors, $\hat{\mathbf{X}}_{0:t}$.

$$p(\mathbf{X}_{0:t}|\mathbf{z}_{1:t}) = \frac{p(\mathbf{z}_t|\mathbf{X}_t)p(\mathbf{X}_t|\mathbf{X}_{t-1})}{p(\mathbf{z}_t|\mathbf{z}_{1:t-1})} p(\mathbf{X}_{0:t-1}|\mathbf{z}_{1:t-1}) \tag{1.12}$$

The goal of a filtering problem is to estimate the most probable state vector at time t given all measurements. Its recursive form is written in Equation 1.13 [4]. In filtering, the computation of $p(\mathbf{X}_t|\mathbf{z}_{1:t-1})$ is called the prediction process while the multiplication by $p(\mathbf{z}_t|\mathbf{X}_t)$ after the prediction is called the update process. Note that no assumptions are made in the derivation of Equation 1.13 which means that there are no restrictions on the distribution of a state vector and a system property, i.e. a linearity. Therefore, Equation 1.13 is applicable to any situations, but an analytical solution to a filtering problem is not always available.

$$\begin{aligned} p(\mathbf{X}_t|\mathbf{z}_{1:t}) &= \frac{p(\mathbf{z}_t|\mathbf{X}_t) \int p(\mathbf{X}_t|\mathbf{X}_{t-1}) p(\mathbf{X}_{t-1}|\mathbf{z}_{1:t-1}) d\mathbf{X}_{t-1}}{p(\mathbf{z}_t|\mathbf{z}_{1:t-1})} \\ &= \frac{p(\mathbf{z}_t|\mathbf{X}_t) p(\mathbf{X}_t|\mathbf{z}_{1:t-1})}{p(\mathbf{z}_t|\mathbf{z}_{1:t-1})} \end{aligned} \tag{1.13}$$

$$p(\mathbf{X}_t|\mathbf{z}_{1:t-1}) = \int p(\mathbf{X}_t|\mathbf{X}_{t-1}) p(\mathbf{X}_{t-1}|\mathbf{z}_{1:t-1}) d\mathbf{X}_{t-1} \tag{1.14}$$

1.3.3 Kalman Filter

The Kalman filter [37] provides the optimal state vector estimate upon a new measurement under the assumption that all the distributions in Equation 1.13 are Gaussian and the system holds a linearity condition [4], i.e. the state transition and measurement equations are linear and time-invariant. In the Kalman filter, filtering is simplified to updates of a mean and covariance of a state vector since the state vector lies on a Gaussian distribution which can be fully characterized by a mean and covariance, and a linear transform of a Gaussian random variable is also normally distributed.

Specifically, the Kalman filter provides the optimal state vector estimate by balancing a predicted state vector and measurement based on their corresponding covariances. This is usually accomplished in two phases, called a prediction and update. Assume that an initial state vector $\mathbf{X}_0$ and its covariance $\mathbf{P}_0$ are known. At time $t-1$, the optimal state vector estimate $\hat{\mathbf{X}}_{t-1}$ and its covariance $\hat{\mathbf{P}}_{t-1}$ are estimated from the Kalman filter, and filtering at time t with a new measurement

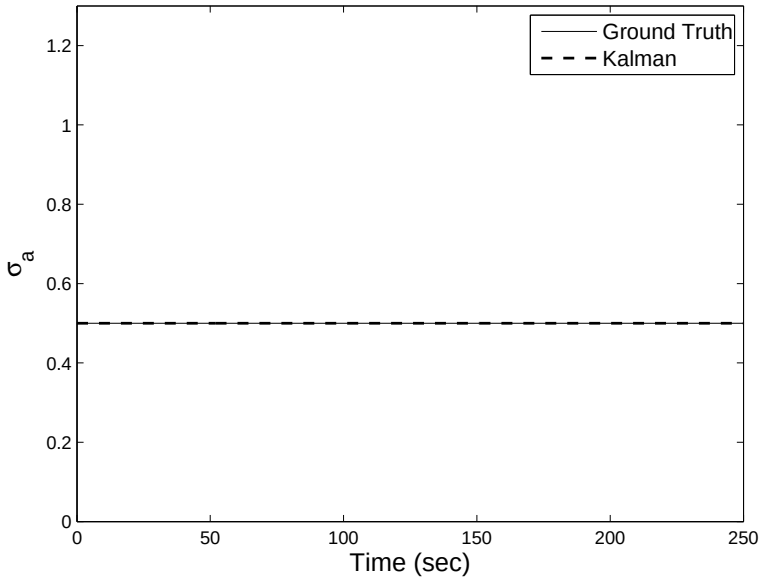

Figure 1.10: Dynamic noise

$\mathbf{z}_t$.

In a prediction phase, the Kalman filter first computes a predicted state vector $\hat{\mathbf{X}}_t^-$ and its covariance $\hat{\mathbf{P}}_t^-$ as shown in Equation 1.15, where $\mathbf{Q}$ is a covariance matrix of a random dynamic noise vector $\mathbf{w_t}$ and is a user-specified parameter. The standard deviation of this dynamic noise remains fixed throughout the filtering as shown in Figure 1.10.

$$\begin{aligned} \hat{\mathbf{X}}_t^- &= \Phi\hat{\mathbf{X}}_{t-1} \\ \hat{\mathbf{P}}_t^- &= \Phi\hat{\mathbf{P}}_{t-1}\Phi^{\mathrm{T}} + \mathbf{Q} \end{aligned} \tag{1.15}$$

In an update phase, a Kalman gain is computed using Equation 1.16 where $\mathbf{R}$ is a covariance matrix of a measurement noise vector $\mathbf{v}_t$ and it is another user-specified parameter. The Kalman gain determines the balance between a predicted state vector and measurement. For example, if a Kalman gain is small, the Kalman filter credits a predicted state vector more, and if a Kalman gain is large, the Kalman filter credits a measurement more.

$$\mathbf{K}_t = \hat{\mathbf{P}}_t^-\mathbf{H}^{\mathrm{T}}[\mathbf{H}\hat{\mathbf{P}}_t^-\mathbf{H}^{\mathrm{T}} + \mathbf{R}]^{-1} \tag{1.16}$$

Lastly, Equation 1.17 shows the update rule of the optimal state vector estimate and its

covariance at time t. It is worth noting that $\mathbf{z}_t - \mathbf{H}\hat{\mathbf{X}}_t^-$, which is called an *innovation* or *residue*, and its covariance shown in Equation 1.18 are the important components in the multiple-model filter theories [48, 51], which will be explained later.

$$\begin{aligned} \hat{\mathbf{X}}_t &= \hat{\mathbf{X}}_t^- + \mathbf{K}_t(\mathbf{z}_t - \mathbf{H}\hat{\mathbf{X}}_t^-) \\ \hat{\mathbf{P}}_t &= [\mathbf{I} - \mathbf{K}_t\mathbf{H}]\hat{\mathbf{P}}_t^- \end{aligned} \tag{1.17}$$

$$\mathbf{C}_t = \mathbf{H}\hat{\mathbf{P}}_t^-\mathbf{H}^{\mathrm{T}} + \mathbf{R} \tag{1.18}$$

The Kalman filter guarantees the optimal state vector estimate only when all distributions are Gaussian and state transition and measurement equations are linear. If any of these assumptions are violated, the Kalman filter no longer provides the optimal state vector estimate and its state vector estimate might diverge at the worst case scenario.

The extended Kalman filter (EKF) can handle a non-linearity in state transition and measurement equations by linearizing them at the most recent state vector estimate using a Jacobian matrix [70]. The unscented transform Kalman filter (UKF) is another method, which can handle a non-linearity, and it uses representative samples of a distribution to overcome a non-linearity in state transition and measurement equations and to directly compute a mean and covariance of a distribution [36]. However, the EKF and UKF also break down if any of the distributions in Equation 1.13 are not Gaussian or if state transition and/or measurement equations are intractable.

1.3.3.1 Asynchronous Kalman Filter

The implementation of a Kalman filter is simplified when a constant sampling interval is assumed. The UWB system used for experiments in this work has a nominal sampling rate of approximately 10 Hz, but due to various sources of measurement noise it occasionally operates at irregular intervals. Figure 1.11 shows a histogram of sampling intervals of the system, which were recorded during 37 minutes of operation using one transmitter. As shown in the figure, the nominal sampling rate is most commonly achieved but other sampling rates sometimes occur. Therefore this work implements an asynchronous Kalman filter.

The sequential steps of the asynchronous Kalman filter are the same as the Kalman filter

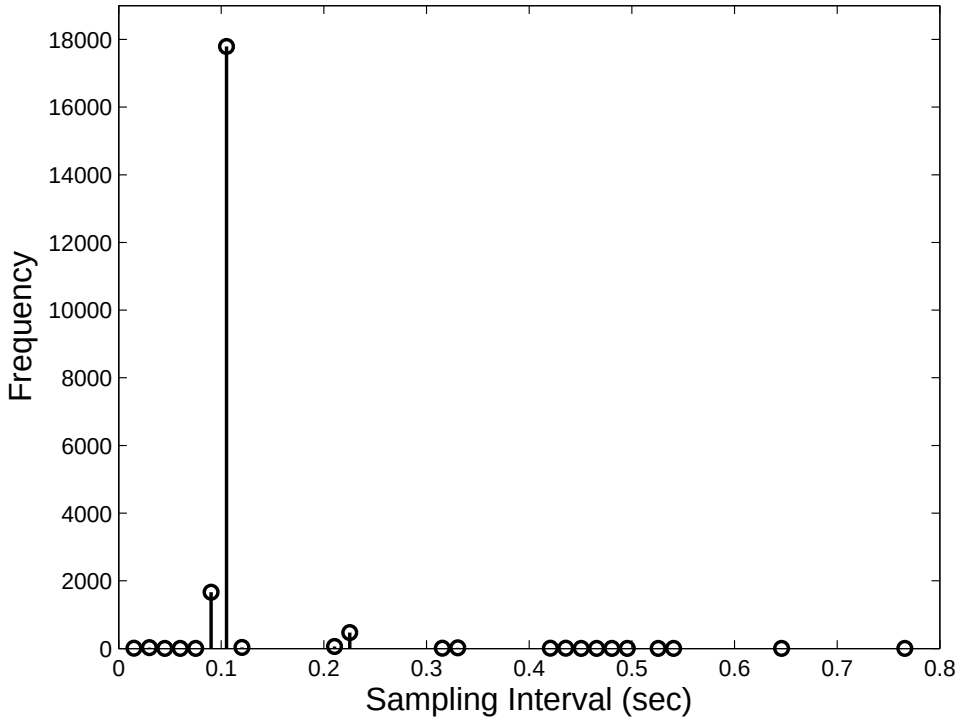

Figure 1.11: Ubisense sampling interval histogram (37 min)

except that the state transition matrix Φ_t and dynamic covariance matrix $\mathbf{Q}_t$ are now functions of the sampling interval Δt and therefore they have to be computed at each iteration. For example, if a constant velocity model is selected to describe state evolution in 1D position tracking as in Equation 1.3, Φ_t and $\mathbf{Q}_t$ can be computed using Equation 1.19 and Equation 1.20, respectively [5]. $\mathbf{Q}'$ in Equation 1.20 represents a base covariance matrix constructed using a random dynamic variable w_t in asynchronous filtering. The detailed derivation of the asynchronous Kalman filter can be found in multiple references [5, 18].

$$\Phi_t = \begin{bmatrix} 1 & \Delta t \\ 0 & 1 \end{bmatrix} \tag{1.19}$$

$$\mathbf{Q}_t = \begin{bmatrix} \Delta t^3/3 & \Delta t^2/2 \\ \Delta t^2/2 & \Delta t \end{bmatrix} \mathbf{Q}' \tag{1.20}$$

$$\mathbf{Q}' = \begin{bmatrix} \sigma_w^2 & 0 \\ 0 & \sigma_w^2 \end{bmatrix} \tag{1.21}$$

1.4 Time-varying noise distribution

As illustrated in Figure 1.10, the basic Kalman filter assumes that the standard deviation of the distribution of dynamic noise (and of the measurement noise) remains constant. In general, there are two approaches that relax this constraint: the adaptive Kalman filter (AKF) and the multiple model Kalman filter (MMKF). Figure 1.12a shows the basic control flow for the AKF. It directly estimates the ratio of dynamic noise to measurement noise at each iteration. It starts with an initial guess as to the proper value, but learns the actual value while operating. Figure 1.12b shows the basic control flow for the MMKF. It uses multiple a priori defined models where each model can use a different ratio of measurement-to-dynamic noise. It either selects one of the filters as the most likely or combines them in a weighted estimate at each iteration.

Figure 1.13a illustrates how the AKF can adapt its standard deviation of dynamic noise at each iteration. At times 50, 100, 150 and 200, the system changes its dynamic noise to an unknown value. The AKF will observe this in the innovation and recalculate the dynamic noise covariance in the filter [50]. Note that the dynamic noise can take any value in this scenario. Figure 1.13b illustrates how the MMKF can adapt its standard deviation of dynamic noise at each iteration. Again, at times 50, 100, 150 and 200, the system changes its dynamic noise but in this illustration it is to one of two possible values, both of which were known a priori and used to formulate the two models. Note that both of these approaches show a lag in the adjustment of the filter's dynamic noise as compared to the actual system.

1.4.1 Applications

The AKF is commonly used in GPS/INS navigation applications where the unavoidable bias error of an INS sensor measurement is mitigated using occasional GPS position updates. There have been many different AKF algorithms depending on adaptation criteria and targets. Mehamed, et al. [51] proposed one AKF algorithm which maximizes the maximum likelihood criterion. It directly estimates a dynamic noise covariance or measurement noise covariance. Hu, et al [31] presented two AKF algorithms focusing on the adaptation of a dynamic noise covariance. One weights a

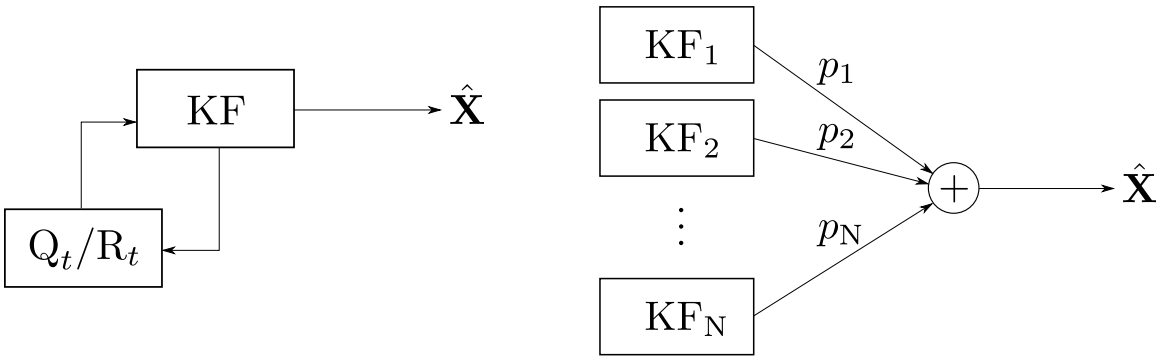

(a) Adaptive Kalman filter (b) Multiple-model Kalman filter

Figure 1.12: Flow diagrams for filtering time-varying noise

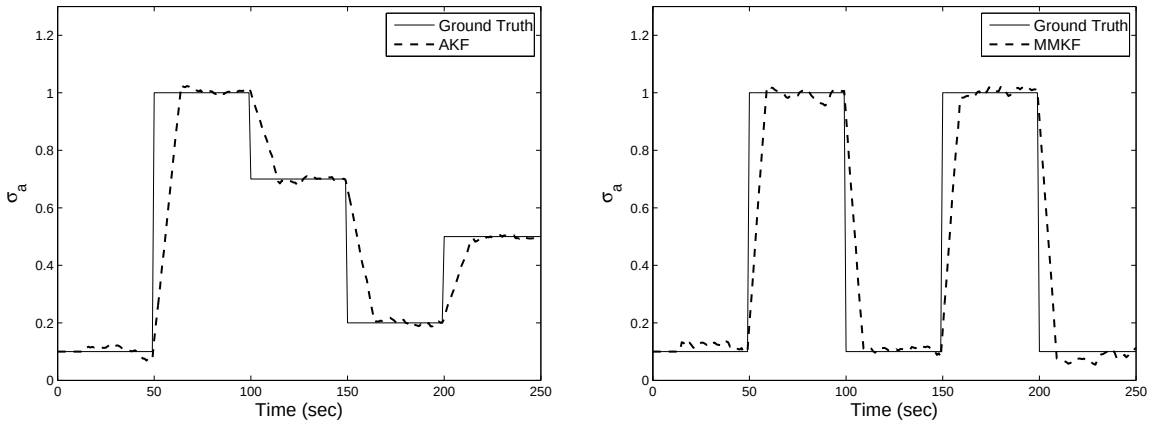

(a) Adaptive Kalman filter (b) Multiple-model Kalman filter

Figure 1.13: Two approaches to time-varying dynamic noise

pre-determined dynamic noise covariance based on the discrepancy between the theoretical and sample innovation covariances, and the other directly estimates a dynamic noise covariance using a Gauss-Markov model. Ding, et al. [17] developed another version of the AKF which weights a pre-determined dynamic noise in a similar way to [31].

The MMKF has been the mainstream approach in maneuvering target tracking [43]. Many different MMKF algorithms have been developed. The autonomous multiple model (AMM) is the first generation of the MMKF algorithm [43, 46]. The AMM assumes that a unique model of a target system is unknown, and this uncertainty is handled by calculating model probabilities of multiple models and combining state estimates from those multiple models based on their probabilities. Ackerson, et al, [2] proposed the first order generalized pseudo Bayesian (GPB1) algorithm which extends the AMM by including the Markov transition model and reinitializing each model filter with a combined state vector estimate from a previous iteration. The GPB1 was further extended to the second order (GPB2) [13] by Chang, et al. The interacting multiple model filter (IMMF) is an intermediate between GPB1 and GPB2, and it individually reinitializes each model filter in a process called mixing [9]. Extensions to the particle filter were also suggested by many researchers [10, 28, 34, 49].

In GPS/INS navigation, the GPS and INS have complementary characteristics where the GPS provides accurate position updates but runs at a low sampling rate while the INS provides real-time position updates but accrues cumulative measurement error over time. Using the Kalman filter with GPS position updates and INS sensor's statistics, i.e. measurement noise covariance, a large bias error of an INS sensor measurement can be estimated and compensated to compute better position estimates during the period of loss of GPS satellite signals. However, the INS sensor's statistics are hard to estimate in advance and are even subject to change over time, and therefore, many researchers have developed an adaptive Kalman filter to handle this issue [3, 17, 29, 51].

Kim, et al [38] applied the MMKF approach in maneuvering vehicle tracking where the constant velocity model and constant-speed turn model are implemented in the filter to track vehicles. Barrios, et al [7] used multiple state transition models to predict vehicle locations. Dyckmanns, et al [19] suggested to use the MMKF approach to predict vehicle positions at an intersection. El Mokhtari, et al [20] used the multiple-model filter to estimate vehicle information and ultimately to perform a map matching. Jordan, et al [35] implemented the multiple-model filter to estimate a vehicle mass.

Farmer, et al [21] used the multiple-model filter to track human motion in a car for the airbag suppression system. Isard, et al [34] proposed to use the particle filter version of the multiple-model filter to track a bouncing ball and switch between different hand drawing motions.

Weng, et al [71] implemented the concept of multiple model filtering in video object tracking by changing the dynamic noise and measurement noise covariances depending on the occlusion rate of a tracking object in a scene. Yu, et al [75] also implemented the concept of multiple model filtering in such a way that the dynamic noise covariance of the Kalman filter switches between two pre-determined values using a statistical hypothesis test called T-test to detect a power harmonic injection.

1.4.2 Adaptive Kalman Filter

The sequential steps of the AKF algorithm developed by Mehamed, et al. [51] are presented in this section. In the results, the performance of this filter is compared against the one newly developed in this work. Like the Kalman filter, the AKF starts with a prediction of a state vector and its covariance as shown in Equation 1.22. It then computes a Kalman gain based on Equation 1.23 and updates a state vector estimate and its covariance using a new measurement as shown in Equation 1.24. Note that unlike the Kalman filter, a computation of an innovation $\mathbf{i}_t$ is formally added to an update phase (Equation 1.24) and it is defined as the difference between the predicted and actual measurements.

$$\begin{aligned} \hat{\mathbf{X}}_t^- &= \Phi\hat{\mathbf{X}}_{t-1} \\ \hat{\mathbf{P}}_t^- &= \Phi\hat{\mathbf{P}}_{t-1}\Phi^{\mathrm{T}} + \mathbf{Q} \end{aligned} \tag{1.22}$$

$$\mathbf{K}_t = \hat{\mathbf{P}}_t^-\mathbf{H}^{\mathrm{T}}[\mathbf{H}\hat{\mathbf{P}}_t^-\mathbf{H}^{\mathrm{T}} + \mathbf{R}]^{-1} \tag{1.23}$$

$$\begin{aligned} \hat{\mathbf{X}}_t &= \hat{\mathbf{X}}_t^- + \mathbf{K}_t(\mathbf{z}_t - \mathbf{H}\hat{\mathbf{X}}_t^-) \\ \hat{\mathbf{P}}_t &= [\mathbf{I} - \mathbf{K}_t\mathbf{H}]\hat{\mathbf{P}}_t^- \\ \mathbf{i}_t &= \mathbf{z}_t - \mathbf{H}\hat{\mathbf{X}}_t^- \end{aligned} \tag{1.24}$$

In the last step the AKF executes an adaptation phase. During this phase, the AKF first computes a sample innovation covariance $\hat{\mathbf{C}}$ using the last W innovation samples as shown in Equation 1.25, where W is a window size and is an user-specified parameter. Finally, the AKF estimates a dynamic noise covariance $\hat{\mathbf{Q}}$ or measurement noise covariance $\hat{\mathbf{R}}$. Their adaptation equations are shown in Equation 1.26 and Equation 1.27, respectively. The positive semi-definite form of the measurement covariance adaptation equation is also shown in Equation 1.28 [69].

$$\hat{\mathbf{C}} = \frac{1}{\mathrm{W}} \sum_{t'=t-\mathrm{W}+1}^{t} \mathbf{i}_{t'} \mathbf{i}_{t'}^{\mathrm{T}} \tag{1.25}$$

$$\begin{aligned} \hat{\mathbf{Q}} =& \mathbf{K}_t \hat{\mathbf{C}} \mathbf{K}_t^{\mathrm{T}} \\ \hat{\sigma}_a =& \sqrt{\hat{\mathbf{Q}}} \end{aligned} \tag{1.26}$$

$$\begin{aligned} \hat{\mathbf{R}} =& \hat{\mathbf{C}} - \mathbf{H} \hat{\mathbf{P}}_t^{-} \mathbf{H}^{\mathrm{T}} \\ \hat{\sigma}_m =& \sqrt{\hat{\mathbf{R}}} \end{aligned} \tag{1.27}$$

$$\hat{\mathbf{R}} = \hat{\mathbf{C}} + \mathbf{H} \hat{\mathbf{P}}_t \mathbf{H}^{\mathrm{T}} \tag{1.28}$$

1.4.3 Interacting Multiple Model Filter

The interacting multiple model filter (IMMF) takes the MMKF approach to adaptation. Its basic algorithm is presented in this section. The performance of the IMMF is compared against the method newly developed in this work in the results. The IMMF runs a bank of filters in parallel, each of which uses its own model, i.e. state transition and measurement equations. Its operation consists of three major stages, called interaction, filtering, and combination, in each iteration as shown in Algorithm 1. They are briefly explained in the following.

The interaction or mixing stage of the IMMF reinitializes initial conditions of each model filter, $\mathbf{X}_{t-1}^{0}$ and $\mathbf{P}_{t-1}^{0}$, by mixing state vector estimates from all model filters at a previous iteration based on mixing probabilities $\mu_{t-1}^{i|j}$. These are computed using Equation 2.7. Note that Equation 2.7 can be interpreted in the context of the Bayesian theorem where the mixing probability is a posterior,

Algorithm 1 IMMF algorithm

Interaction for model j

(a) Compute a mixing probability.

$$\mu_{t-1}^{i|j} = \frac{1}{c_j} p_{ij} \mu_{t-1}^{i} \tag{1.29}$$

where, p_{ij} is a model transition probability from model i to model j, μ_{t-1}^{i} is a probability of model i being correct at time $t-1$, and c_j is a normalization factor.

(b) Compute a mixed initial state $\mathbf{X}_{t-1}^{0}$ and its covariance $\mathbf{P}_{t-1}^{0}$.

$$\begin{aligned} \mathbf{X}_{t-1}^{0} &= \sum_{i} \hat{\mathbf{X}}_{t-1}^{i} \mu_{t-1}^{i|j} \\ \mathbf{P}_{t-1}^{0} &= \sum_{i} \{\hat{\mathbf{P}}_{t-1}^{i} + [\hat{\mathbf{X}}_{t-1}^{i} - \mathbf{X}_{t-1}^{0}][\hat{\mathbf{X}}_{t-1}^{i} - \mathbf{X}_{t-1}^{0}]^{\mathrm{T}}\} \mu_{t-1}^{i|j} \end{aligned} \tag{1.30}$$

where, $\hat{\mathbf{X}}_{t-1}^{i}$ is a state estimate from model i at time $t-1$, and $\hat{\mathbf{P}}_{t-1}^{i}$ is its covariance.

Filtering for model j

(a) Compute a predicted state $\hat{\mathbf{X}}_{t}^{-}$ and its covariance $\hat{\mathbf{P}}_{t}^{-}$.

$$\begin{aligned} \hat{\mathbf{X}}_{t}^{-} &= \Phi_j \mathbf{X}_{t-1}^{0} \\ \hat{\mathbf{P}}_{t}^{-} &= \Phi_j \mathbf{P}_{t-1}^{0} \Phi_j^{\mathrm{T}} + \mathbf{Q}_j \end{aligned} \tag{1.31}$$

where, Φ_j is a state transition matrix of model j and $\mathbf{Q}_j$ is a dynamic noise covariance of model j.

(b) Obtain a measurement $\mathbf{z}_t$.

(c) Compute an updated state $\hat{\mathbf{X}}_{t}^{j}$ and its covariance $\hat{\mathbf{P}}_{t}^{j}$.

$$\begin{aligned} \mathbf{K}_t &= \hat{\mathbf{P}}_{t}^{-} \mathbf{H}_j^{\mathrm{T}} [\mathbf{H}_j \hat{\mathbf{P}}_{t}^{-} \mathbf{H}_j^{\mathrm{T}} + \mathbf{R}_j]^{-1} \\ \hat{\mathbf{X}}_{t}^{j} &= \hat{\mathbf{X}}_{t}^{-} + \mathbf{K}_t (\mathbf{z}_t - \mathbf{H}_j \hat{\mathbf{X}}_{t}^{-}) \\ \hat{\mathbf{P}}_{t}^{j} &= [\mathbf{I} - \mathbf{K}_t \mathbf{H}_j] \hat{\mathbf{P}}_{t}^{-} \end{aligned} \tag{1.32}$$

where, $\mathbf{H}_j$ is an observation matrix of model j and $\mathbf{R}_j$ is a measurement noise covariance of model j.

(d) Compute an innovation $\mathbf{i}_t$ and its covariance $\mathbf{C}_t$.

$$\begin{aligned} \mathbf{i}_t &= \mathbf{z}_t - \mathbf{H}_j \hat{\mathbf{X}}_{t}^{-} \\ \mathbf{C}_t &= \mathbf{H}_j \hat{\mathbf{P}}_{t}^{-} \mathbf{H}_j^{\mathrm{T}} + \mathbf{R}_j \end{aligned} \tag{1.33}$$

(e) Compute a model probability.

$$\mu_{t}^{j} = \frac{1}{c} \Lambda_t \sum_{i} p_{ij} \mu_{t-1}^{i} \tag{1.34}$$

where, Λ_t is a likelihood function, $p(\mathbf{i}_t | \mathcal{N}(\mathbf{0}, \mathbf{C}_t)$, and c is a normalizing factor.

Combination

(a) Compute an unified state estimate.

$$\hat{\mathbf{X}}_t = \sum_{j} \hat{\mathbf{X}}_{t}^{j} \mu_{t}^{j} \tag{1.35}$$

the model transition probability p_{ij} is a likelihood, and the model probability μ_{t-1}^{j} is a prior. It is also worth noting that if the transition probabilities between all pairs of model filters are zero, the IMMF algorithm is reduced to the AMM algorithm [48]. The complete details of the interaction stage can be found in the interacting part of Algorithm 1.

The filtering stage of the IMMF is almost identical to the normal Kalman filter except for the model probability computation. The model probability μ_{t}^{j} is computed using an innovation $\mathbf{i}_t$ as shown in Equation 2.12. It represents the probability of a model being correct at the current iteration. Note that the IMMF algorithm also utilizes innovation information in its operation, similar to the AKF algorithm. The filtering part of Algorithm 1 shows the detailed procedures of the filtering stage.

In the combination stage, the IMMF estimates a unified state vector by combining state vector estimates from all model filters using their model probabilities. The details are listed in the combination part of Algorithm 1.

1.5 Novelty

This work proposes a new class of problem in time-varying noise. Figure 1.14 illustrates an example. It is expected that the dynamic noise has one of two possible states, typical or impulse. The typical dynamic noise occurs frequently, while the impulse dynamic noise occurs infrequently but with a value one or more orders of magnitude larger than the typical distribution. This figure can be contrasted with the types of problems intended to be addressed by both the AKF and MMKF approaches (see Figure 1.13a and Figure 1.13b). Using either of those approaches on the type of problem illustrated in Figure 1.14 produces sub-optimal results. Neither approach responds quickly to a change in the noise. This causes problems both in quickly adapting to large trajectory changes in the system dynamics, and in quickly returning to baseline measurement-to-dynamic noise filtering to provide sufficient smoothing.

The challenges addressed in this work include developing a new model that describes a system having occasional impulses in dynamic noise; implementing the model in a Kalman filter framework; determining its potential for improving upon existing methods across the possible ranges of measurement, typical, and impulse dynamic noises; demonstrating its performance on the practical problems of tracking human motion using UWB sensing and power state estimation; and applying

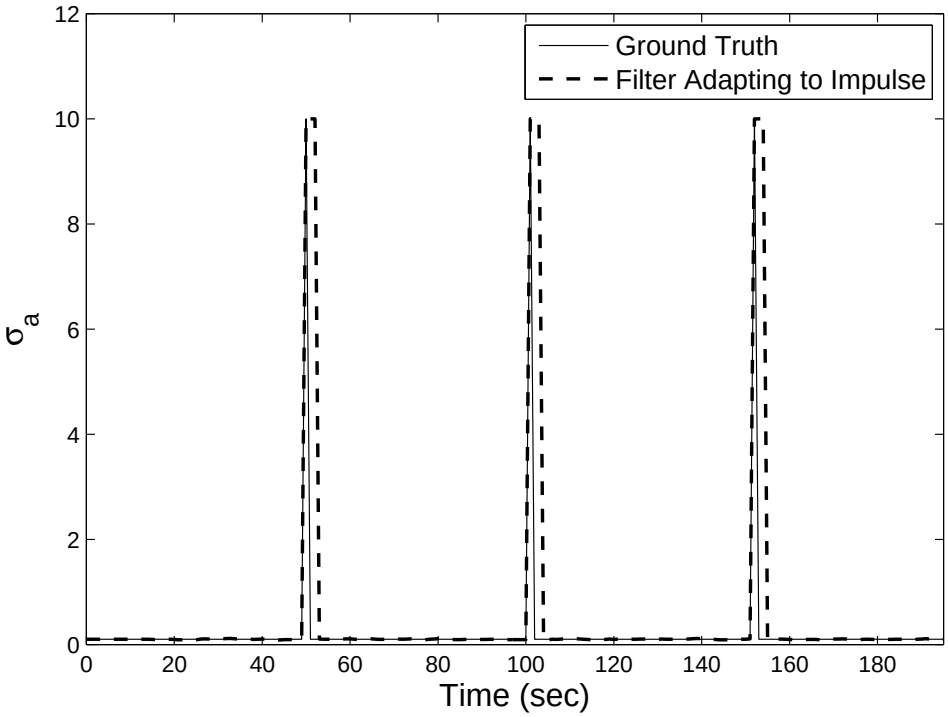

Figure 1.14: The proposed filter is intended to adapt to occasional impulses in dynamic noise.

the same idea to measurement noise to handle outlier measurements in a UWB position tracking.

Chapter 2

Impulse Model for Dynamic Noise

This chapter first presents an analysis of a publicly available data set of humans being tracked while moving in an indoor space. This is done to motivate the development of a new filter model of human motion. Finally, an algorithm for implementing this model in an MMKF framework is detailed.

2.1 Investigation of 2D Human Motion

Human motion can be studied in many ways, such as tracking hand motions during task completion, or facial feature tracking during communication, or full-body skeletal tracking of articulated joints during activities. The multiple model filtering approach has been applied in many such domains [43, 48], and is a popular technique to synthesize, classify, and track human motion [55, 64]. This work is motivated by the desire to track simple 2D human motion, such as location within a building as would be indicated by a map. To the author's knowledge no experimental assessment of the profile of this sort of human motion has been reported. Therefore, this section analyzes a publicly available dataset to determine its motion characteristics, in particular its acceleration profile.

Acceleration $\bar{a}$ is defined as the rate of a change in velocity $\Delta\mathbf{v}$ over a period of measurement time Δt as shown in Equation 2.1. The SI unit of acceleration is m/s^2. By definition, acceleration depends on the time interval over which it is measured. It is important to have a common measurement time interval when comparing accelerations of different objects. Instantaneous acceleration can be defined using Equation 2.2, but in practice it is impossible to measure because the measurement

Segment	Time (sec)	Speed (m/s)	Acceleration (m/s^2)
0 - 10 m	1.85	5.41	2.92
10 - 20 m	1.02	9.80	4.30
20 - 30 m	0.91	10.99	1.30
30 - 40 m	0.87	11.49	0.50
40 - 50 m	0.85	11.76	0.31
50 - 60 m	0.82	12.20	0.51
60 - 70 m	0.82	12.20	0.0
70 - 80 m	0.82	12.20	0.0
80 - 90 m	0.83	12.05	-0.18
90 - 100 m	0.90	11.11	-1.04

Table 2.1: Usain Bolt 100m speed data in 2008 Beijing Olympics

must take place over an interval of time. Alternatively, the average acceleration also can be defined over measured distances instead of time intervals. For example, human sprint races are sometimes analyzed this way, as shown in Table 2.1 [14].

$$\bar{a} = \frac{\Delta \mathbf{v}}{\Delta t} \tag{2.1}$$

$$\mathbf{a} = \lim_{\Delta t \to 0} \frac{\Delta \mathbf{v}}{\Delta t} \tag{2.2}$$

Accelerometers have been used to analyze and classify human motion [6, 12, 47], but these works studied motion more complex than simple 2D position. This section analyzes human motion videos from the CAVIAR project [24], which contain a variety of indoor human activities including people walking alone, meeting with others, and simulated fighting. The videos were analyzed to determine the acceleration profiles of human motion in 2D. Some example human activities of the dataset are shown in Figure 2.1. The videos were captured at 25 FPS and the resolution of each video is 384 x 288.

The ground truth image coordinates of each person in a video are available as an XML format in the dataset. For the acceleration analysis, the image coordinates of each person were projected onto the pre-surveyed two dimensional real world coordinate using the provided homography matrix. Figure 2.2 shows two different walking patterns in 2D world coordinates after the projections. Acceleration measurements were computed using these position data.

The accelerations of 29 people were measured at every 200 ms during 377 seconds (13

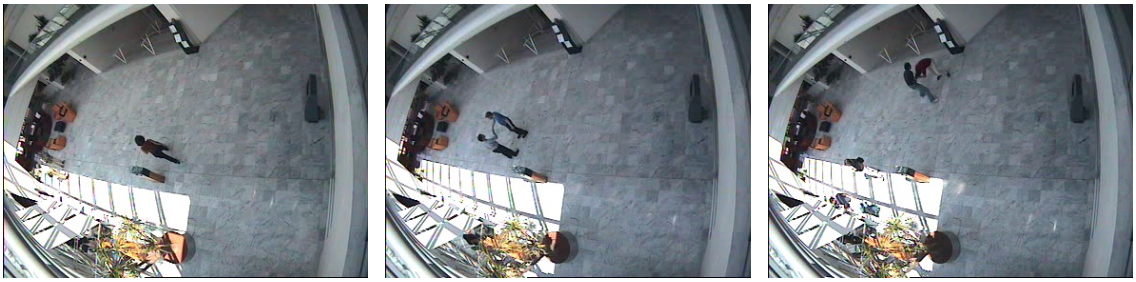

(a) Walking (b) Meeting (c) Fighting

Figure 2.1: CAVIAR dataset

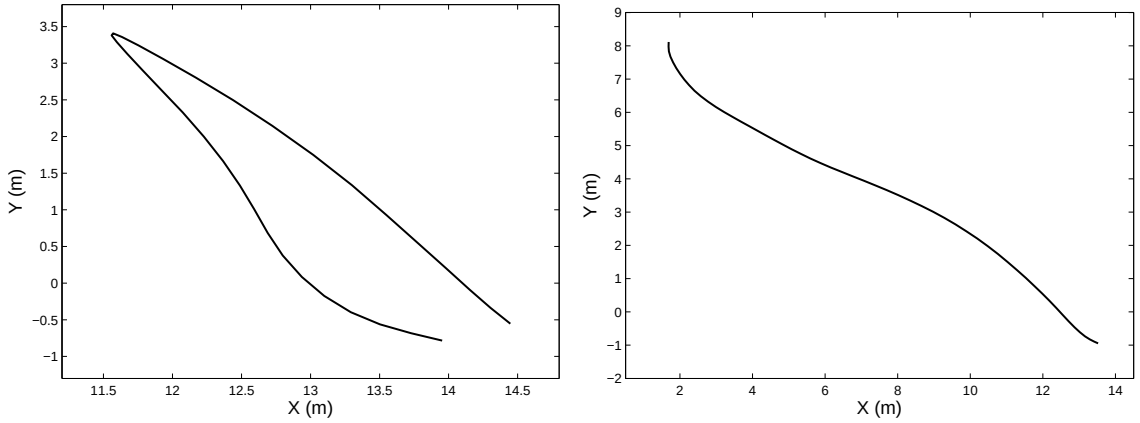

(a) Walking pattern one (b) Walking pattern two

Figure 2.2: Two different walking patterns

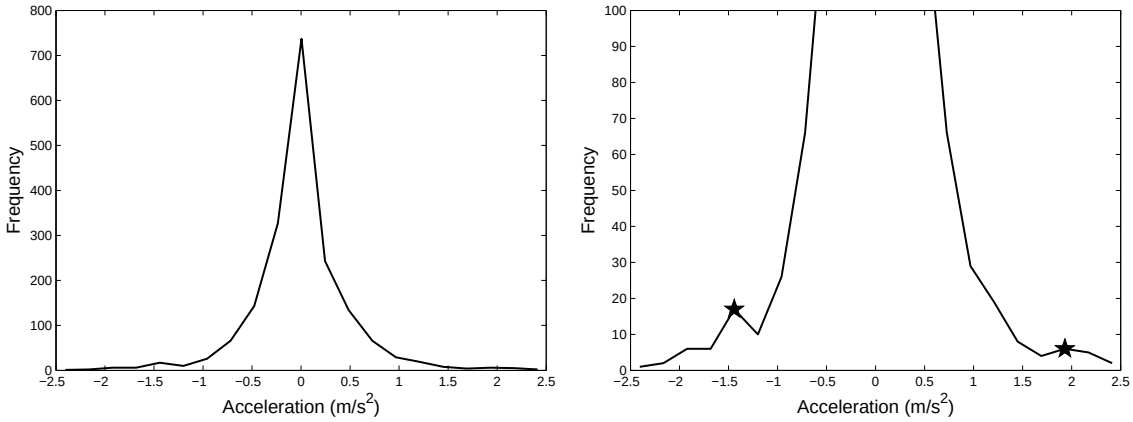

(a) Histogram (b) Histogram with zoom-in

Figure 2.3: Measured acceleration histogram

seconds for each person on average). Figure 2.3 shows the resulting histogram of the acceleration measurements. A zoomed-in version is shown in Figure 2.3b. From the figures, it can be observed that the acceleration profile resembles a Gaussian but has noticeable spikes out in the tails, marked as the filled stars. These spikes represent occasional large accelerations or decelerations. Figure 2.4 shows an illustration of this type of distribution. This work is motivated to develop a filter model that follows this distribution to improve the accuracy in tracking of 2D human motion.

2.2 Proposed Human Motion Model

Equation 2.3 is proposed as a model for 1D human motion. It can be applied to two dimensions by duplication, once for each coordinate. It describes how the dynamics of human motion evolves over time where s represents a dynamic motion state, x represents a 1D position, and $\dot{x}$ represents a 1D velocity. It is assumed that the dynamics of human motion follows the constant velocity model and alternates between a typical dynamic noise state ($s = 0$) and an impulse dynamic noise state ($s = 1$). Equation 2.4 describes the measurement process, where z is a 1D position measurement.

There are four parameters $(p_n, \sigma_a, \sigma_i, \sigma_m)$ in the equations. The parameter p_n is a probability of remaining in a typical dynamic noise state given that a previous state is also a typical dynamic noise state. The parameters σ_a, σ_i, and σ_m represent standard deviations of typical dynamic noise,

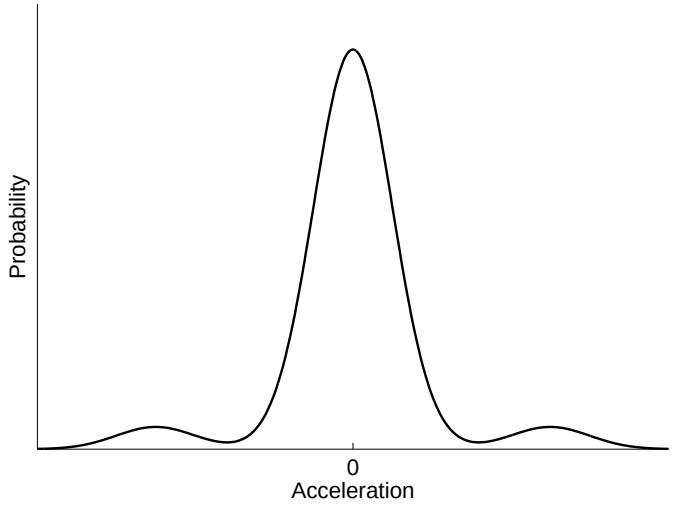

Figure 2.4: Multimodal acceleration

impulse dynamic noise, and measurement noise, respectively.

$$
\begin{aligned}
s_t &= \begin{cases} 0 & \text{if } s_{t-1} = 1 \text{ or } \mathrm{U}[0,1] \leq p_n \\ 1 & \text{otherwise} \end{cases} \\
x_t &= x_{t-1} + \dot{x}_{t-1} T \\
\dot{x}_t &= \begin{cases} \dot{x}_{t-1} + N(0, \sigma_a^2) & \text{if } s_t = 0 \\ \dot{x}_{t-1} + N(0, \sigma_i^2) & \text{if } s_t = 1 \end{cases}
\end{aligned}
\tag{2.3}
$$

$$
z_t = x_t + N(0, \sigma_m^2) \tag{2.4}
$$

2.3 Multiple-Model Kalman Filter with Impulse Response

In this section an algorithm is described that implements the proposed motion model in an MMKF framework. The new filter is called MMKF-IR (impulse response). The basic idea is that the filter executes a number of copies of Equation 2.3 where each copy takes turns transitioning into the impulse state ($s = 1$). In effect, the set of models is taking turns "guessing" that an impulse has just occurred. The MMKF framework calculates its output as a weighted sum of the set of model

outputs. It is assumed that those models undertaking the transition to an impulse state when no impulse has occurred will provide less weight to the output on average. It is also assumed that the single model that correctly "guesses" at the time when an impulse does actually happen will provide more weight to the output on average.

Algorithm 2 shows how the concept of the MMKF-IR can be implemented in the IMMF framework. The MMKF-IR algorithm uses a predefined matrix of state transitions to indicate when each model copy transitions to the impulse state. Let C represent the number of copies of the model, and let S represent the length of the pre-defined state transition sequences. The following matrix is used by the filter:

$$\mathbf{M}_{(\mathrm{C}+1)\times\mathrm{S}} = \begin{bmatrix} \mathbf{0}_{1\times\mathrm{S}} \\ \mathbf{I}_{\mathrm{C}\times\mathrm{S}} \end{bmatrix} \tag{2.5}$$

where the vector $\mathbf{0}_{1\times\mathrm{S}}$ indicates a copy of the model that never transitions to the impulse state, and the matrix $\mathbf{I}_{\mathrm{C}\times\mathrm{S}}$ represents C copies of the model that each transitions to the impulse state once. The use of an identity matrix insures that no two copies of the model transition to the impulse state at the same time. The following equation shows an example for when C=3 and S=3:

$$\mathbf{M}_{4\times3} = \begin{bmatrix} 0 & 0 & 0 \\ 1 & 0 & 0 \\ 0 & 1 & 0 \\ 0 & 0 & 1 \end{bmatrix} \tag{2.6}$$

Even though S can be set to any number, it may be preferable to set that length according to the likelihood of transitioning to the impulse state as specified by p_n in the motion model. For example, if p_n is set to 99.7%, it can be assumed that the impulse dynamic noise state occurs on average 1 out of 333 samples according to its model probability (0.3%), and therefore S can be set

Algorithm 2 IMMF-IR algorithm

Interaction for model j (Identical to IMMF)

(a) Compute a mixing probability.

$$\mu_{t-1}^{i|j} = \frac{1}{c_j} p_{ij} \mu_{t-1}^{i} \tag{2.7}$$

where, p_{ij} is a model transition probability from model i to model j, μ_{t-1}^{i} is a probability of model i being correct at time $t-1$, and c_j is a normalization factor.

(b) Compute a mixed initial state $\mathbf{X}_{t-1}^{0}$ and its covariance $\mathbf{P}_{t-1}^{0}$.

$$\begin{aligned} \mathbf{X}_{t-1}^{0} &= \sum_{i} \hat{\mathbf{X}}_{t-1}^{i} \mu_{t-1}^{i|j} \\ \mathbf{P}_{t-1}^{0} &= \sum_{i} \{\hat{\mathbf{P}}_{t-1}^{i} + [\hat{\mathbf{X}}_{t-1}^{i} - \mathbf{X}_{t-1}^{0}][\hat{\mathbf{X}}_{t-1}^{i} - \mathbf{X}_{t-1}^{0}]^{\mathrm{T}}\} \mu_{t-1}^{i|j} \end{aligned} \tag{2.8}$$

where, $\hat{\mathbf{X}}_{t-1}^{i}$ is a state estimate from model i at time $t-1$, and $\hat{\mathbf{P}}_{t-1}^{i}$ is its covariance.

Filtering for model j

(a) Compute an index $k = \mathrm{mod}(t, \mathrm{S})$.

(b) Compute a predicted state $\hat{\mathbf{X}}_{t}^{-}$ and its covariance $\hat{\mathbf{P}}_{t}^{-}$.

$$\begin{aligned} \hat{\mathbf{X}}_{t}^{-} &= \Phi_j \mathbf{X}_{t-1}^{0} \\ \hat{\mathbf{P}}_{t}^{-} &= \Phi_j \mathbf{P}_{t-1}^{0} \Phi_j^{\mathrm{T}} + \mathbf{Q}_{\mathbf{M}(j,k)} \end{aligned} \tag{2.9}$$

where, Φ_j is a state transition matrix of model j, and $\mathbf{Q}_{\mathbf{M}(j,k)}$ is a dynamic noise covariance of dynamic noise state $\mathbf{M}(j,k)$.

(c) Obtain a measurement $\mathbf{z}_t$.

(d) Compute an updated state $\hat{\mathbf{X}}_{t}^{j}$ and its covariance $\hat{\mathbf{P}}_{t}^{j}$.

$$\begin{aligned} \mathbf{K}_t &= \hat{\mathbf{P}}_{t}^{-} \mathbf{H}_j^{\mathrm{T}} [\mathbf{H}_j \hat{\mathbf{P}}_{t}^{-} \mathbf{H}_j^{\mathrm{T}} + \mathbf{R}_j]^{-1} \\ \hat{\mathbf{X}}_{t}^{j} &= \hat{\mathbf{X}}_{t}^{-} + \mathbf{K}_t (\mathbf{z}_t - \mathbf{H}_j \hat{\mathbf{X}}_{t}^{-}) \\ \hat{\mathbf{P}}_{t}^{j} &= [\mathbf{I} - \mathbf{K}_t \mathbf{H}_j] \hat{\mathbf{P}}_{t}^{-} \end{aligned} \tag{2.10}$$

where, $\mathbf{H}_j$ is an observation matrix of model j and $\mathbf{R}_j$ is a measurement noise covariance of model j.

(e) Compute an innovation $\mathbf{i}_t$ and its covariance $\mathbf{C}_t$.

$$\begin{aligned} \mathbf{i}_t &= \mathbf{z}_t - \mathbf{H}_j \hat{\mathbf{X}}_{t}^{-} \\ \mathbf{C}_t &= \mathbf{H}_j \hat{\mathbf{P}}_{t}^{-} \mathbf{H}_j^{\mathrm{T}} + \mathbf{R}_j \end{aligned} \tag{2.11}$$

(f) Compute a model probability.

$$\mu_{t}^{j} = \frac{1}{c} \Lambda_t \sum_{i} p_{ij} \mu_{t-1}^{i} \tag{2.12}$$

where, Λ_t is a likelihood function, $p(\mathbf{i}_t | \mathcal{N}(\mathbf{0}, \mathbf{C}_t)$, and c is a normalizing factor.

Combination (Identical to IMMF)

(a) Compute an unified state estimate.

$$\hat{\mathbf{X}}_t = \sum_{j} \hat{\mathbf{X}}_{t}^{j} \mu_{t}^{j} \tag{2.13}$$

to 333. In this case, the IMMF-IR can be built using the matrix specified in Equation 2.14.

$$\mathbf{M}_{334\times 333} = \begin{bmatrix} 0 & 0 & 0 & 0 & 0 & \cdots & 0 \\ 1 & 0 & 0 & 0 & 0 & \cdots & 0 \\ 0 & 1 & 0 & 0 & 0 & \cdots & 0 \\ \vdots & \vdots & \vdots & \vdots & \vdots & \ddots & 0 \\ 0 & 0 & 0 & 0 & 0 & \cdots & 1 \end{bmatrix} \tag{2.14}$$

Chapter 3

Simulation

This chapter uses simulations to explore the potential of the new filter for improving tracking performance. The simulations allow for the testing of performance across a range of values for measurement noise, typical dynamic noise, impulse dynamic noise, and impulse frequency. The first section examines these ranges relative to human and automobile motion, and to camera, GPS and UWB sensors, in order to provide context. The following section describes the data that was generated across these ranges. An evaluation metric is then defined. The configurations and initializations of all the filters are defined, and an upper bound on performance is established. The results of all the filters are then evaluated using this context.

3.1 Ranges of Analysis

The purpose of this section is to provide context for ranges of typical dynamic noise and impulse dynamic noise. The context is provided by enumerating ranges for each quantity with respect to human and automobile motion. This section also provides context for measurement noise by enumerating ranges for camera, GPS and UWB tracking systems. Finally these data are combined to enumerate ranges of measurement-to-dynamic noise ratios.

As stated in Chapter 2, the measurement of acceleration requires either a defined amount of time or distance. Both were used with different data sources to obtain reasonable ranges for human and automobile motion. Table 3.1 lists the results. The first ranges of human motion were obtained by analyzing Usain Bolt's 100m dash accelerations from Table 2.1. The impulse range

	Human				Automobile
	Usain Bolt [14]	CAVIAR [24]	Bayat [8]	Range	Bokare [11]
σ_a (m/s^2)	$0.1 \sim 0.18$	$0.1 \sim 0.2$	$0.1 \sim 1$	$\mathbf{0.1 \sim 1}$	$\mathbf{0.2 \sim 0.3}$
σ_i (m/s^2)	$2.92 \sim 4.3$	$1.5 \sim 2.5$	$9 \sim 12$	$\mathbf{1.5 \sim 12}$	$\mathbf{1.5 \sim 3}$

Table 3.1: Standard deviations for typical and impulse dynamic noise

	Camera [24]	GPS [52]	UWB [62]
σ_m (m)	0.04	$1 \sim 10$	$0.3 \sim 1$

Table 3.2: Standard deviations for measurement noise

was taken from the periods of time in which the sprinter achieved maximum acceleration, while the remaining periods of time were used to define a range of typical acceleration. The second estimates were obtained from the CAVIAR acceleration histogram in Figure 2.3. The impulse range was taken from the tails of the distribution while the rest of the range was used to define the range of typical acceleration. The third estimates were obtained from smart-phone acceleration data in Figure 2 of Bayat's work [8]. The impulse range was taken by including all the local acceleration extrema, and the rest of data were used to define the range of typical acceleration. The cumulative span of these three ranges is summarized in the "range" column of Table 3.1 and highlighted in bold. Finally, estimates of impulse and typical accelerations of automobiles were taken from the data in Figure 5 of Bokare's work [11], in which a number of different vehicle types were measured to determine acceleration profiles. The impulse range was obtained from the region of speed 0 - 5m/s, while the typical range was obtained from the region of speed more than 25m/s.

Table 3.2 shows the standard deviation values (σ_m) for measurement noise for three sensor types. The measurement noise (4 cm) of the camera system is computed from the CAVIAR video data by projecting one pixel difference to real world coordinates using the provided homography matrix. The measurement noise of the GPS ($1 \sim 10m$) is taken from a recent technical report analyzing its performance [52]. The measurement noise of a UWB position tracking system (30 - 100 cm) is taken from a recent survey of published results [62].

Using the previously determined ranges, the range of measurement-to-typical-dynamic noise for a camera system tracking human motion is estimated as:

$$\sigma_m^{\text{Camera}} / \sigma_a^{\text{Human}} = \frac{0.04\ m}{0.1 \sim 1\ m/s^2} \approx 0.04 \sim 0.4 \tag{3.1}$$

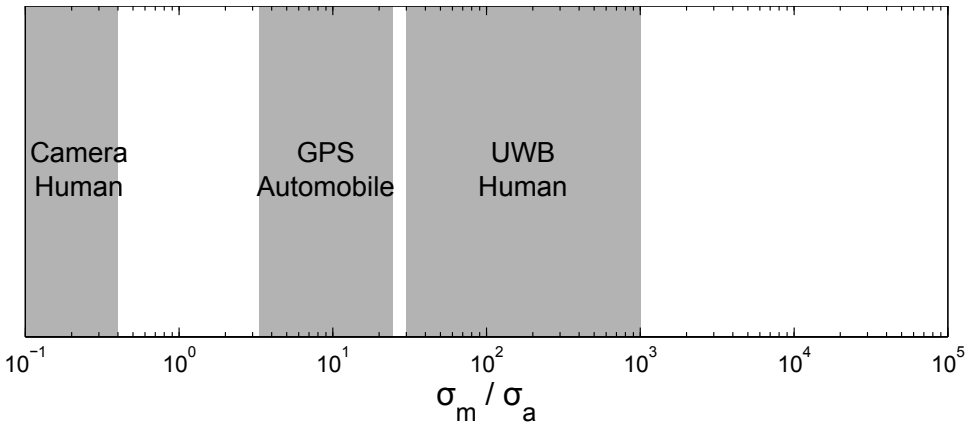

Figure 3.1: Measurement system σ_m/σ_a ratio ranges

	Camera	GPS	UWB
σ_m/σ_a	$0.04 \sim 0.4$	$3.33 \sim 50$	$30 \sim 1000$

Table 3.3: Measurement system σ_m/σ_a ratio ranges

The range of measurement-to-typical-dynamic noise for the GPS tracking automobile motion is estimated as:

$$\sigma_m^{\text{GPS}}/\sigma_a^{\text{Auto}} = \frac{1 \sim 10\ m}{0.2 \sim 0.3\ m/s^2} \approx 3.33 \sim 50 \tag{3.2}$$

The range of measurement-to-typical-dynamic noise for a UWB system tracking human motion is estimated using the following two equations:

$$\sigma_a^{\text{Human}} = 0.1 \sim 1\ m/s^2 \cdot \left(\frac{1\ s}{10\ sample}\right)^2 = 0.001 \sim 0.01\ m/sample^2 \tag{3.3}$$

$$\sigma_m^{\text{UWB}}/\sigma_a^{\text{Human}} = \frac{0.3 \sim 1\ m/sample}{0.001 \sim 0.01\ m/sample^2} \approx 30 \sim 1000 \tag{3.4}$$

These equations assume a UWB system operating at a rate of 10 Hz, similar to the equipment available for real data experiments described in the next chapter.

Table 3.3 summarizes these ranges, and Figure 3.1 illustrates them on a logarithmic scale. The placement of these systems on this scale helps provide context for the simulation results.

Another important ratio is impulse-to-typical dynamic noise. This describes the magnitude of an expected impulse relative to its usual distribution. The range for humans and automobiles

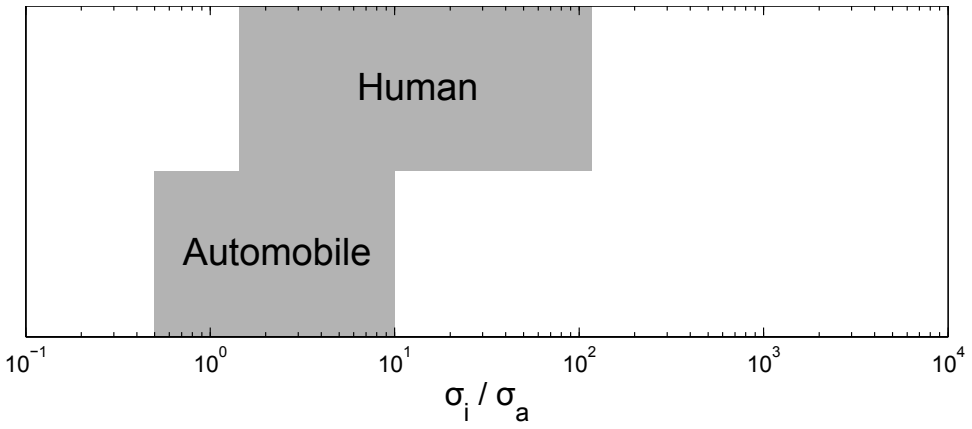

Figure 3.2: Context for σ_i/σ_a ratio ranges

were derived using the same data from above as follows:

$$\sigma_i^{\text{Human}}/\sigma_a^{\text{Human}} = \frac{1.5 \sim 12\ m/s^2}{0.1 \sim 1\ m/s^2} \approx 1.5 \sim 120 \tag{3.5}$$

$$\sigma_i^{\text{Auto}}/\sigma_a^{\text{Auto}} = \frac{1.5 \sim 3\ m/s^2}{0.2 \sim 0.3\ m/s^2} \approx 0.5 \sim 10 \tag{3.6}$$

Figure 3.2 illustrates these ranges on a logarithmic scale. It can be seen that they largely overlap, but that humans have a slightly higher range. However, note that these data are based upon defined periods of distance or time for estimating accelerations, and thus must be viewed accordingly.

The final important range is the percentage of impulse dynamic noise. For one estimate, the CAVIAR data set was again analyzed as illustrated in Figure 3.3. The percentage of data in the two tails (shaded areas) was found to be 2.8%.

3.2 Data Generation

Simulated motion data was generated using the human motion model proposed in Section 2.2. This data was used to compare the performance of newly proposed filter against existing techniques. For clarity, the equations for the human motion model are repeated in Equation 3.7 and Equation 3.8.

There are four variables of interest: measurement noise (σ_m), typical dynamic noise (σ_a),

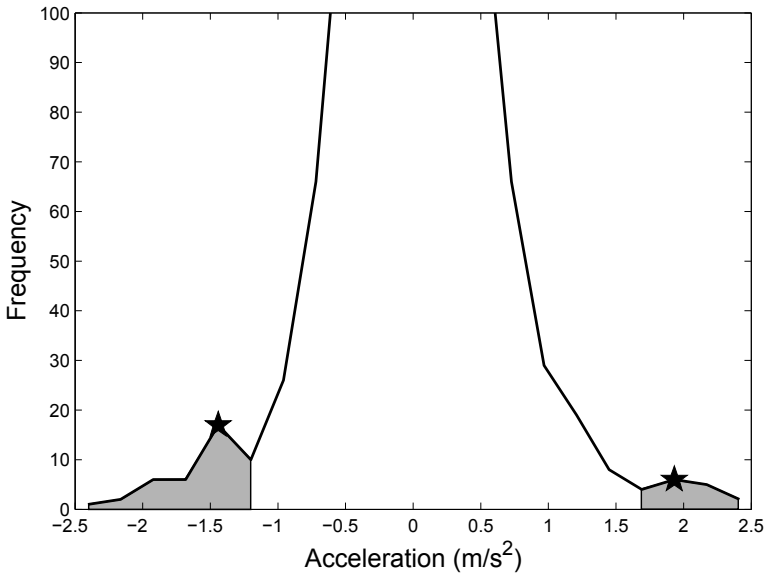

Figure 3.3: Typical and impulse dynamic noise areas. Non-grey region represents the typical dynamic noise area, while grey region represents the impulse dynamic noise area.

Scenario	p_n	σ_a	σ_i	σ_m	Range
σ_m/σ_a	0.997	0.1	10.0	varying	$0.1 \sim 10^5$
σ_i/σ_a	0.997	0.1	varying	30	$10 \sim 10^4$
$\sigma_i(\%)$	varying	0.1	10.0	30	$0.1 \sim 5$

Table 3.4: The three different scenarios

impulse dynamic noise (σ_i), and frequency of impulse occurrence (p_n). However, it is the ratio of measurement-to-dynamic noise that affects filter performance. Therefore, three ranges were evaluated in the simulations. First, the ratio of measurement-to-typical-dynamic noise was simulated by changing σ_m while fixing the other parameters. Second, σ_m was fixed to the value which generated the largest performance difference between the MMKF-IR filter compared to previous methods, then σ_i was varied across a range of impulse-to-typical dynamic noise. Finally, under the same value of σ_m, a range of the percentages of impulse dynamic noise was explored. Table 3.4 summaries how the three different ranges were simulated. The sampling rate $1/\Delta t$ was fixed to 1 sample/sec for all simulations.

Each value in each range was used to generate independent data sets 100 times, each of which was filtered. This was done to find average performance. For example, Table 3.5 shows a sample parameter set of human motion with a ratio of measurement-to-typical-dynamic noise equal

p_n	σ_a	σ_i	σ_m
0.997	0.1	10.0	30

Table 3.5: The sample parameter set of simulated human motion

to 300. This particular parameter set was used to generate 100 datasets to compute the average performances of all the filters. A dataset generated by the sample parameter set can be interpreted in such a way that the typical dynamic noise state ($s = 0$) dominates the ground truth positions (99.7%), while the impulse dynamic noise state ($s = 1$) rarely occurs (0.3%); σ_a and σ_i are set to 0.1 and 10, respectively and the ground truth position is corrupted by Gaussian noise with σ_m=20 to generate the measurements.

$$
\begin{aligned}
s_t &= \begin{cases} 0 & \text{if } s_{t-1} = 1 \text{ or } \mathrm{U}[0,1] \leq p_n \\ 1 & \text{otherwise} \end{cases} \\
x_t &= x_{t-1} + \dot{x}_{t-1} T \\
\dot{x}_t &= \begin{cases} \dot{x}_{t-1} + N(0, \sigma_a^2) & \text{if } s_t = 0 \\ \dot{x}_{t-1} + N(0, \sigma_i^2) & \text{if } s_t = 1 \end{cases}
\end{aligned}
\tag{3.7}
$$

$$
z_t = x_t + N(0, \sigma_m^2) \tag{3.8}
$$

3.3 Error Metric

The root means square error (RMSE) is calculated as the error metric. Its percentage improvement relative to the measurement RMSE is used to compare filter performances. The meaning of RMSE is the same as the standard deviation. It represents how spread out state vector estimates are from the ground truth. The RMSE equation is shown in Equation 3.9 where N is the number of measurements. The RMSE was computed 100 times on 100 different datasets of the same simulated

ratio to compute the average RMSE.

$$\mathrm{RMSE} = \sqrt{\frac{1}{\mathrm{N}}\sum_{i=1}^{\mathrm{N}}(\mathbf{X}_i - \hat{\mathbf{X}}_i)^{\mathrm{T}}(\mathbf{X}_i - \hat{\mathbf{X}}_i)} \tag{3.9}$$

3.4 Filters

The simulations compare four different types of filter: the Kalman filter, AKF, IMMF and IMMF-IR. Their initial setup information is given in this section. All the filter parameters are set according to the parameter set which generated a simulated human motion dataset. The initial states of filters are set using the first ground truth position x_1 as in Equation 3.10, and the initial state covariances of filters are set using σ_a as shown in Equation 3.11.

$$\mathbf{X}^0 = \begin{bmatrix} x_1 \\ 0 \end{bmatrix} \tag{3.10}$$

$$\mathbf{P}^0 = \begin{bmatrix} 0 & 0 \\ 0 & \sigma_a^2 \end{bmatrix} \tag{3.11}$$

Two Kalman filters, $\mathrm{KF_{low}}$ and $\mathrm{KF_{hi}}$, are implemented, differing according to the selection of dynamic noise. The $\mathrm{KF_{low}}$ filter was implemented using σ_a for its dynamic noise while $\mathrm{KF_{hi}}$ was implemented using σ_i for its dynamic noise. The $\mathrm{KF_{low}}$ filter provides optimal filtering during typical dynamic noise, while $\mathrm{KF_{hi}}$ provides optimal filtering during impulses.

The dynamic noise of the AKF was initially set to σ_a, and its window size (W) was set to 40. The value of 40 was empirically found to provide best results for the sampling rate and p_n.

Two IMMF filters, $\mathrm{IMMF_1}$ and $\mathrm{IMMF_2}$, were evaluated. Each of them consists of two model filters since there are two different dynamic motion models in the simulated human motion model. $\mathrm{IMMF_1}$ has the transition probability of Equation 3.12 which reflects the model transition probability of the dataset, while $\mathrm{IMMF_2}$ has the transition probability of Equation 3.13 which assumes independence between the model filters.

$$\mathbf{p}_{ij} = \begin{bmatrix} p_n & 1-p_n \\ 1 & 0 \end{bmatrix} \tag{3.12}$$

$$\mathbf{p}_{ij} = \begin{bmatrix} 1 & 0 \\ 0 & 1 \end{bmatrix} \tag{3.13}$$

Lastly, the model filters of IMMF-IR were evaluated using the matrix specified in Equation 3.14. The number of the pre-defined state transition sequence (S) was set to 333 since an impulse dynamic noise state occurs 1 out of 333 samples according to the model probability $1 - p_n$ (0.3%), and therefore the number of copies of model (C) is 333. However, note that a different set of model filters for IMMF-IR can be constructed regardless of the model probability. Equation 3.15 shows the model transition probability of the filter.

$$\mathbf{M}_{334\times333} = \begin{bmatrix} 0 & 0 & 0 & 0 & 0 & \cdots & 0 \\ 1 & 0 & 0 & 0 & 0 & \cdots & 0 \\ 0 & 1 & 0 & 0 & 0 & \cdots & 0 \\ \vdots & \vdots & \vdots & \vdots & \vdots & \ddots & 0 \\ 0 & 0 & 0 & 0 & 0 & \cdots & 1 \end{bmatrix} \tag{3.14}$$

$$\mathbf{p}_{ij} = \mathbf{I}_{334\times334} \tag{3.15}$$

3.5 Performance Upper Bound

In order to establish an upper bound on the possible performance improvement that could be provided by a multiple model filter, a version of a KF was implemented that switched between σ_a and σ_i at perfect times. This was done by coding the filter to follow the same set of impulse times calculated during generation of the simulated data sets. Figure 3.4 shows an example, where the filter can be seen to be behaving ideally. The dotted vertical line in the figure indicates the time when the impulse dynamic motion occurred.

Figure 3.5 shows the filter's performance on the simulated human motion datasets across ranges of measurement-to-typical-dynamic noise ratios and impulse-to-typical dynamic noise ratios. When the ratio of measurement-to-typical-dynamic noise is low, the filter offers little improvement over the raw measurements. In other words, there is really no need for any type of filter; because the measurement noise is so low, the raw measurements themselves can be used. This range is

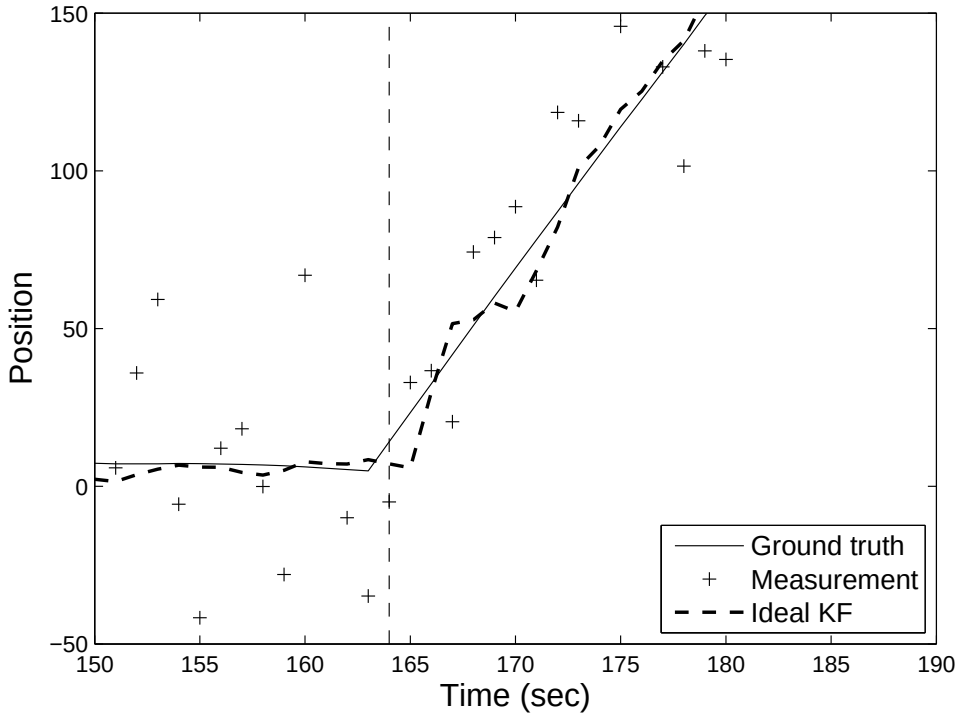

Figure 3.4: Ideal multiple model Kalman filter position estimate

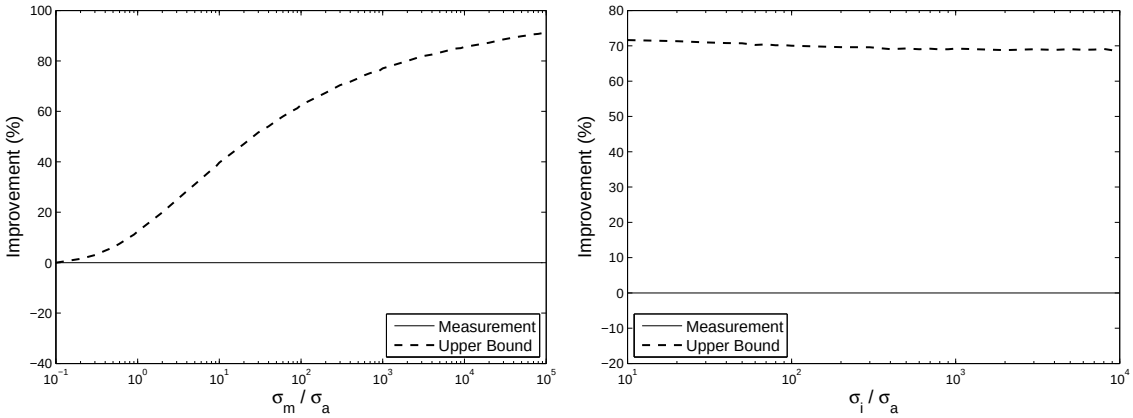

(a) Measurement-to-typical-dynamic ratio

(b) Impulse-to-typical dynamic ratio

Figure 3.5: Upper bound

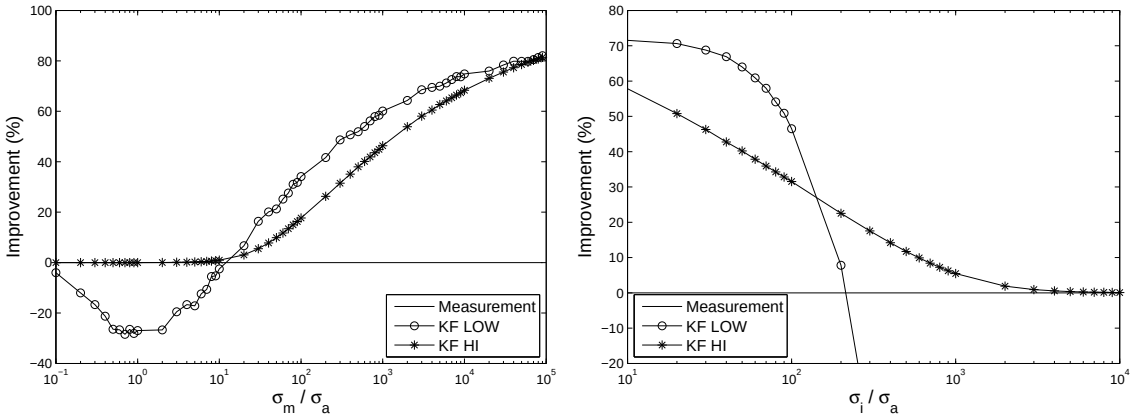

(a) Measurement-to-typical-dynamic ratio

(b) Impulse-to-typical dynamic ratio

Figure 3.6: Kalman filter performance

where camera-based tracking of human motion tends to reside. As the range increases past 10^0, a performance improvement begins to occur, eventually rising as high as 90%. With respect to the ratio of impulse-to-typical dynamic noise, a performance improvement of approximately 70% was found across the entire range. These curves establish an upper bound for the performance improvement that can be expected by this approach.

3.6 Performance Analysis

This section presents the performances of the filters on the simulated human motion data, and analyzes the reasons why one filter outperforms the other filters using examples.

3.6.1 Kalman Filter

Figure 3.6a shows the RMSE percentage improvement of the two Kalman filters relative to the measurement RMSE across a range of measurement-to-typical-dynamic noise. As can seen in the figure, $\mathrm{KF}_{\mathrm{low}}$ performs worse than the raw measurements and $\mathrm{KF}_{\mathrm{hi}}$ at low σ_m/σ_a ratios since it tries to balance between a predicted state vector estimate and measurement instead of relying on almost noise-free measurements. However, its performance exceeds $\mathrm{KF}_{\mathrm{hi}}$ at high σ_m/σ_a ratios because of large measurement noise. In opposite to $\mathrm{KF}_{\mathrm{low}}$, the performance of $\mathrm{KF}_{\mathrm{hi}}$ is compatible with raw measurements at low σ_m/σ_a ratios due to its high weighting of measurements that are corrupted by low levels of noise, but its performance becomes worse than $\mathrm{KF}_{\mathrm{low}}$ as the σ_m/σ_a ratio

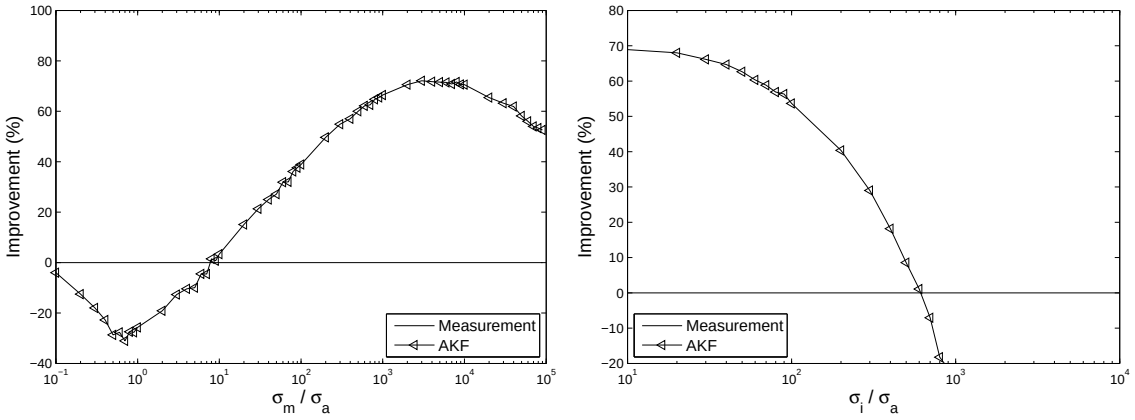

(a) Measurement-to-typical-dynamic ratio

(b) Impulse-to-typical dynamic ratio

Figure 3.7: Adaptive Kalman filter performance

increases. Finally, the performances of the two KF filters are similar to each other at extremely large measurement noises since the values of dynamic noise used by the filters do not make much difference in this situation.

The results across a range of impulse-to-typical dynamic ratios are shown in Figure 3.6b. The performance of $\mathrm{KF}_{\mathrm{low}}$ rapidly degenerates as the σ_i/σ_a ratio increases because its response time to the impulse dynamic motion gets longer and longer. Conversely, the rate of performance degeneracy of $\mathrm{KF}_{\mathrm{hi}}$ is relatively slow compared to $\mathrm{KF}_{\mathrm{low}}$, and its performance converges to the raw measurements.

In the later summary, only $\mathrm{KF}_{\mathrm{low}}$ will be compared against the other types of filters as the representative of the Kalman filter since its performance is better at high σ_m/σ_a ratios.

3.6.2 Adaptive Kalman Filter

The AKF exhibits a similar performance pattern as $\mathrm{KF}_{\mathrm{low}}$ across the range of σ_m/σ_a ratios as shown in Figure 3.7a. Unlike $\mathrm{KF}_{\mathrm{low}}$, however, its performance starts degenerating again after σ_m/σ_a reaches 4000 because its window size is not large enough to correctly estimate a dynamic noise covariance in a large measurement noise condition. Its performance degeneracy is also similar to $\mathrm{KF}_{\mathrm{low}}$ as σ_i/σ_a increases as shown in Figure 3.7b. This is because a big difference between σ_a and σ_i makes a correction statistics estimation more difficult and thus causes a large lag in the filter response.

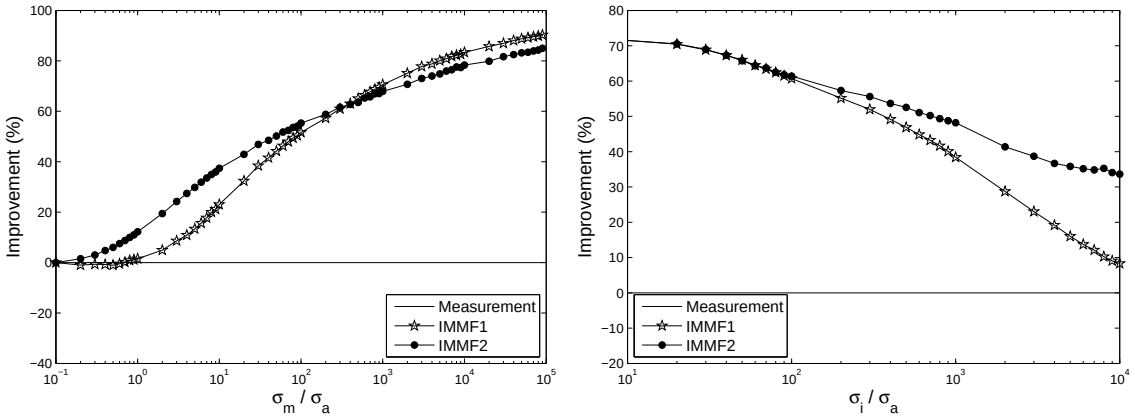

(a) Measurement-to-typical-dynamic ratio

(b) Impulse-to-typical dynamic ratio

Figure 3.8: Interacting multiple model filter performance

3.6.3 IMMF

The performance results of the two IMMFs are shown in Figure 3.8. It can be observed in Figure 3.8a that IMMF_2 outperforms IMMF_1 at low σ_m/σ_a ratios due to the fact that IMMF_2 with the transition probability set by Equation 3.13 is more sensitive to impulse dynamic noise at low σ_m/σ_a ratios. However, this sensitivity makes its performance worse than IMMF_1 with the transition probability set by Equation 3.12 at high σ_m/σ_a ratios as shown in Figure 3.8a. Therefore, in the summary both IMMF_1 and IMMF_2 will be compared against the other types of filters.

3.6.4 IMMF-IR

Overall, the IMMF-IR displays a similar performance pattern as the two IMMFs across the range of σ_m/σ_a ratios as shown in Figure 3.9a. However, its rate of performance degeneracy is much faster than the two IMMFs when the σ_i/σ_a ratio increases which can be observed in Figure 3.9b. This is because the magnitude of impulse dynamic noise relative to measurement noise also becomes large at high σ_i/σ_a ratios. Its effect is similar to a relatively low measurement noise environment where measurements can provide reliable information on a dynamic change of motion, and therefore IMMF outperforms IMMF-IR at high σ_i/σ_a ratios.

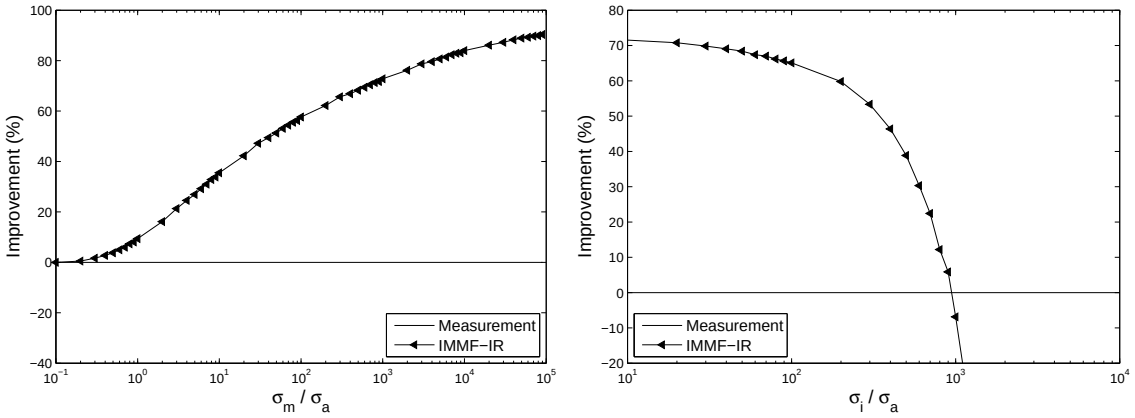

(a) Measurement-to-typical-dynamic ratio

(b) Impulse-to-typical dynamic ratio

Figure 3.9: Interacting multiple model filter with impulse response performance

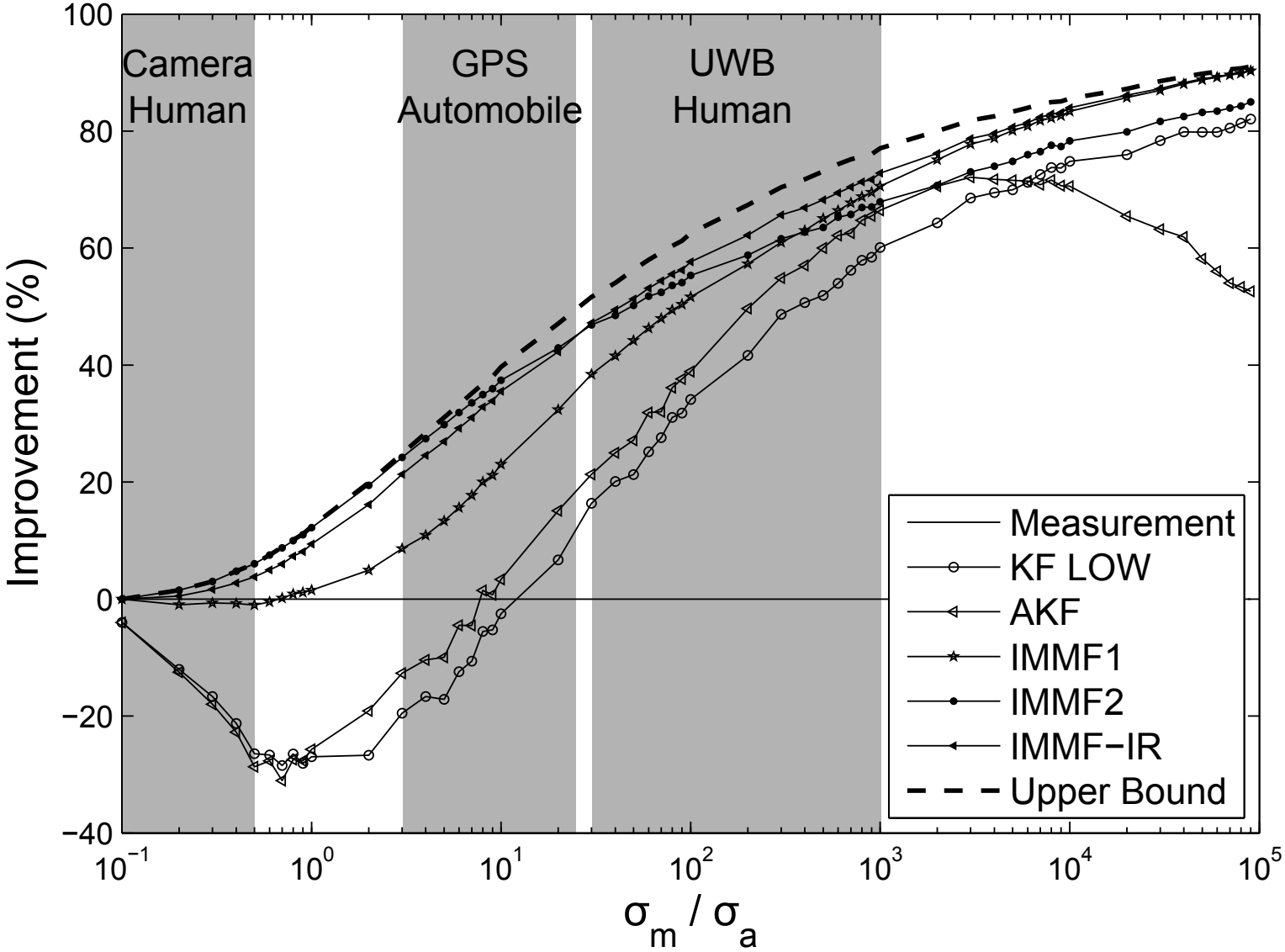

Figure 3.10: Summary of filter performances on various σ_m/σ_a ratios

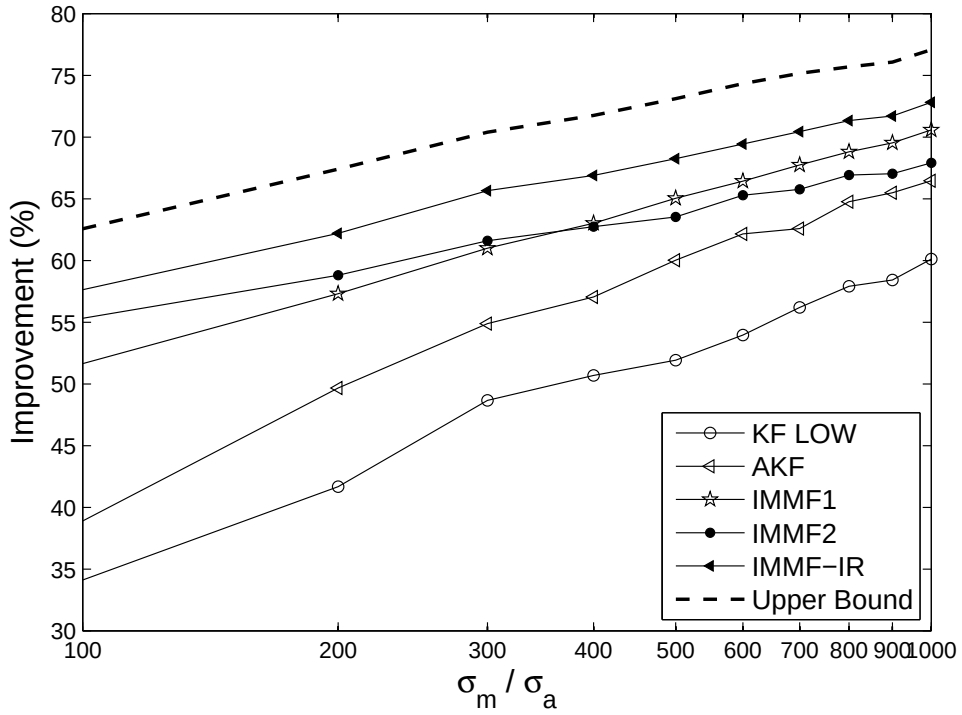

Figure 3.11: The best IMMF-IR performance relative to the other filters

3.6.5 Summary

Figure 3.10 summarizes the performances of the different types of filters. Generally, KF_{low} shows the worst performance among all the filters. The performance of the AKF is slightly better than KF_{low}. It can be seen from the figure that $IMMF_2$ and IMMF-IR collectively achieve the best performance across the whole test range. The IMMF-IR shows the best performance in the range characterized by human tracking using UWB sensing. Figure 3.11 shows a zoomed view of the area around which the IMMF-IR shows the best performance improvement relative to the other filters.

The performances of the filters across a range of impulse-to-typical dynamic noise ratios are summarized in Figure 3.12. It can be observed that KF_{low} and AKF rapidly drop as the σ_i/σ_a ratio increases. The performance of IMMF-IR is best until just past the range 10^2.

Figure 3.13 summarizes the filter performances across a range of percentages of occurrences of impulse. All the filters generally deteriorate as the percentage of impulse dynamic noise increases. In particular, the rates of performance decrease of the IMMFs are faster than the other filters except for KF_{low}, and they both start performing worse than AKF after the impulse dynamic noise

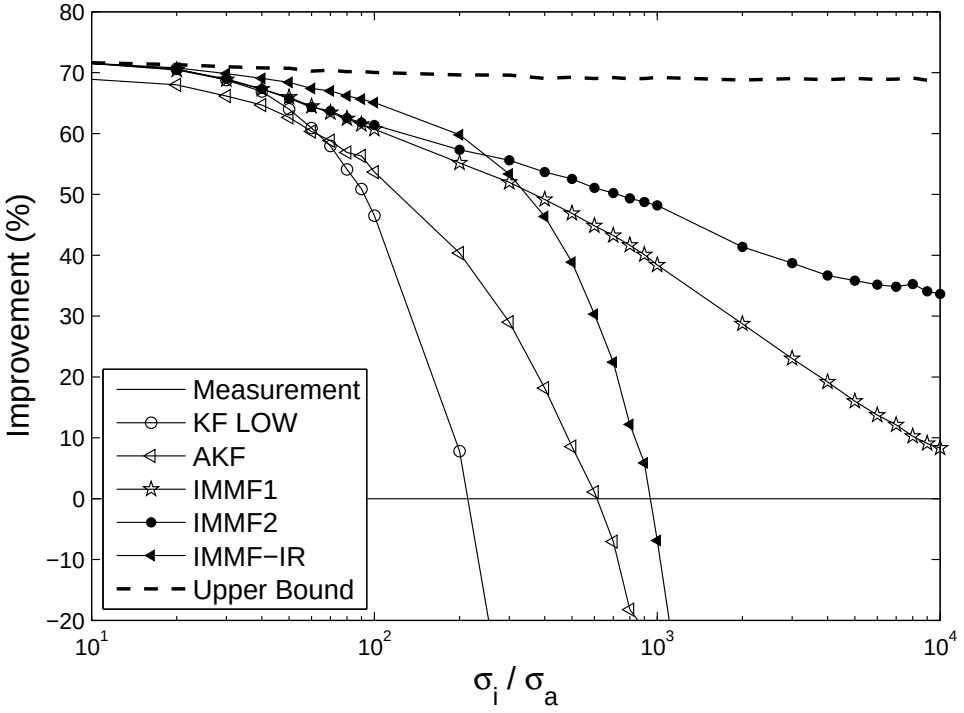

Figure 3.12: Summary of filter performances on various σ_i/σ_a ratios

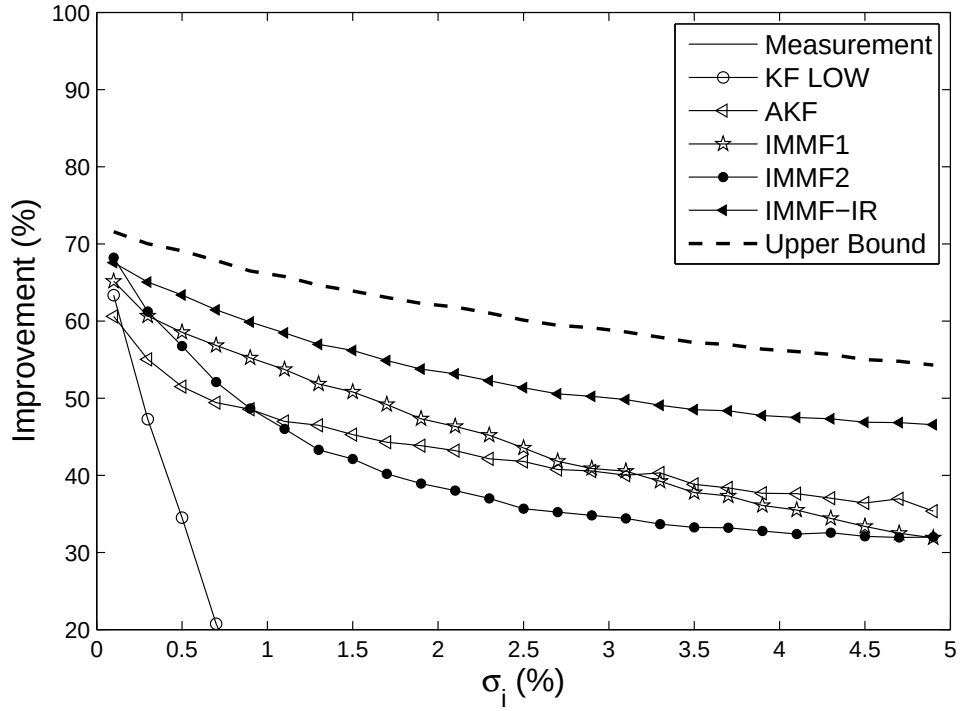

Figure 3.13: Summary of filter performances on various σ_i percentages

p_n	σ_a	σ_i	σ_m
0.997	0.1	10.0	30

Table 3.6: The sample parameter set of simulated human motion

percentage reaches 3.0%. Conversely, the rate of performance decrease of IMMF-IR is relatively slow as the impulse dynamic noise percentage increases compared with the other filters. IMMF-IR maintains the best performance over all the experimented p_n percentages. Note that the different set of model filters of IMMF-IR is constructed according to the impulse dynamic noise percentage in each experiment. For example, if the impulse dynamic noise percentage is set to 1%, the model filters of IMMF-IR are built using the matrix specified in Equation 3.16 where C = 100 and S = 100.

$$\mathbf{M}_{101\times100} = \begin{bmatrix} 0 & 0 & 0 & 0 & 0 & \cdots & 0 \\ 1 & 0 & 0 & 0 & 0 & \cdots & 0 \\ 0 & 1 & 0 & 0 & 0 & \cdots & 0 \\ \vdots & \vdots & \vdots & \vdots & \vdots & \ddots & 0 \\ 0 & 0 & 0 & 0 & 0 & 0 & 1 \end{bmatrix} \tag{3.16}$$

3.6.6 Examples

In this section, the filters are demonstrated on the dataset which is generated using the parameter set in Table 3.6. The position estimates of AKF and IMMF_2 are analyzed and compared against that of IMMF-IR to give an idea why IMMF-IR performs the best at high σ_m/σ_a ratios. All the filters are initialized according to the setup instructions in Section 3.2.

3.6.6.1 Adaptive Kalman Filter

The AKF was developed under the assumption that the statistics of a target system do not frequently change over time and remain stable for at least the previous W iterations. Thus, the correct estimation on an innovation covariance using innovation samples is feasible. Otherwise, the AKF fails to adapt correct statistics, and consequently fails to estimate a state vector of a target system. This assumption does not hold in the simulated human motion data since the impulse dynamic noise state instantly occurs. As shown in Figure 3.14b, the AKF starts to fail to adapt

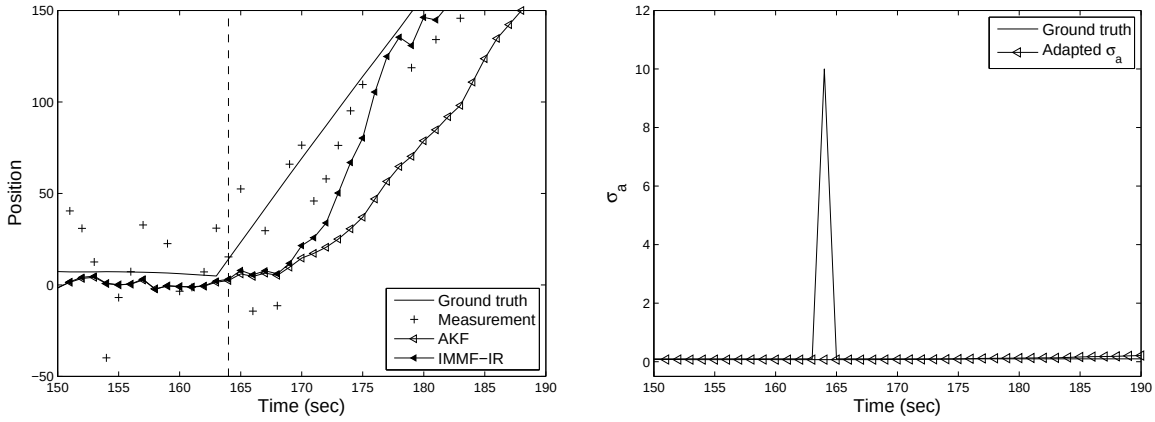

(a) AKF vs. IMMF-IR

(b) AKF σ_a estimate

Figure 3.14: AKF position estimate

a correct dynamic noise σ_a around the acceleration point. Figure 3.14a shows a lag in the AKF position estimate caused by the incorrect estimation of dynamic noise, which makes its performance worse than IMMF-IR.

3.6.6.2 Interacting Multiple Model Filter

The IMMF works well when the ratio of measurement noise to typical dynamic noise is small which means measurements can provide reliable information on a dynamic change of motion. But if the ratio is large, the IMMF easily gets confused whether a big jump in a position measurement is due to the measurement noise or a model change. Figure 3.15 shows such a situation where the IMMF with two models is applied on a dataset. As shown in Figure 3.15b, the filter with the typical dynamic model remains dominant for a while even after the acceleration point, and IMMF tries to catch up to the position difference by switching to the impulse dynamic model about 7 seconds after the acceleration point. This is why its response to impulse dynamic motion is slower than IMMF-IR as shown in Figure 3.15a. This also makes the overall performance worse than IMMF-IR.

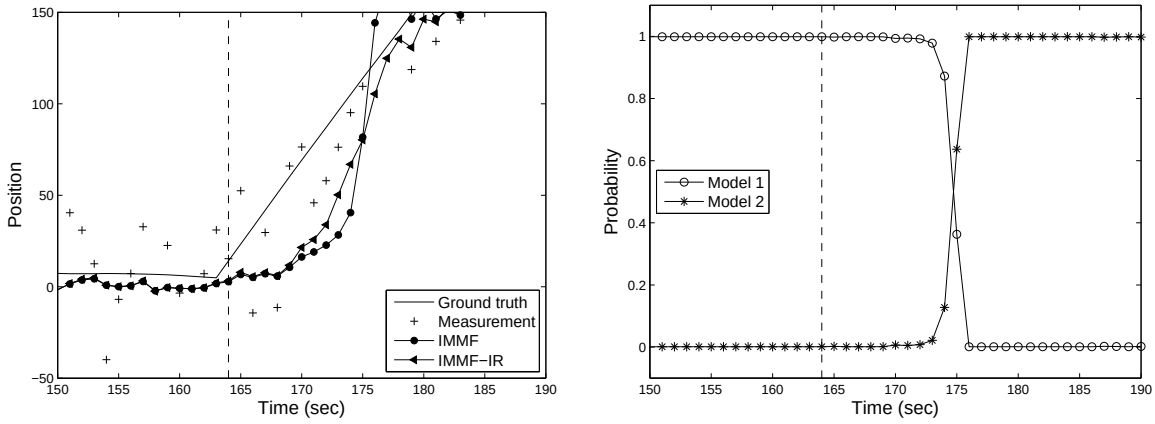

(a) IMMF vs. IMMF-IR

(b) IMMF model probabilities

Figure 3.15: IMMF position estimate. Model 1 represents a filter set with σ_a while model 2 represents a filter set with σ_i.

Chapter 4

UWB Position Tracking

This chapter describes experiments testing the new filter on real UWB measurements tracking 2D human motion. First, the test facility and the Ubisense tracking system are described. Then the estimation of ground truth motion and collection of tracking data are provided. Finally, the performance of the new filter is compared against existing methods.

4.1 Test Facility

The test facility is located in the basement of Riggs Hall at Clemson University. The floor plan of the test facility is given in Figure 4.1. As shown in the floor plan, the dimension of the test facility is approximately 8 m x 10 m. It includes part of a hallway and open lab space that are separated by a 20 cm thick concrete wall. The floor plan also depicts the metal and wooden cabinets, metal cupboards, and vending machine as parts of a normal indoor environment that possibly obstruct a UWB signal. The images in Figure 4.2 and Figure 4.3 show the test facility from the inside and outside of the lab space. As shown in the figures, the ceiling is covered by fiber tiles. The receivers for the tracking system are installed above this dropped ceiling, which together with the other obstacles make the system susceptible to NLOS and multipath errors.

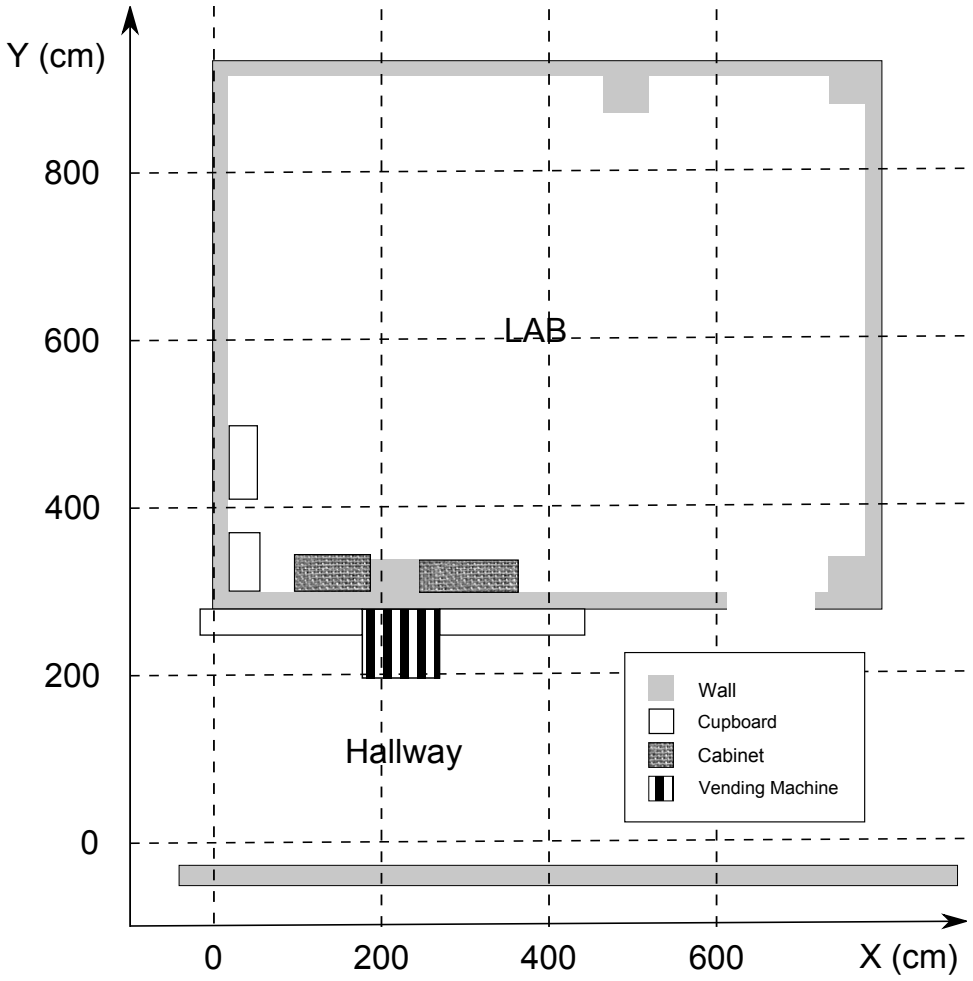

Figure 4.1: Test facility floor plan

Figure 4.2: Test facility: an open lab space

Figure 4.3: Test facility: a hallway

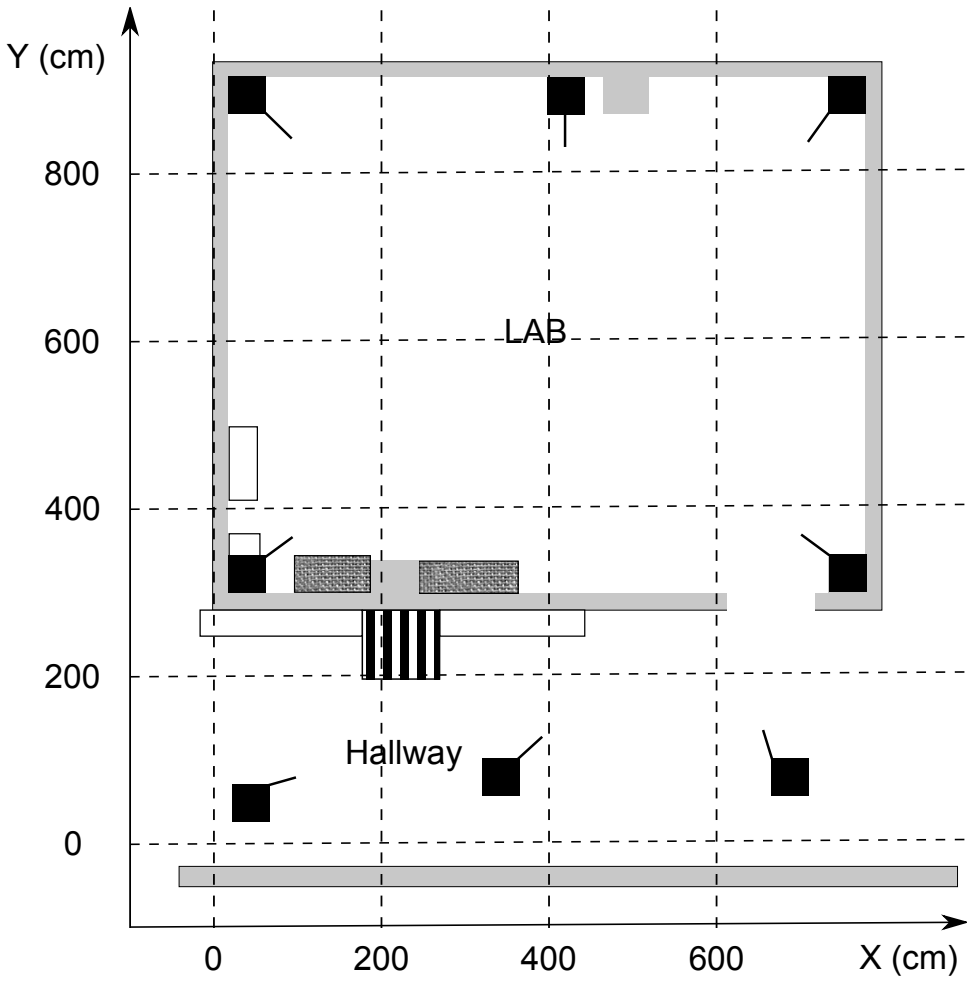

Figure 4.4: Test facility: eight receiver positions. The filled square represents a receiver, and the line coming from that filled square represents its orientation.

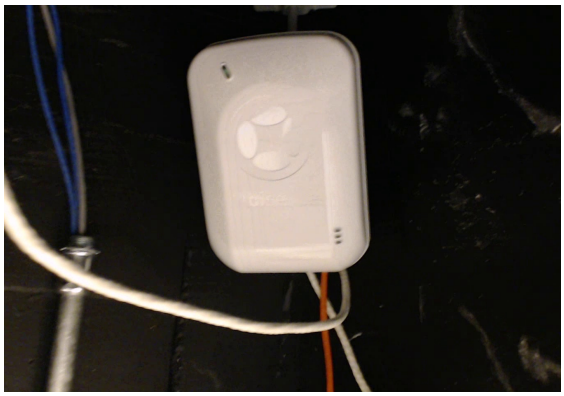

(a) Receiver (20cm x 14cm x 6.5cm)

(b) Transmitter (3.8cm x 3.9cm x 1.65cm)

Figure 4.5: Ubisense receiver and transmitter

4.2 Ubisense Tracking System

The tracking system is a real-time locating system developed by a U.K. based company, Ubisense Inc. It comprises multiple pieces, including transmitters, receivers, a timing distribution unit, and a network switch. Its typical installation layout can be found in the Ubisense system documentation [67]. The system computes range measurements to moving transmitters, which run on batteries, using angle of arrival (AOA) and time difference of arrival (TDOA) information collected from receivers that are powered by a network switch [66]. After the range measurement synchronization by the timing distribution unit, the system generates 3D position measurements through multilateration using range estimates from at least two receivers [66].

In this work, eight receivers of the Ubisense Series 7000 IP sensors are installed in the Riggs test facility as laid out in Figure 4.4. Their 3D positions were precisely surveyed using hand measurement tools based on the user-defined origin. Figure 4.5a shows an installation picture of one of the receivers inside of the dropped ceiling. The signal propagation delays between the receivers and timing distribution unit are calibrated for the range measurement synchronization using one of the Ubisense Series 7000 Compact tags (or transmitters) that is placed at a fixed known location. The pitches and yaws of the receivers are also calibrated in the same manner. Figure 4.5b shows a picture of the transmitter.

The installed receiver is capable of providing real-time position updates of transmitters [66]. However, in reality this capability is limited by the working frequencies of the transmitter, which is in the range of 0.00225 Hz - 33.75 Hz [65], and the number of the transmitters in use at the same

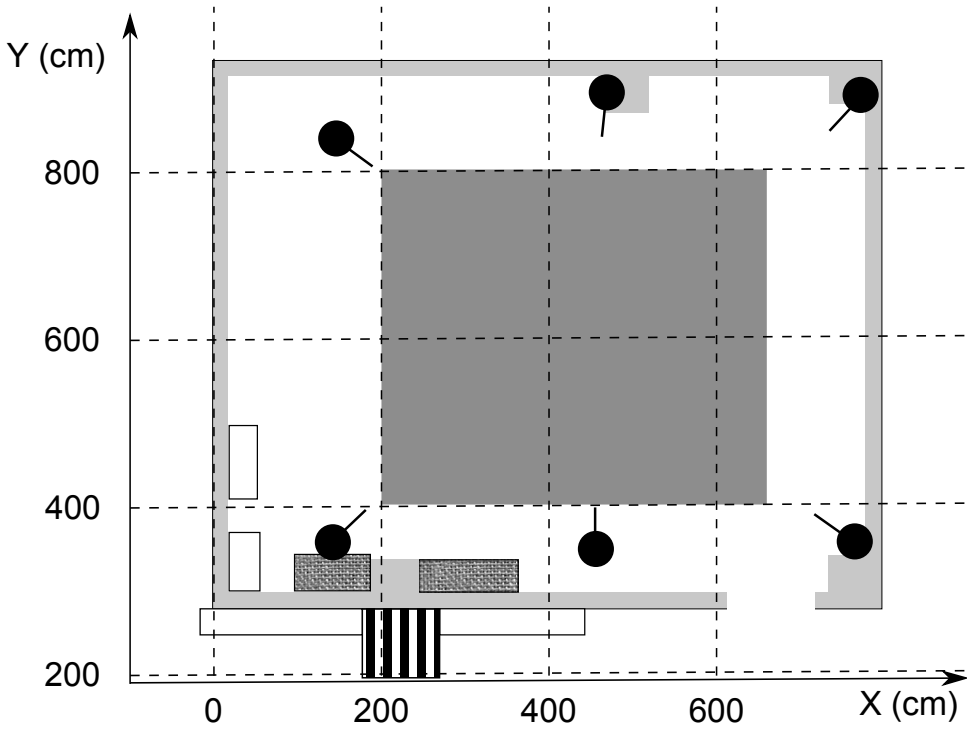

Figure 4.6: Camera network and its coverage area. Filled circles represent cameras, and the lines coming from filled circles represent their orientations. The big gray rectangle in the center represents the camera network coverage area.

time. Our experiments show that the Ubisense tracking system works approximately at 10 Hz when the number of the transmitters is 1 - 4, but this working frequency drops down to about 5 Hz when the number of transmitters is 5 - 8.

4.3 Ground Truth

A network of six cameras was used to calculate 2D ground truth positions for UWB tracking data. The camera network operates at 20Hz [5]. Figure 4.6 illustrates how the six cameras are installed and how much area the camera network covers in the lab space.

Specifically, an occupancy map (640 $\times$ 480) is created from the camera network through background subtraction and pixel-to-plane projection, and then a target object is detected and tracked in the occupancy map using a blob detection algorithm [30]. For example, the white target circle in Figure 4.7a is detected as the white blob on the right of the occupancy map in Figure 4.7b. Each pixel in the occupancy map indicates space in the lab floor, and its binary intensity represents

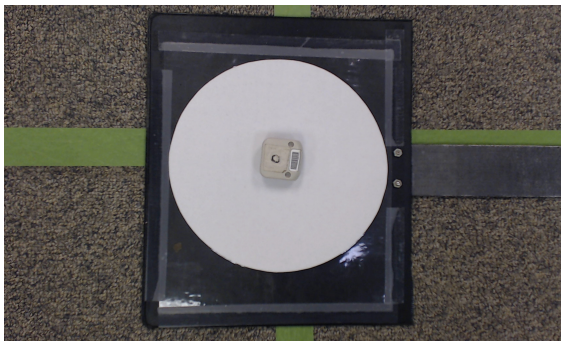

(a) White target circle with Ubisense tag

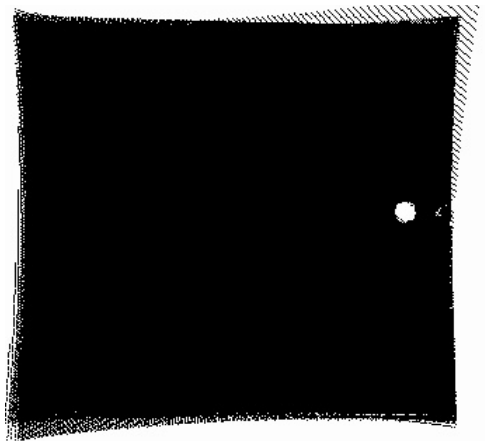

(b) Occupancy map. White represents occupied while black represents unoccupied.

Figure 4.7: Camera network target tracking

	Mean	Standard deviation
Error (X,Y)	(0.19cm, 0.17cm)	(0.47cm, 0.56cm)

Table 4.1: Camera network position error statistics

occupancy. In Figure 4.7a the Ubisense tag is placed in the center of the white target circle so that the center of a white blob in an occupancy map can be treated as an Ubisense tag location. Finally, pixel coordinates of the center of a blob are projected from the occupancy map to the Ubisense tracking system coordinate to provide the 2D ground truth positions for UWB tracking data.

The accuracy of the camera network was evaluated at 12 different locations as shown in Figure 4.8. In the figure, a mean position ($\times$) from the camera network is displayed together with its ground truth position ($+$) and UWB measurements ($\cdot$). Each mean position of the camera network is calculated using 500 camera network position measurements. The position error statistics of the camera network are summarized in Table 4.1, and overall they show better than 1 cm accuracy.

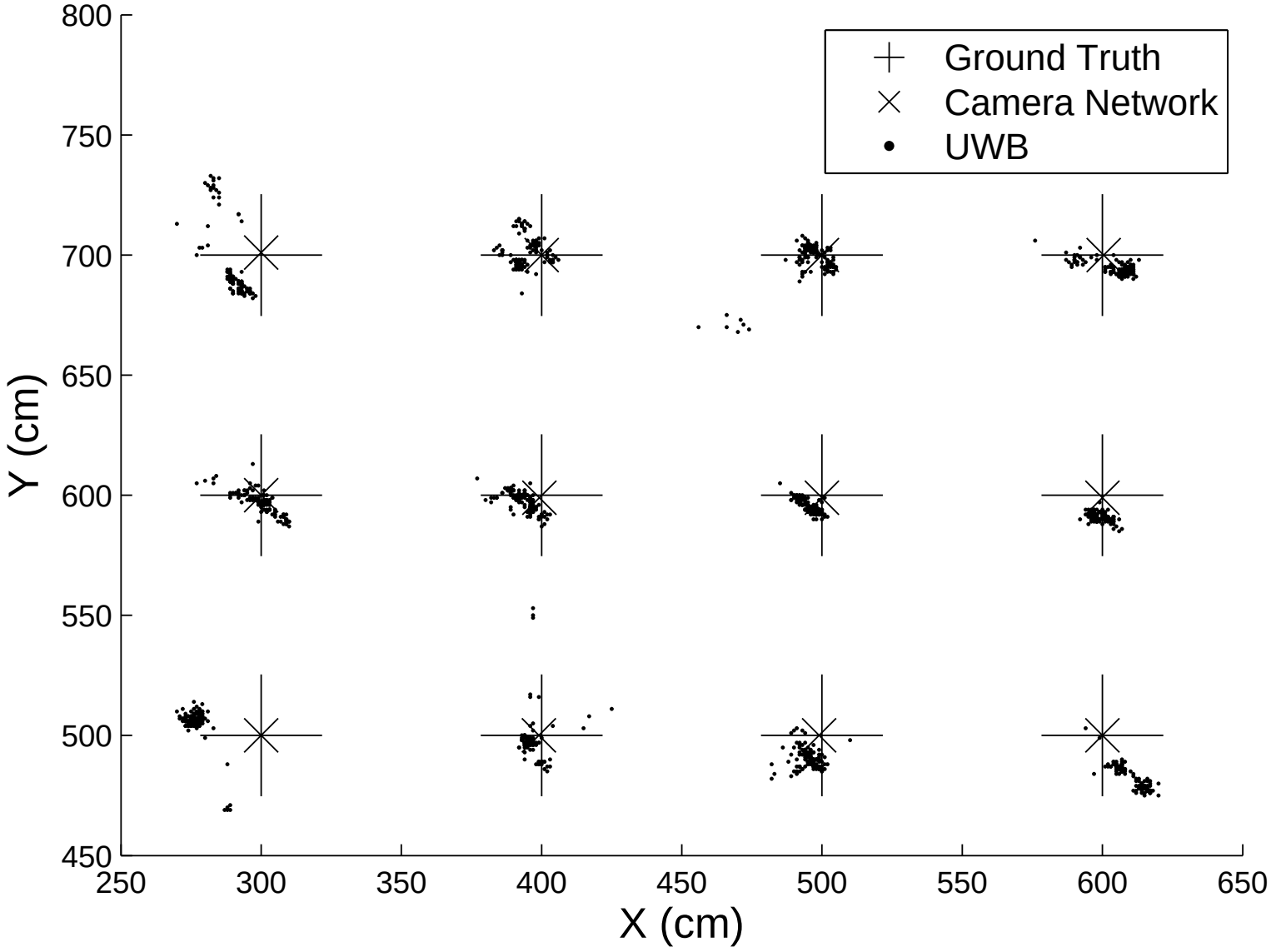

Figure 4.8: Camera network accuracy

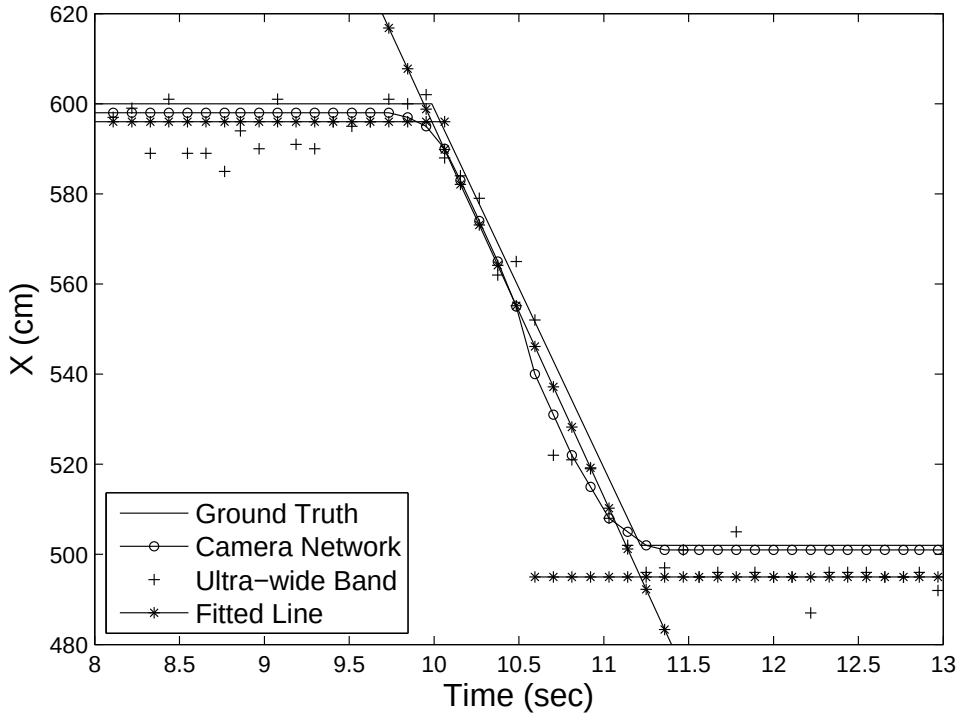

Figure 4.9: Camera network synchronization with Ubisense tracking system.

The synchronization of the camera network with the Ubisense tracking system was also evaluated using data shown in Figure 4.9. The data was collected when instantly pushing the target object along X axis to test the synchronization between the camera network and the Ubisense tracking system. The switching points of the camera network are compared against those of the UWB measurements, i.e. acceleration to move or deceleration to stop points. The switching points of UWB measurements were extracted as the follows: UWB measurements were manually partitioned into multiple motions as shown in Figure 4.10, then a line was fitted to each partition of data as shown in Figure 4.11, and then the switching points were extracted from the line intersections [61]. As can be seen in Figure 4.9, the synchronization is less than 0.1 sec between the camera network and the Ubisense tracking system.

4.4 Data Collection

Figure 4.12 shows a measurement tool built for these experiments. The white target circle is secured at the end of the metal ruler and the other end of the metal ruler is duct-taped with a

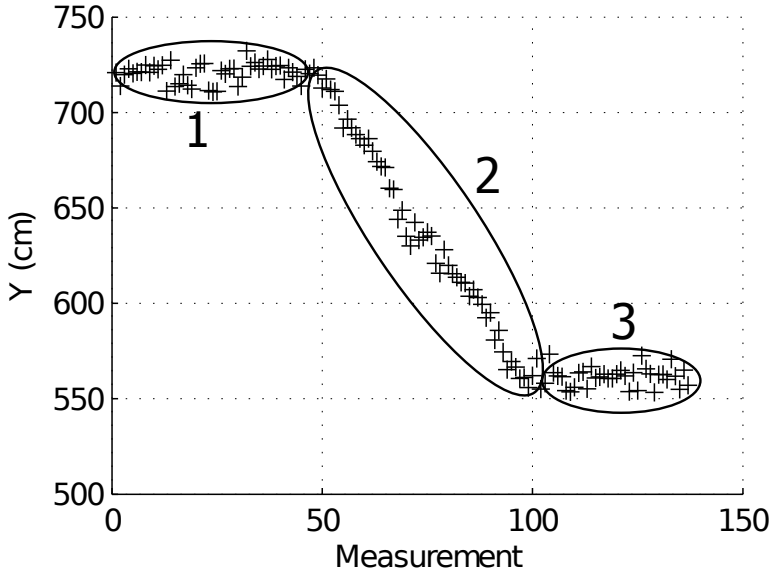

Figure 4.10: Raw measurement data. Ellipse 1 and 3 represents the object when stationary and ellipse 2 represents the object in motion.

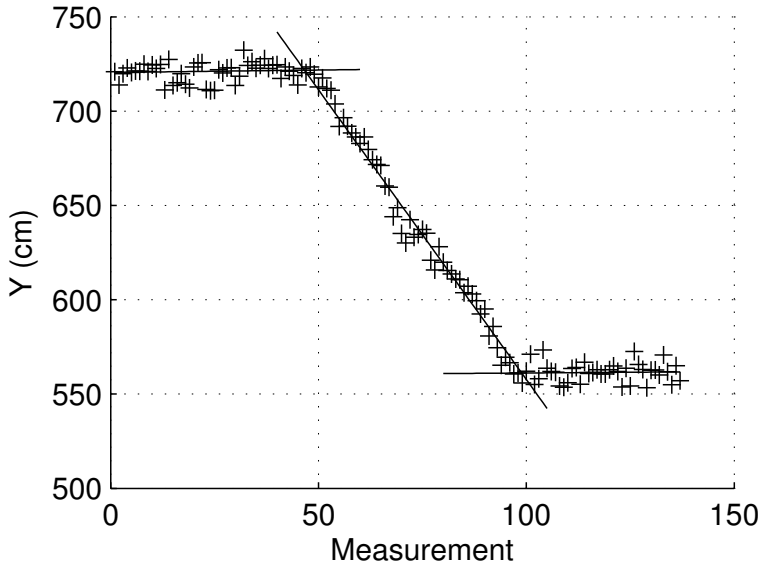

Figure 4.11: Three fitted lines on raw measurement data.

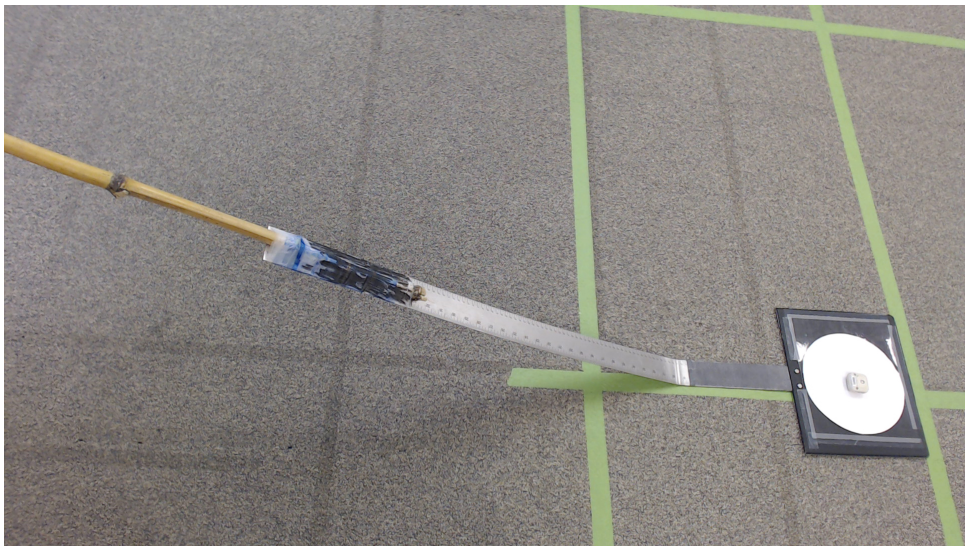

Figure 4.12: Measurement tool

Track name	Acceleration to motion	Deceleration to stop	Measurement RMSE (cm)
1	6	6	18.14
2	6	6	13.96
3	6	6	19.21
4	6	6	29.10
5	6	6	20.04

Table 4.2: Linear track data

bamboo stick. This setup ensures that the white target circle is about 1.5 m away from the bamboo stick end, and therefore it minimizes any camera occlusions of the while target circle by a user during the data collection. The metal ruler is bent about 20° near to the white target circle to facilitate tool manipulation.

Tracking data was collected while manually moving the measurement tool along pre-defined tracks. Figures 4.13a - 4.13b depict the five linear tracks tested. Ten trials were recorded for each track. The linear tracks start and finish at the rightmost point of each track and stop at each dot for about 10 seconds. Figures 4.13c - 4.13e depict more complex tracks that were tested. Fifteen trials were recorded for each track. In this case, the tracks start at either at the rightmost or right bottom point, and make one loop movement. The complex tracks also stop at each dot for about 10 seconds.

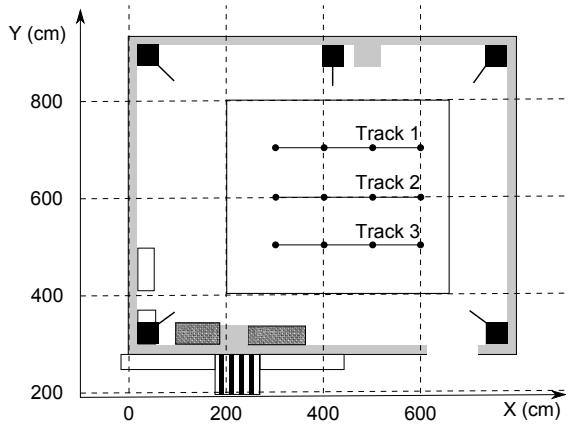

(a) Horizontal linear movement

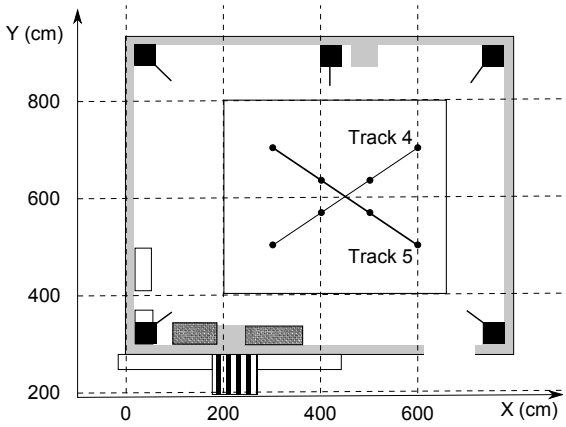

(b) Diagonal linear movement

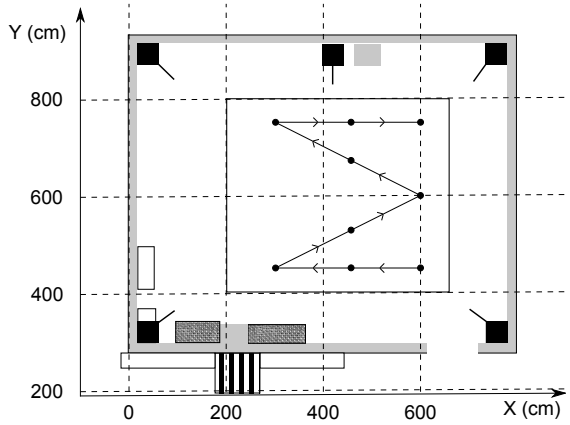

(c) M shape movement

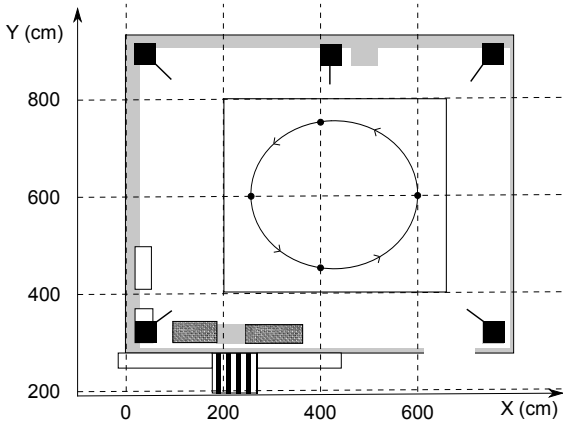

(d) Circle shape movement

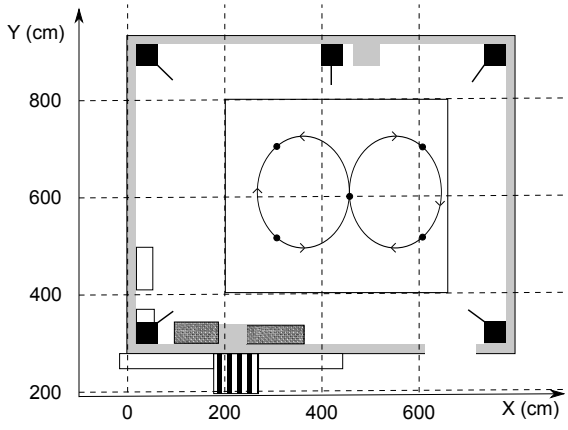

(e) Eight shape movement

Figure 4.13: Pre-defined track paths.

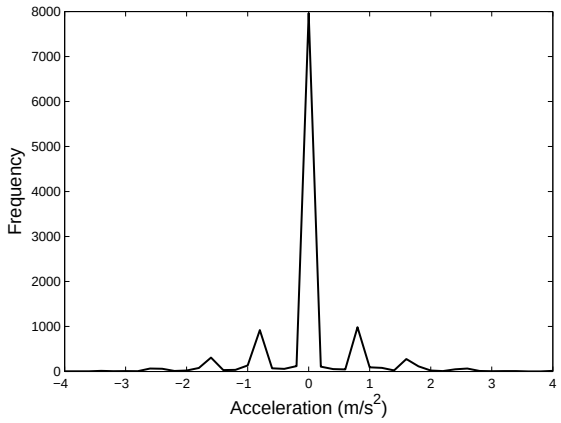

(a) Horizontal linear movement

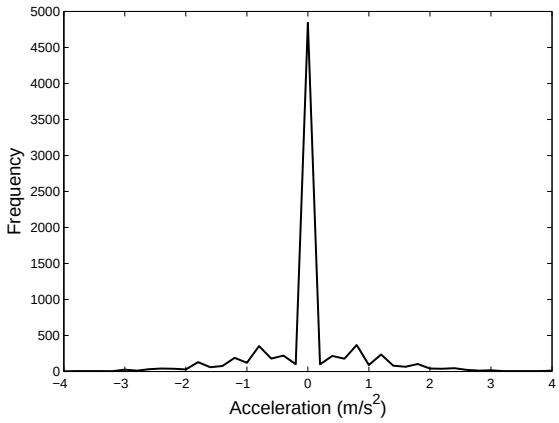

(b) Diagonal linear movement

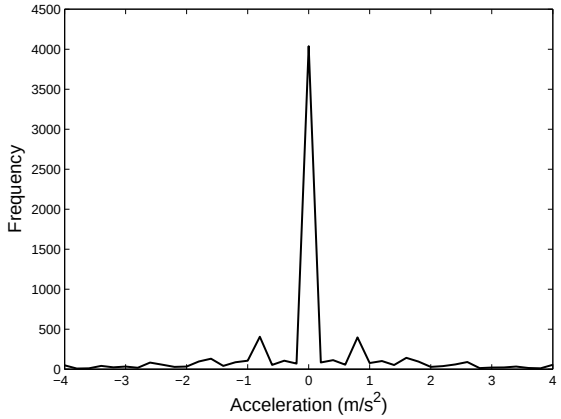

(c) M shape movement

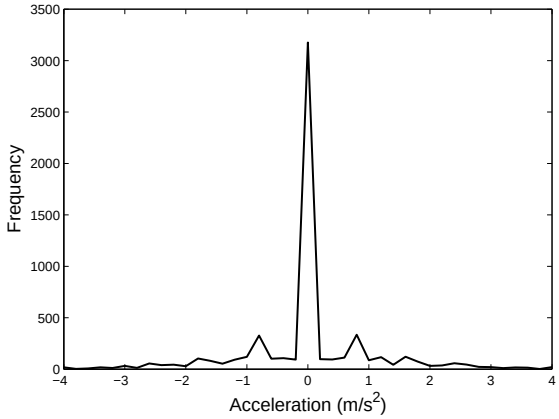

(d) Circle shape movement

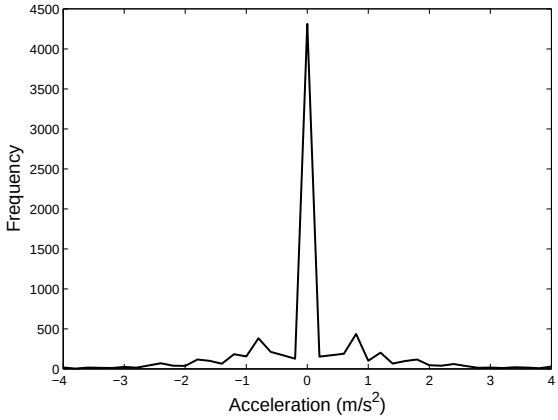

(e) Eight shape movement

Figure 4.14: Pre-defined track acceleration histograms

Track name	Acceleration to motion	Deceleration to stop	Measurement RMSE (cm)
M shape	8	8	24.86
Circle shape	4	4	31.58
Eight shape	6	6	23.86

Table 4.3: Complex track data

$\sigma_a(m/s^2)$	$\sigma_i(m/s^2)$	$\sigma_m(m)$
0.01	1.00	0.16

Table 4.4: Filter parameters

Tables 4.2 - 4.3 provide information about the collected data. The range of raw measurement error was 14 - 32 cm and each recording contains 4 - 8 dynamic impulses. Figure 4.14 shows their acceleration histograms. It can be seen that the histograms in Figure 4.14 exhibit multi-modality, similar to the histogram of CAVIAR walking data in Figure 2.4.

4.5 Filters

The asynchronous versions of three different types of filter were evaluated: the AKF, IMMF and IMMF-IR. The initial setup information of the applied filters is given in this section. It is assumed that the recorded human motion follows the constant velocity model and undergoes two different types of acceleration, typical and impulse accelerations. In addition, it is also assumed that each of two different accelerations can be modeled by a single Gaussian, and therefore they can be modeled by the proposed human motion model.

All the filters make use of the same assumptions in their models, and their parameters are primarily set by values in Table 4.4 unless otherwise mentioned. The initial states of all the filters are set using the first ground truth position (x_1,y_1) as in Equation 4.1, and the initial state covariances of filters are set using σ_a as described in Equation 4.2.

$$\mathbf{X}^0 = \begin{bmatrix} x_1 \\ 0 \\ y_1 \\ 0 \end{bmatrix} \tag{4.1}$$

$$\mathbf{P}^0 = \begin{bmatrix} 0 & 0 & 0 & 0 \\ 0 & \sigma_a^2 & 0 & 0 \\ 0 & 0 & 0 & 0 \\ 0 & 0 & 0 & \sigma_a^2 \end{bmatrix} \tag{4.2}$$

The AKF is initially set with dynamic noise equal to σ_a, and its window size is set to 40. The two models of the IMMF are constructed according to the previous assumptions with the transition probability of Equation 4.3. The model filters of the IMMF-IR are built using the matrix specified in Equation 4.4, where C is 5 and S is 5. Equation 4.5 shows the model transition probability of IMMF-IR.

$$\mathbf{p}_{ij} = \begin{bmatrix} 1 & 0 \\ 0 & 1 \end{bmatrix} \tag{4.3}$$

$$\mathbf{M}_{6\times5} = \begin{bmatrix} 0 & 0 & 0 & 0 & 0 \\ 1 & 0 & 0 & 0 & 0 \\ 0 & 1 & 0 & 0 & 0 \\ 0 & 0 & 1 & 0 & 0 \\ 0 & 0 & 0 & 1 & 0 \\ 0 & 0 & 0 & 0 & 1 \end{bmatrix} \tag{4.4}$$

$$\mathbf{p}_{ij} = \mathbf{I}_{6\times6} \tag{4.5}$$

4.6 Performance Analysis

The performance results of all the filters on the Ubisense tracking data are summarized in Table 4.5 and Table 4.6. The best performance figure for each track is marked in bold. It can be seen in the tables that the IMMF-IR has the best performance among all the applied filters. Its average percentage improvement relative to measurement RMSE is 16.54% as shown in Table 4.7, which is 2.83% higher than that of IMMF. In the following, the position estimates are analyzed in four different captured scenarios to demonstrate why the IMMF-IR worked the best.

Track name	RMSE (cm)			
	Measurement	AKF	IMMF	IMMF-IR
1	18.14	51.19	15.52	**14.53**
2	13.96	49.39	13.28	**12.33**
3	19.21	51.70	18.49	**18.22**
4	29.10	62.29	24.54	**23.63**
5	20.04	65.25	17.82	**17.33**
Average	20.09	55.96	17.93	**17.21**

Table 4.5: Filter performance on linear track data

Track name	RMSE (cm)			
	Measurement	AKF	IMMF	IMMF-IR
M shape	24.86	62.60	20.10	**19.79**
Circle shape	31.58	73.86	26.18	**25.19**
Eight shape	23.86	69.40	21.03	**20.57**
Average	26.77	68.62	22.44	**21.85**

Table 4.6: Filter performance on complex track data

	Measurement	AKF	IMMF	IMMF-IR
Average RMSE (cm)	23.25	61.96	20.06	**19.41**
Improvement (%)	0	-166.45	13.71	**16.54**

Table 4.7: Filter performance and percentage improvement

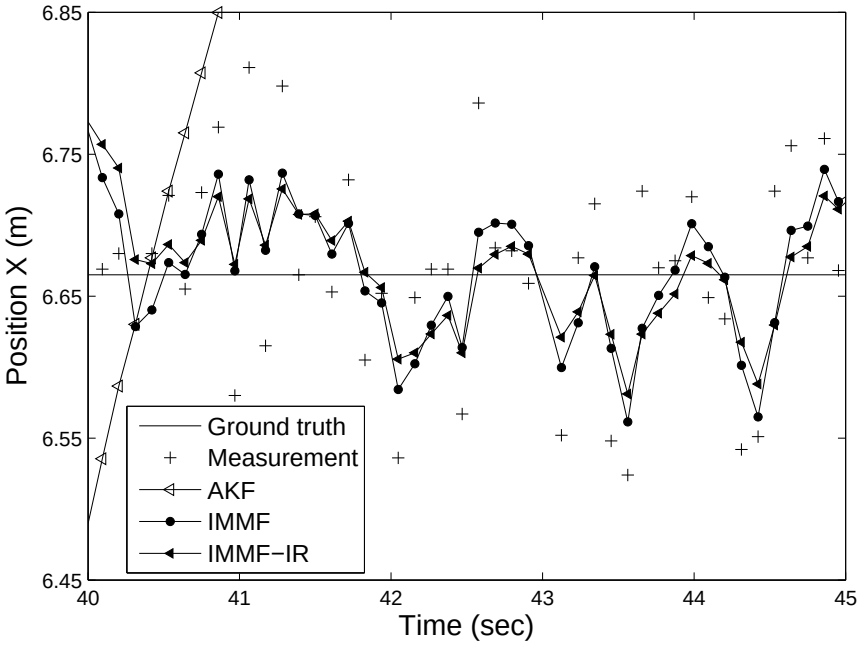

Figure 4.15: Filter position estimates when the human motion becomes stationary after a deceleration.

4.7 Filter Estimate Analysis

Figure 4.15 shows the position estimates of the three filters when the human motion remains stationary after deceleration. As shown in the figure, the IMMF-IR achieves the best performance, as its position estimate closely oscillates around the ground truth position after stabilization. The tendency of the position estimate of the IMMF is similar to the IMMF-IR, but its performance is slightly worse than that of IMMF-IR. On the other hand, the position estimate of the AKF overshoots and tries to get back to the trajectory after deceleration, and therefore it shows the worst performance. At the worst case scenario, the AKF diverges after a velocity changing point and generates a large performance error.

When human motion experiences velocity changes, i.e. deceleration, the performance of the IMMF is more sensitive to the magnitude of measurement noise around the velocity changing point than that of IMMF-IR. Figure 4.16 shows a case where the measurement noise is large around the deceleration point. As can be seen in the figure, both IMMF and IMMF-IR quickly adapt their position estimates to the ground truth position after the deceleration. The opposite scenario is shown in Figure 4.17. In this case, the IMMF fails to punctually detect the impulse change or

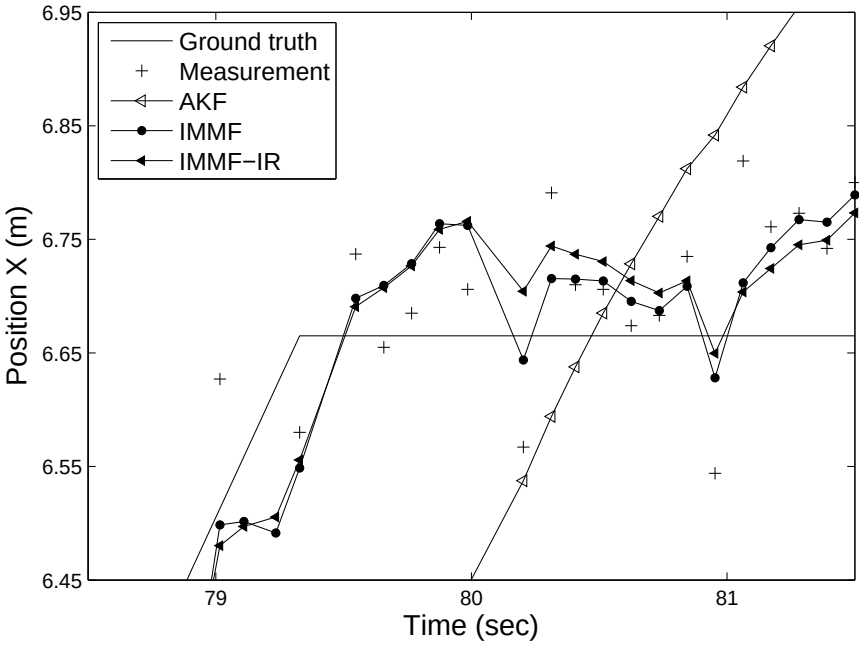

Figure 4.16: Filter position estimates. Human motion undergoes deceleration at 79.3 sec, and then remains stationary. Measurement noise is large around the deceleration point.

deceleration. Therefore, its performance worsens a lot around the deceleration point. However, the IMMF-IR more quickly adapts its position estimate to the ground truth position as shown in the figure.

An outlier can occur in UWB position tracking. Figure 4.18 shows an example of how the three filters respond to such a case. It can be observed from the figure that IMMF and IMMF-IR quickly recover their position estimates from the outlier, but the outlier creates a large error for both filters. This problem is further discussed in Chapter 6.

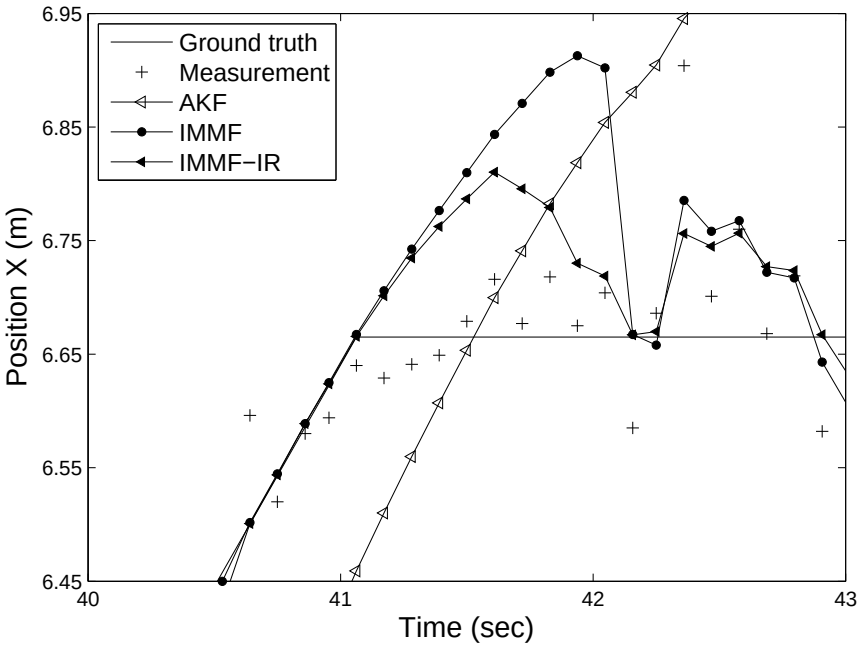

Figure 4.17: Filter position estimates. Human motion undergoes deceleration at 41 sec, and then remains stationary. Measurement noise is small around the deceleration point.

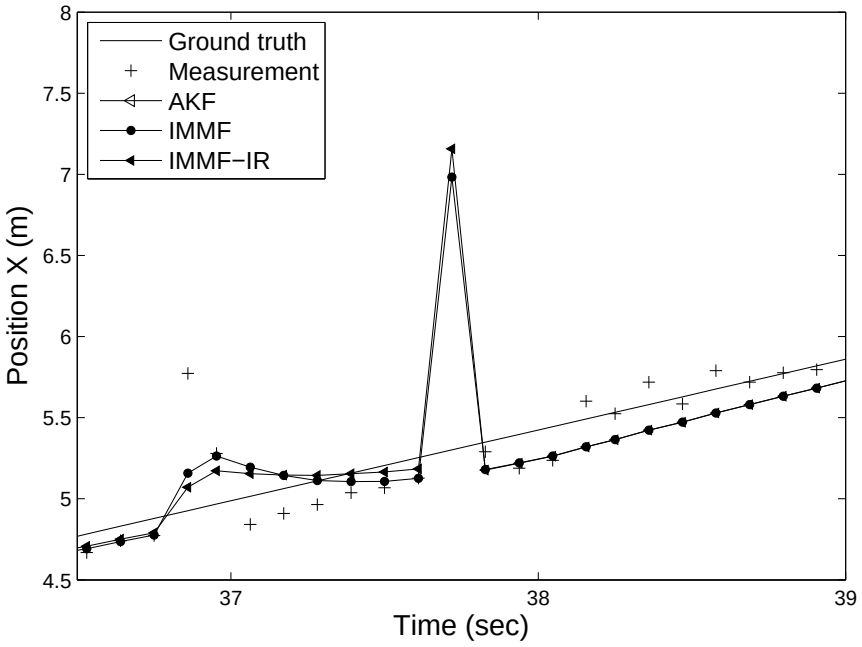

Figure 4.18: Filter position estimates. Human motion is at the constant velocity. Outlier in measurement appears at 37.7 sec.

Chapter 5

Power System State Estimation

This chapter explores the application of the new filter to a state estimation problem for a power system. Simulated power system data was generated that exhibits impulse-like spikes due to faults. The new filter was applied in an extended Kalman filter (EKF) to handle the non-linearity in the measurement process. A modified RMSE metric is defined and used for evaluation. Finally, the performance of the new filter on the simulated power system data is compared against existing methods.

5.1 Problem Description

State estimation can be used in electrical power grids to monitor the state of a power system and to provide inputs for other essential operations such as power security analysis [1, 32, 72]. Conventionally, the state estimation problem has been solved using the weighted least square (WLS) algorithm in which a single set of possibly noisy, asynchronous measurements is used to estimate the state of a power system [59]. However, the WLS algorithm ignores the dynamic characteristics of a power system, instead reinitializing at every iteration [32, 33, 68]. Recently, filter techniques have been applied which include the dynamic model of a system in their operations [26, 33, 68]. In filtering, the prediction of states is feasible due to this dynamic model and it is beneficial especially when some quantities cannot be easily measured. It can also be used to help detect anomalies such as abrupt faults or bad measurement data [32, 68].

Figure 5.1 shows a model of two alternating current (AC) power buses connected via a

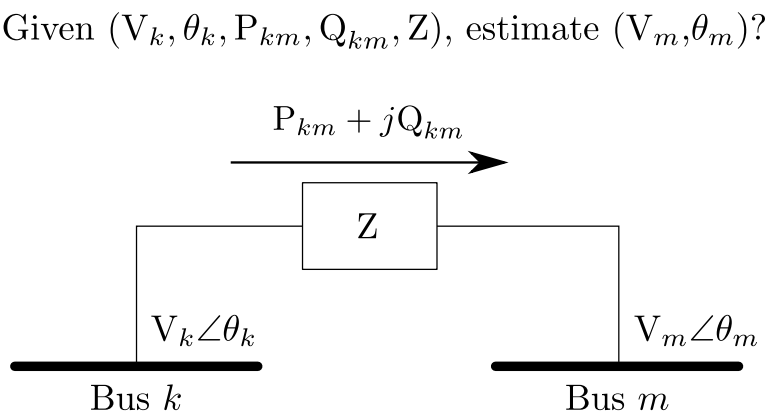

Figure 5.1: 2-bus power system and state estimation problem

.

transmission line [1]. In the figure, V_i and θ_i represent the voltage and phase at bus i, P_{km} and Q_{km} represent real and reactive power flows from bus k to bus m, and Z is the impedance of a transmission line between bus k and m. Figure 5.2 shows an example of normal voltage and phase signals.

Figure 5.1 illustrates the state estimation problem considered in this work. The objective of the problem is to estimate the voltage and phase at bus m (V_m, θ_m) while the real and reactive power flow (P_{km}, Q_{km}) are observed, even during a fault or grounded condition i.e. thunder. The fault appears as a sudden drop in voltage and phase. Figure 5.3 shows an example. The fault resembles an impulse in the dynamic noise. For this problem, it is assumed that (V_k, θ_k, Z) are provided as constants. Equation 5.1 formulates how the components in the figure are mathematically related to each other, where g_{km} is a real part of the impedance Z and b_{km} is an imaginary part of the impedance Z. Note that the measurements P_{km} and Q_{km} are non-linear functions of the unknown variables V_m and θ_m in the equations.

$$\begin{aligned} P_{km} &= V_k^2 g_{km} - V_k V_m g_{km} \cos(\theta_k - \theta_m) - V_k V_m b_{km} \sin(\theta_k - \theta_m) \\ Q_{km} &= -V_k^2 b_{km} + V_k V_m b_{km} \cos(\theta_k - \theta_m) - V_k V_m g_{km} \sin(\theta_k - \theta_m) \end{aligned} \tag{5.1}$$

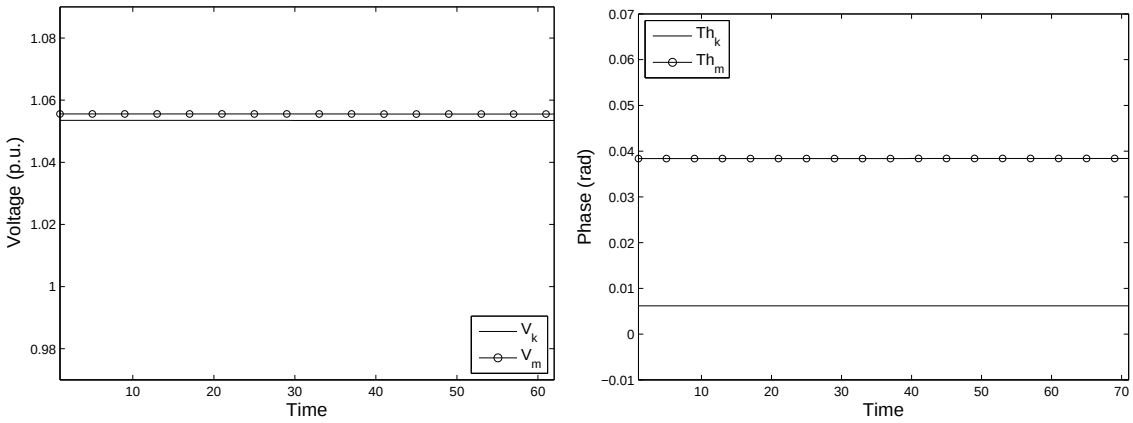

(a) Voltage (b) Phase

Figure 5.2: Normal voltage and phase signals.

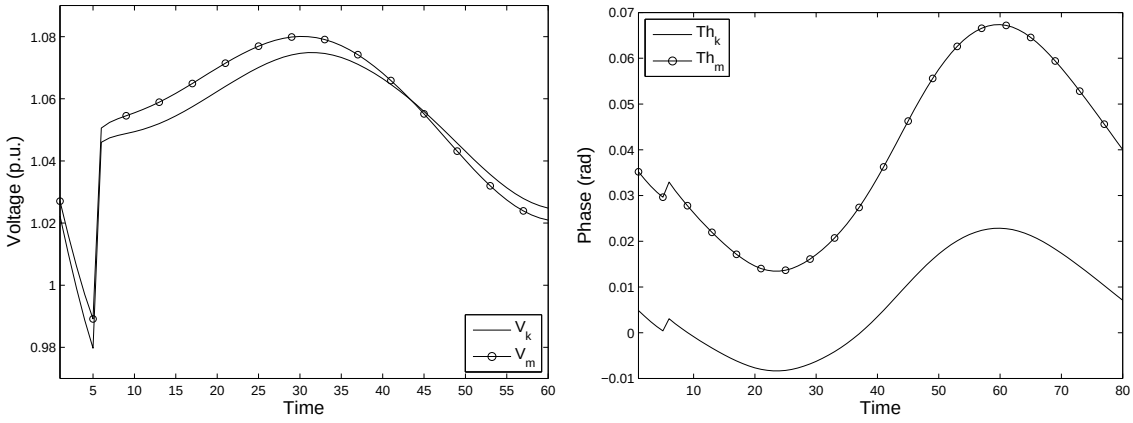

(a) Voltage (b) Phase

Figure 5.3: Voltage and phase signals with a fault near the beginning.

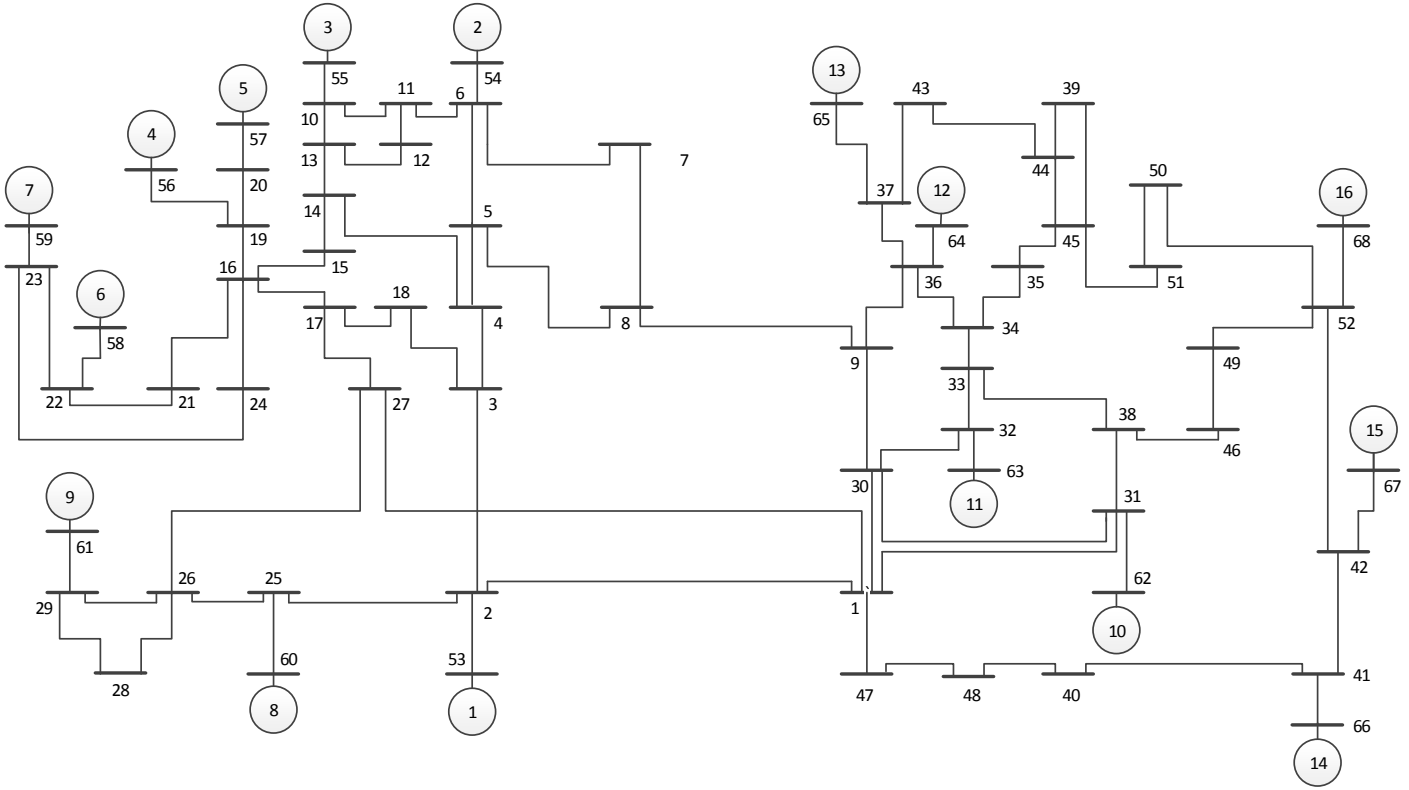

Figure 5.4: IEEE 16-machine 68-bus system. In the figure, a circle represents a generator, a thick horizontal bar represents a bus, and a line connecting two buses represents a transmission line.

5.2 Simulated Power System Data

Figure 5.4 shows the IEEE 16-machine 68-bus system [53]. It represents the simplified equivalent of the interconnected New England test system and New York power system. It consists of 83 pairwise interconnections between the buses. This means the data has 83 2-bus state estimation problems. This system was simulated in the Real-Time Power and Intelligent Systems Lab at Clemson University to generate simulated power system data using the real time digital simulator (RTDS) [39]. One fault is simulated in the beginning in the simulation. The data was collected at 30Hz for 3 seconds at each bus. In the data set, the voltages and phases (V,θ) are available at buses as the ground truth, and the real and reactive powers (P,Q) between buses are available as noise free measurements. The impedances Z between buses are also provided in the data set.

The measurement noise in a power system is known to be modeled by an additive zero mean Gaussian distribution as in Equation 5.2, where $\bar{\mathbf{z}}_t$ is an ideal measurement while $\mathbf{z}_t$ is a noisy measurement [1]. The standard deviation σ_m of the noise can be determined depending on the property of a chosen measurement device. In this work, a range of zero mean Gaussian noise was tested in order to evaluate the performance of the filter under various measurement conditions. An example of simulated noisy power measurements is shown in Figure 5.5 when $\sigma_m = 0.1$.

$$\mathbf{z}_t = \bar{\mathbf{z}}_t + N(0, \sigma_m^2) \tag{5.2}$$

The data set was analyzed to evaluate if the voltage and phase signals in the data can be modeled by the proposed dynamic model in Section 2.2. For this purpose, the second derivatives of the voltage and phase signals were computed and the histogram of them was calculated as shown in Figure 5.6. From this figure it can be seen that there is a small but noticeable multimodal distribution caused by the faults. Hence, the voltage and phase signals can be modeled by the proposed dynamic model.

5.3 Extended Kalman Filter

This section explains the sequential steps of the EKF algorithm. It is worth noting that these sequential steps of the algorithm are simplified to deal with only a nonlinearity in the measurement process. The prediction of the algorithm is shown in Equation 5.3. It is the same as the Kalman filter

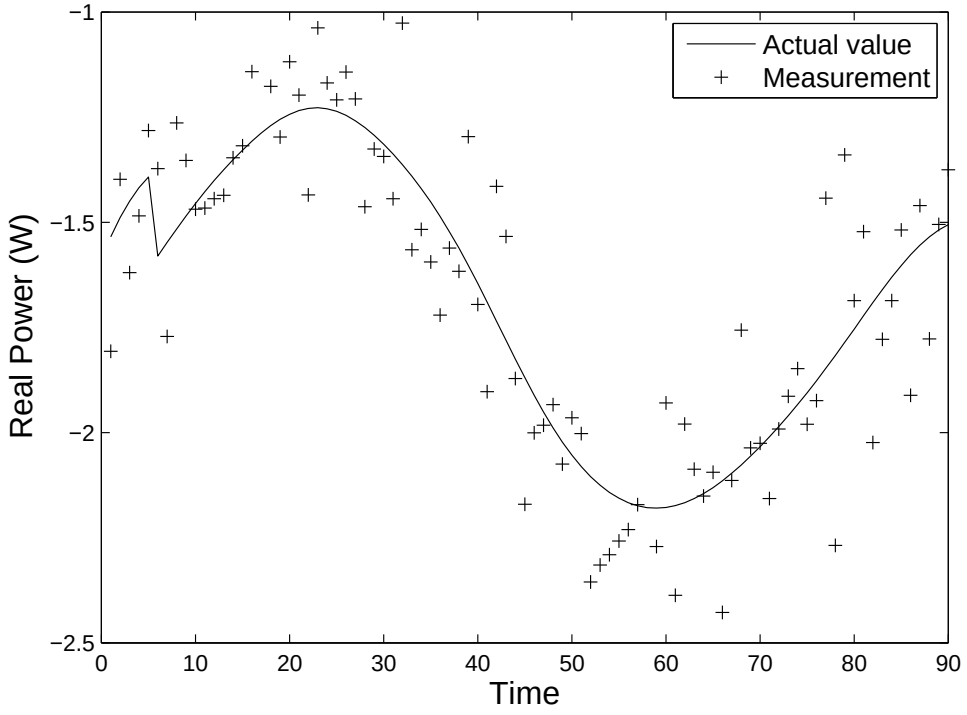

(a) Real power

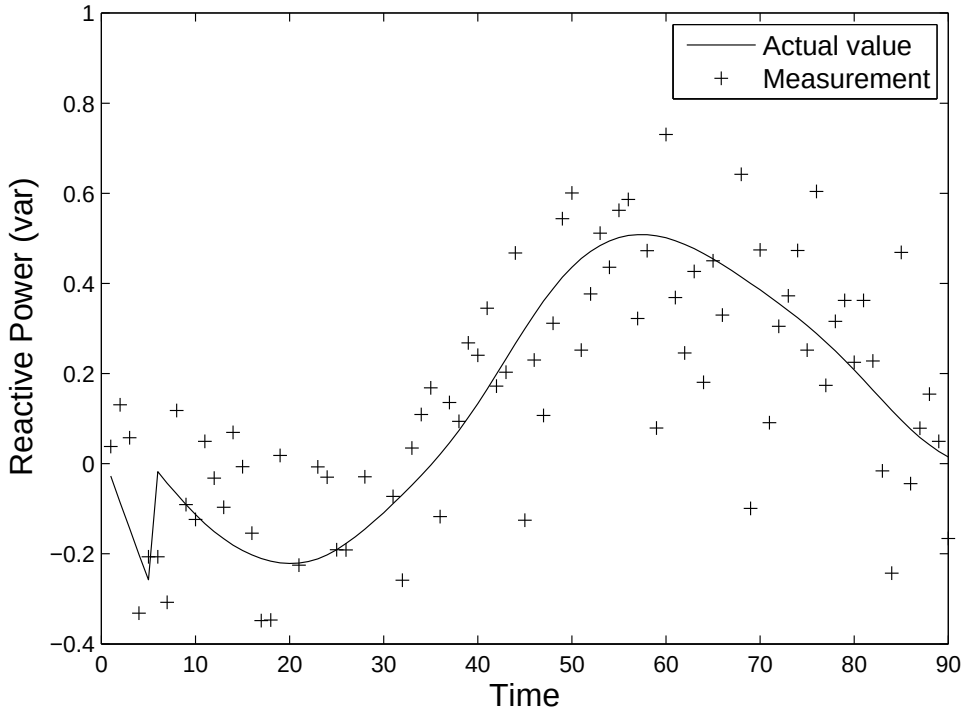

(b) Reactive power

Figure 5.5: Real and reactive power measurements. Zero mean Gaussian noise with $\sigma = 0.1$ is added to the original noiseless power measurements.

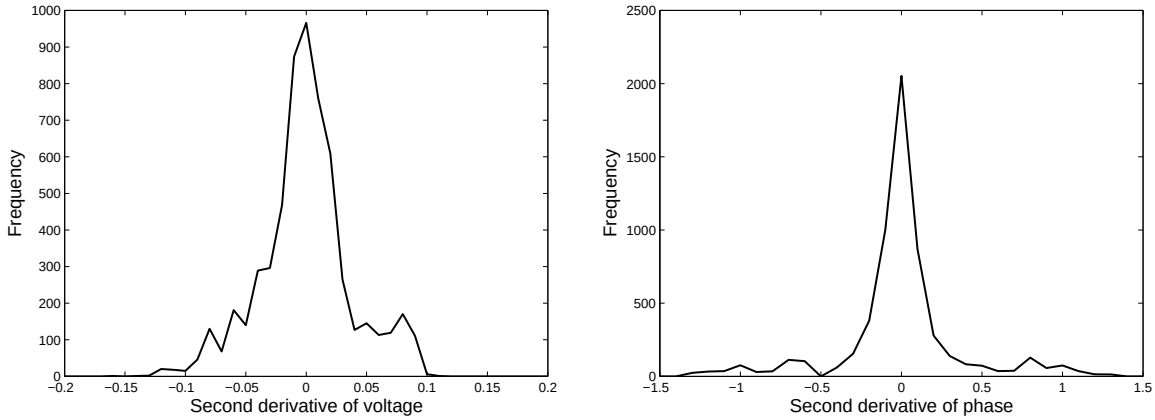

(a) Voltage (b) Phase

Figure 5.6: Histograms of second derivatives of voltage and phase.

algorithm because it is assumed that the state transition process is linear. The algorithm computes a Jacobian matrix $\mathbf{J_H}$ using the most recent estimate $\hat{\mathbf{X}}_t^-$ as in Equation 5.4, which is defined as the derivative of the measurement function $\mathbf{g}(\cdot)$ with respect to the state $\mathbf{X}$. Subsequently, the Kalman gain is computed using Equation 5.5 and the algorithm updates the state vector as shown in Equation 5.6.

$$\begin{aligned} \hat{\mathbf{X}}_t^- &= \Phi\hat{\mathbf{X}}_{t-1} \\ \hat{\mathbf{P}}_t^- &= \Phi\hat{\mathbf{P}}_{t-1}\Phi^{\mathrm{T}} + \mathbf{Q} \end{aligned} \tag{5.3}$$

$$\mathbf{J_H} = \frac{\partial \mathbf{g}_t(\hat{\mathbf{X}}_t^-)}{\partial \mathbf{X}_t} \tag{5.4}$$

$$\mathbf{K}_t = \hat{\mathbf{P}}_t^- \mathbf{J}_\mathbf{H}^{\mathrm{T}} [\mathbf{J_H}\hat{\mathbf{P}}_t^- \mathbf{J}_\mathbf{H}^{\mathrm{T}} + \mathbf{R}]^{-1} \tag{5.5}$$

$$\begin{aligned} \hat{\mathbf{X}}_t &= \hat{\mathbf{X}}_t^- + \mathbf{K}_t(\mathbf{z}_t - \mathbf{J_H}\hat{\mathbf{X}}_t^-) \\ \hat{\mathbf{P}}_t &= [\mathbf{I} - \mathbf{K}_t\mathbf{J_H}]\hat{\mathbf{P}}_t^- \end{aligned} \tag{5.6}$$

$\sigma_{\mathrm{V}a}$	$\sigma_{\mathrm{V}i}$	$\sigma_{\theta\mathrm{a}}$	$\sigma_{\theta\mathrm{i}}$	σ_m
0.0005	0.005	0.007	0.7	0.2 - 7

Table 5.1: Filter parameters

5.4 Error Metric

This chapter uses the RMSE between ideal measurements $\bar{\mathbf{z}}$ and estimated measurements $\hat{\mathbf{z}}$ as the error metric. It is calculated using Equation 5.7. In this way, the quality of two separate state estimates $\hat{\mathrm{V}}$ and $\hat{\theta}$ can be jointly evaluated in one measure whose unit is available. Estimated measurements $\hat{\mathbf{z}}$ or $(\hat{\mathrm{P}}, \hat{\mathrm{Q}})$ can be computed from state vector estimates using Equation 5.1. The RMSE was computed 100 times on 100 different datasets to compute the average RMSE for each measurement noise standard deviation σ_m. A relative improvement to a measurement RMSE will be used to compare the performances of filters, which is a similar performance measure as the performance index used in [68].

$$\mathrm{RMSE} = \sqrt{\frac{1}{\mathrm{N}} \sum_{i=1}^{\mathrm{N}} (\bar{\mathbf{z}}_i - \hat{\mathbf{z}}_i)^{\mathrm{T}} (\bar{\mathbf{z}}_i - \hat{\mathbf{z}}_i)} \tag{5.7}$$

5.5 Filters

The AKF, IMMF, and IMMF-IR were applied on 83 state estimation problems of the simulated power system data. Their parameters are primarily configured by the values in Table 5.1 where $\sigma_{\mathrm{V}a}$ and $\sigma_{\theta\mathrm{a}}$ represent typical dynamic noise standard deviations for voltage and phases, and $\sigma_{\mathrm{V}i}$ and $\sigma_{\theta\mathrm{i}}$ represent impulse dynamic noise standard deviations for voltages and phases. The range of measurement noise standard deviation σ_m is selected so that it covers 3 - 120% of the ideal measurement magnitude standard deviation. The initial states of all the filters are set using the first ground truth (V_1,θ_1) as in Equation 5.8. The initial state covariances of filters are set using the typical dynamic noise as described in Equation 5.9.

$$\mathbf{X}^0 = \begin{bmatrix} \mathrm{V}_1 \\ 0 \\ \theta_1 \\ 0 \end{bmatrix} \tag{5.8}$$

$$\mathbf{P}^0 = \begin{bmatrix} 0 & 0 & 0 & 0 \\ 0 & \sigma^2_{\mathrm{V}a} & 0 & 0 \\ 0 & 0 & 0 & 0 \\ 0 & 0 & 0 & \sigma^2_{\theta\mathrm{a}} \end{bmatrix} \tag{5.9}$$

The AKF is initially set with the typical dynamic noise, and its window size is set to 10. The two models of the IMMF are constructed according to the proposed dynamic model with the transition probability of Equation 5.10. The model filters of the IMMF-IR are built using the matrix specified in Equation 5.11, where C is 100 and S is 100. Equation 5.12 shows the model transition probability of IMMF-IR.

$$\mathbf{p}_{ij} = \begin{bmatrix} 1 & 0 \\ 0 & 1 \end{bmatrix} \tag{5.10}$$

$$\mathbf{M}_{101\times100} = \begin{bmatrix} 0 & 0 & 0 & 0 & 0 & \cdots & 0 \\ 1 & 0 & 0 & 0 & 0 & \cdots & 0 \\ 0 & 1 & 0 & 0 & 0 & \cdots & 0 \\ \vdots & \vdots & \vdots & \vdots & \vdots & \ddots & 0 \\ 0 & 0 & 0 & 0 & 0 & \cdots & 1 \end{bmatrix} \tag{5.11}$$

$$\mathbf{p}_{ij} = \mathbf{I}_{101\times101} \tag{5.12}$$

5.6 Performance Analysis

Figure 5.7 summarizes the performances of AKF, IMMF, and IMMF-IR in terms of a percentage improvement relative to measurement RMSE. In the range of $\sigma_m = 0.2 - 1.0$, which is the typical range of measurement noise for this problem, the IMMF-IR shows the best performance. Interestingly, although the AKF performs the worst in the beginning of the tested σ_m range, it starts performing better than the other two filters after $\sigma_m = 3$, suggesting that in the presence of very noisy measurement devices it would be the best filter.

To show an example, the voltage and phase estimates of the filters at bus 12 are plotted in Figure 5.8 when $\sigma_m = 0.3$. The estimates are captured only around the fault because this is when

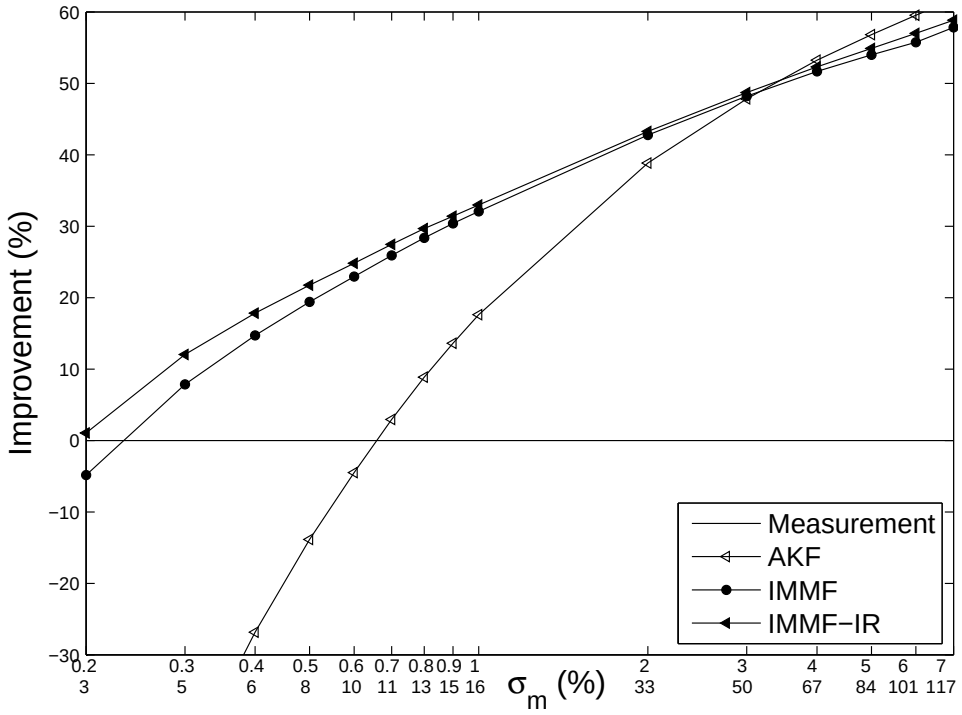

Figure 5.7: Summary of filter performances on various σ_m. The first row of the X labels represents real values used in the simulation while the second row of the X labels represents their percentages relative to the ideal measurement magnitude standard deviation.

the filters have the most difference. As depicted in the figure, the response of the IMMF-IR to the fault is slightly faster than that of the IMMF even though overall they both adapt to the fault. On the other hand, the AKF has the slowest response time among the filters.

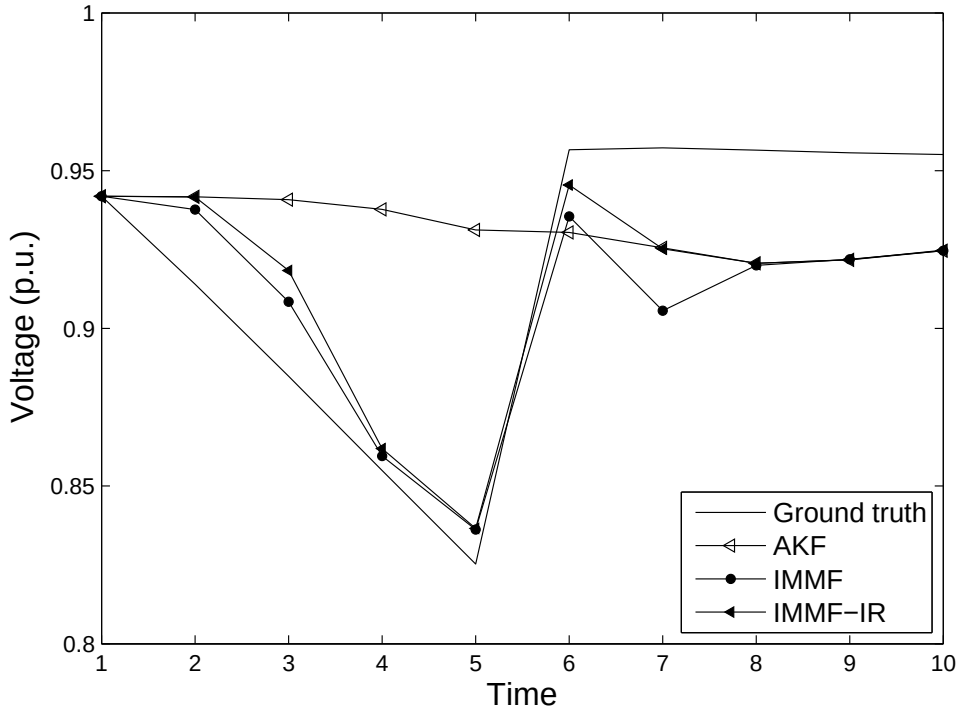

(a) Voltage

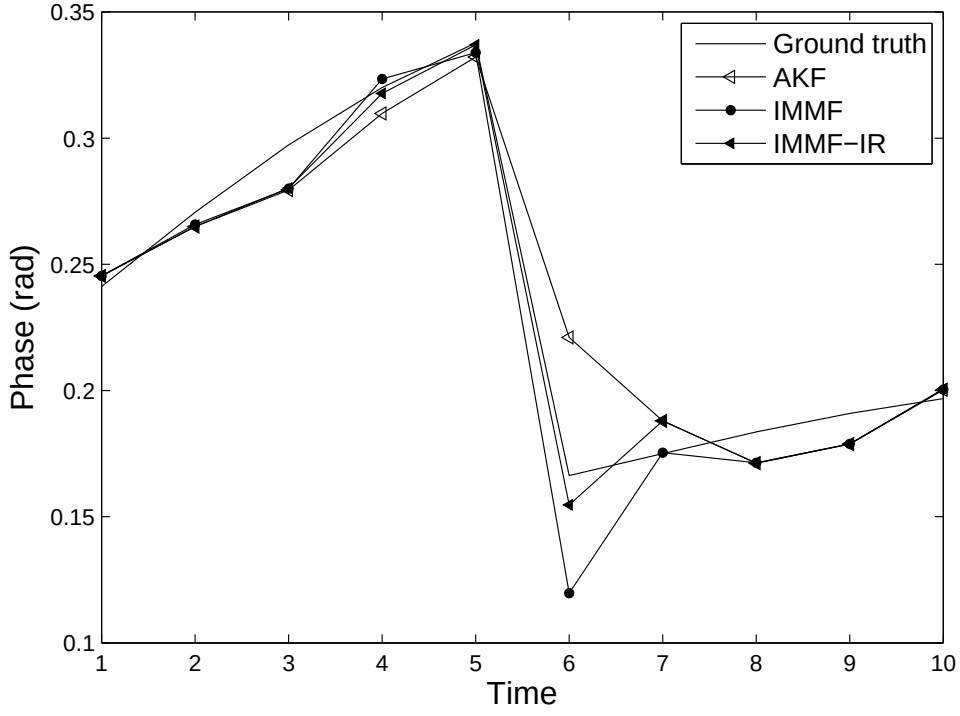

(b) Phase

Figure 5.8: Voltage and phase estimates at bus 12 when $\sigma_m = 0.3$

Chapter 6

Measurement Outliers

The ideas in this dissertation were developed to address impulses in dynamic noise. This chapter explores if the same idea can be applied to measurement noise. Outliers are a well-studied phenomenon and can be detected and eliminated by a number of methods, such as RANSAC [23]. This chapter considers the possibility that an outlier could be modeled as an impulse in measurement noise. First, the appearance of measurement noise in real UWB tracking data is investigated. Then a measurement model is developed incorporating an impulse component. A filter algorithm that implements the new measurement model is developed in the Kalman filter framework. Finally, the performances of the MMKF filters integrated with the new measurement model on the UWB tracking data are compared against the previous results.

6.1 Investigation of Measurement Error

In this section, the measurement errors of the UWB tracking data are analyzed. The histogram of the measurement errors was calculated using ground truth positions versus raw measurements and is shown in Figure 6.1a. Figure 6.1b shows a zoomed view of the histogram with one standard deviation σ marked as two vertical dashed lines. Note that this standard deviation is usually used in filtering to set up a measurement covariance. From the figure, it can be seen that outliers appear with greater frequency than would be suggested by a unimodal distribution. This motivated the development of a model that specifies an outlier component.

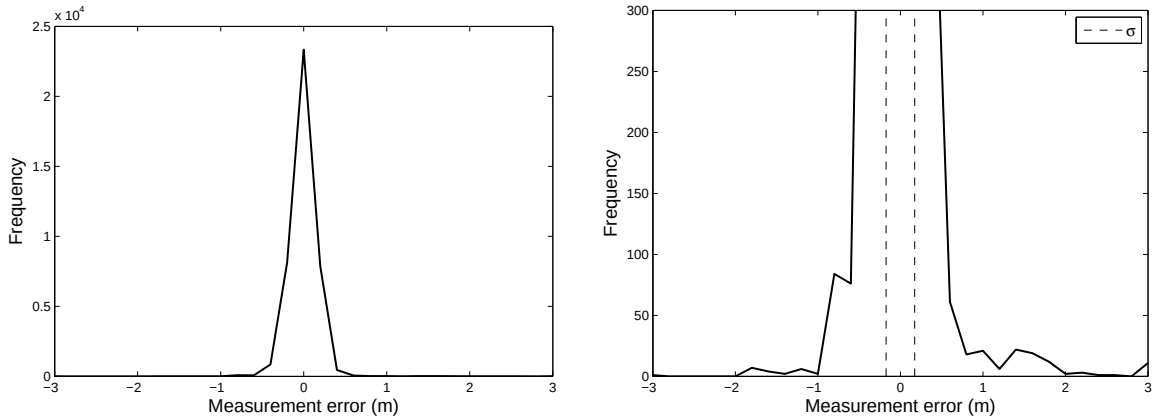

(a) Histogram

(b) Histogram with zoom-in

Figure 6.1: Measurement error histogram of UWB tracking data (X axis)

6.2 Proposed Measurement Model

As before, a constant velocity model is used to explain a state transition process as shown in Equation 6.1 where x represents a 1D position and $\dot{x}$ represents a 1D velocity. Equation 6.2 represents the proposed measurement model for a measurement process where k represents a measurement noise state and z is a 1D position measurement. This measurement model assumes that measurements are additively corrupted by noise and the measurement process switches between typical measurement noise state ($k = 0$) and outlier measurement noise state ($k = 1$). The proposed model can also be extended to two dimensions by duplication.

There are four parameters $(q_n, \sigma_a, \sigma_m, \sigma_o)$ in the equations. The parameter q_n is a probability of remaining in a typical measurement noise state given that a previous state is also a typical measurement noise state. The parameters σ_a, σ_m, and σ_o represent standard deviations of dynamic noise, typical measurement noise, and outlier measurement noise, respectively.

$$\begin{aligned} x_t &= x_{t-1} + \dot{x}_{t-1}\Delta t \\ \dot{x}_t &= \dot{x}_{t-1} + N(0, \sigma_a^2) \end{aligned} \tag{6.1}$$

$$
\begin{aligned}
k_t &= \begin{cases} 0 & \text{if } k_{t-1} = 1 \text{ or } \mathrm{U}[0,1] \leq q_n \\ 1 & \text{otherwise} \end{cases} \\
z_t &= \begin{cases} x_t + N(0, \sigma_m^2) & \text{if } k_t = 0 \\ x_t + N(0, \sigma_o^2) & \text{if } k_t = 1 \end{cases}
\end{aligned}
\tag{6.2}
$$

6.3 Kalman Filter with Outlier Handling

This section explains an algorithm that implements the proposed measurement model in the Kalman filter framework. The fundamental idea is that the filter estimates a measurement noise state k based on the probability of the innovation $\mathbf{i}$. The innovation represents the difference between the predicted and actual measurements. It is highly likely that the magnitude of an innovation is in a certain range during the operation of filtering. However, when an outlier occurs, the magnitude of the innovation gets extremely large and the probability of having that innovation becomes low. Hence, whenever the probability of an innovation is less than a certain threshold, it can be assumed that the measurement process is in the outlier measurement noise state ($k = 1$). The equations to compute an innovation and its covariance are shown in Equation 6.3. The probability of an innovation can be computed using Equation 6.4.

$$
\begin{aligned}
\mathbf{i}_t &= \mathbf{z}_t - \mathbf{H}\hat{\mathbf{X}}_t^- \\
\mathbf{C}_t &= \mathbf{H}\hat{\mathbf{P}}_t^-\mathbf{H}^{\mathrm{T}} + \mathbf{R}
\end{aligned}
\tag{6.3}
$$

$$
\Lambda_t = p(\mathbf{i}_t | \mathcal{N}(\mathbf{0}, \mathbf{C}_t)) \tag{6.4}
$$

Algorithm 3 shows how the concept of the new filter is implemented in the Kalman filter framework. The most important part of the algorithm is excerpted in Equation 6.5. In the equation, $\mathrm{P}_{\min}$ is a minimum innovation probability to be classified as a typical measurement noise state while c is a pre-defined constant for an outlier measurement noise state. c controls how the Kalman filter responds to outlier noise measurements by adjusting the new measurement covariance $\mathbf{R}'$, i.e. the

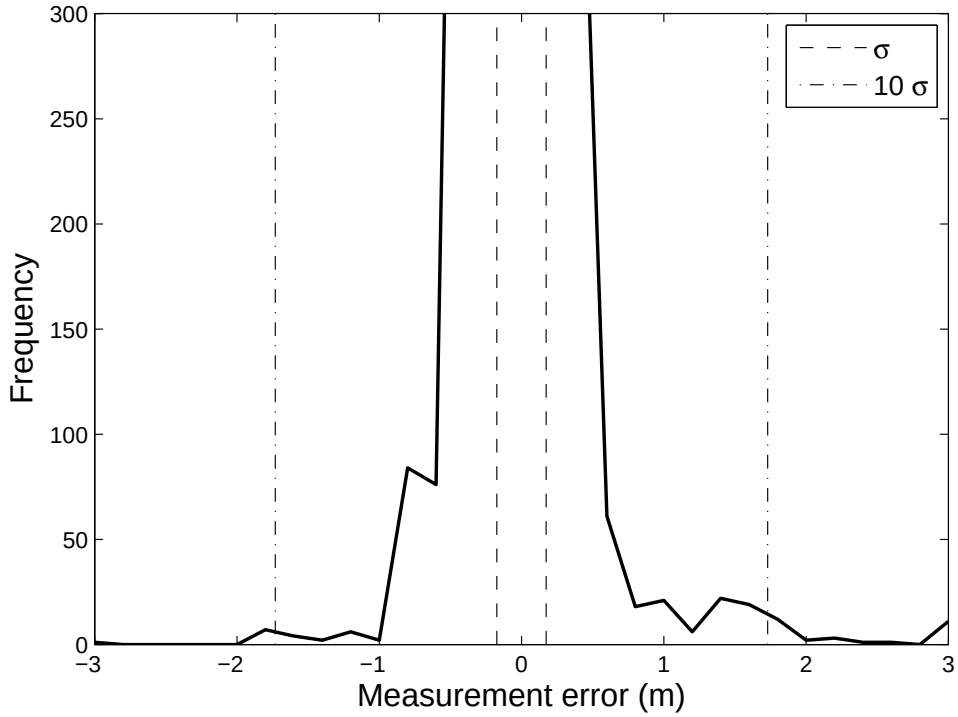

Figure 6.2: Measure error histogram of UWB tracking data (X axis)

higher the constant c is, the more likely the filter is to give lower weight to the measurement. In other words, the Kalman gain determines the balance between a predicted state and measurement based on the ratio of dynamic noise covariance and measurement noise covariance and this balance can be adjusted by scaling the original measurement covariance as shown in Equation 6.5.

$$
\begin{aligned}
k_t &= \begin{cases} 0 & \text{if } \Lambda_t \geq \mathrm{P}_{\min} \\ 1 & \text{otherwise} \end{cases} \\
\mathbf{R}' &= \begin{cases} \mathbf{R} & \text{if } k = 0 \\ c\mathbf{R} & \text{if } k = 1 \end{cases}
\end{aligned}
\tag{6.5}
$$

Figure 6.2 illustrates two standard deviations located in the measurement error histogram of the UWB tracking data when $c = 100$, which means 10 times a measurement noise standard deviation for outlier handing. As shown in the figure, $c = 100$ is reasonable since 10σ covers the

Algorithm 3 KF with Outlier Handling algorithm

(a) Compute a predicted state $\hat{\mathbf{X}}_t^-$ and its covariance $\hat{\mathbf{P}}_t^-$.

$$\begin{aligned} \hat{\mathbf{X}}_t^- &= \Phi \mathbf{X}_{t-1}^0 \\ \hat{\mathbf{P}}_t^- &= \Phi \mathbf{P}_{t-1}^0 \Phi^{\mathrm{T}} + \mathbf{Q} \end{aligned} \tag{6.6}$$

where, Φ is a state transition matrix, and $\mathbf{Q}$ is a dynamic noise covariance.

(b) Obtain a measurement $\mathbf{z}_t$.

(c) Compute an innovation $\mathbf{i}_t$ and its covariance $\mathbf{C}_t$.

$$\begin{aligned} \mathbf{i}_t &= \mathbf{z}_t - \mathbf{H}\hat{\mathbf{X}}_t^- \\ \mathbf{C}_t &= \mathbf{H}\hat{\mathbf{P}}_t^-\mathbf{H}^{\mathrm{T}} + \mathbf{R} \end{aligned} \tag{6.7}$$

where, $\mathbf{H}$ is an observation matrix, and $\mathbf{R}$ is a typical measurement noise covariance.

(d) Compute an innovation probability Λ_t.

$$\Lambda_t = p(\mathbf{i}_t | \mathcal{N}(\mathbf{0}, \mathbf{C}_t)) \tag{6.8}$$

(e) Determine a new measurement noise covariance $\mathbf{R}'$.

$$\begin{aligned} k_t &= \begin{cases} 0 & \text{if } \Lambda_t \geq \mathrm{P}_{\min} \\ 1 & \text{otherwise} \end{cases} \\ \mathbf{R}' &= \begin{cases} \mathbf{R} & \text{if } k_t = 0 \\ c\mathbf{R} & \text{if } k_t = 1 \end{cases} \end{aligned} \tag{6.9}$$

where, $\mathrm{P}_{\min}$ is a minimum innovation probability, and c is a pre-defined constant for outlier measurement noise state.

(f) Compute a Kalman gain $\mathbf{K}_t$.

$$\mathbf{K}_t = \hat{\mathbf{P}}_t^-\mathbf{H}^{\mathrm{T}}[\mathbf{H}\hat{\mathbf{P}}_t^-\mathbf{H}^{\mathrm{T}} + \mathbf{R}']^{-1} \tag{6.10}$$

(g) Compute an updated state $\hat{\mathbf{X}}_t$ and its covariance $\hat{\mathbf{P}}_t$.

$$\begin{aligned} \hat{\mathbf{X}}_t &= \hat{\mathbf{X}}_t^- + \mathbf{K}_t(\mathbf{z}_t - \mathbf{H}\hat{\mathbf{X}}_t^-) \\ \hat{\mathbf{P}}_t &= [\mathbf{I} - \mathbf{K}_t\mathbf{H}]\hat{\mathbf{P}}_t^- \end{aligned} \tag{6.11}$$

local peaks in the tail of the histogram.

P_{min}	c	$\sigma_a(m/s^2)$	$\sigma_i(m/s^2)$	$\sigma_m(m)$
10^{-10}	100	0.01	1.00	0.16

Table 6.1: Filter parameters

Track name	RMSE (cm)			
	Measurement	AKF	IMMF	IMMF-IR
1	18.14	51.19	15.48 (-0.04)	**14.53** (0.00)
2	13.96	49.39	13.28 (0.00)	**12.33** (0.00)
3	19.21	51.70	18.49 (0.00)	**18.22** (0.00)
4	29.10	62.29	23.78 (-0.76)	**22.52** (-1.11)
5	20.04	65.25	16.54 (-1.28)	**16.47** (-0.86)
Average	20.09	55.96	17.51 (-0.42)	**16.81** (-0.40)

Table 6.2: Filter performance on linear track data. The numbers in the parentheses ( ) represent the difference between the previous and current performances, and minus sign means an improvement from a previous performance.

6.4 Filters

The asynchronous versions of AKF, IMMF, and IMMF-IR were applied on the UWB tracking data as in Chapter 4. The IMMF and IMMF-IR filters were further extended to handle outlier measurement noise using the new filter algorithm. Their parameters are listed in Table 6.1. The extension of the AKF to handle outlier measurement noise was not considered here because its dynamic noise covariance is adaptive in nature and thus computing a stable innovation probability is impossible. All other initial conditions, setups, and assumptions are the same as in Section 4.5.

6.5 Performance Analysis

The performance results of all the filters on the UWB tracking data are summarized in Table 6.2 and Table 6.3. Their overall percentage improvement is also shown in Table 6.4. It can be seen that the filters with the outlier handling extension achieve better performance than before. Specifically, the performance of IMMF has been improved about 4.28 % and the performance of IMMF-IR has been improved about 4.12 %.

The position estimates of IMMF and IMMF-IR are also depicted before and after the outlier handling in Figure 6.3 and Figure 6.4. As shown in Figure 6.3b, the responses of IMMF and IMMF-IR to the outlier measurement have been significantly reduced. However, Figure 6.4 shows the

Track name	RMSE (cm)			
	Measurement	AKF	IMMF	IMMF-IR
M shape	24.86	62.60	19.95 (-0.15)	**19.81** (0.02)
Circle shape	31.58	73.86	22.83 (-3.35)	**21.97** (-3.22)
Eight shape	23.86	69.40	20.47 (-0.56)	**20.01** (-0.56)
Average	26.77	68.62	21.08 (-1.36)	**20.60** (-1.25)

Table 6.3: Filter performance on complex track data. The numbers in the parentheses ( ) represent the difference between the previous and current performances, and minus sign means an improvement from a previous performance.

Outlier handling	Average RMSE (cm)			
	Measurement	AKF	IMMF	IMMF-IR
Before	23.25	61.96	20.06	**19.41**
After	23.25	61.96	19.20	**18.61**
Improvement (%)	0	0	4.28	4.12

Table 6.4: Filter performances improvement

opposite scenario. In the figure, the behaviors of IMMF on the outlier measurement do not show much difference before and after the outlier handling. This may be due to the presence of multiple consecutive outliers in the same neighborhood, which could be caused by either a measurement impulse or a dynamic impulse. On the other hand, IMMF-IR mitigates the outlier measurement in this case.

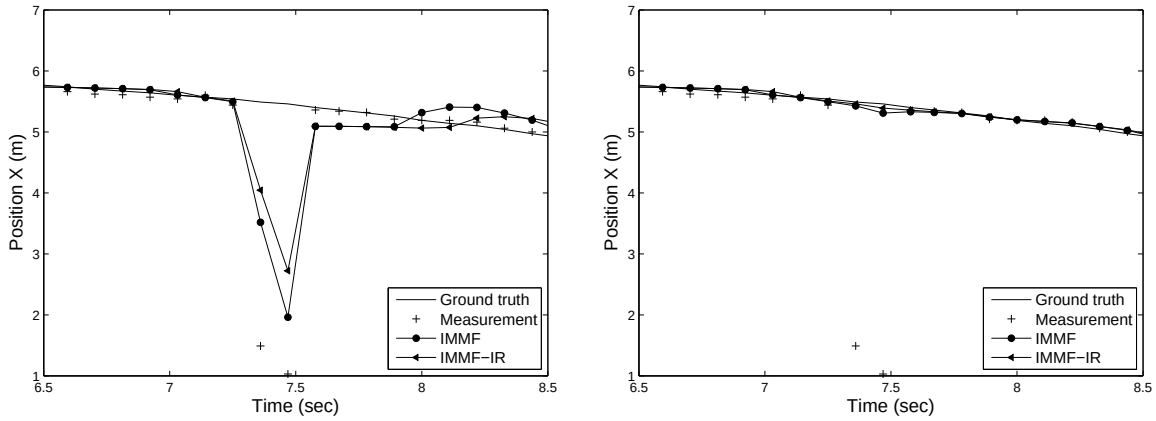

(a) Before (b) After

Figure 6.3: A successful example of filtering a measurement outlier using an impulse model

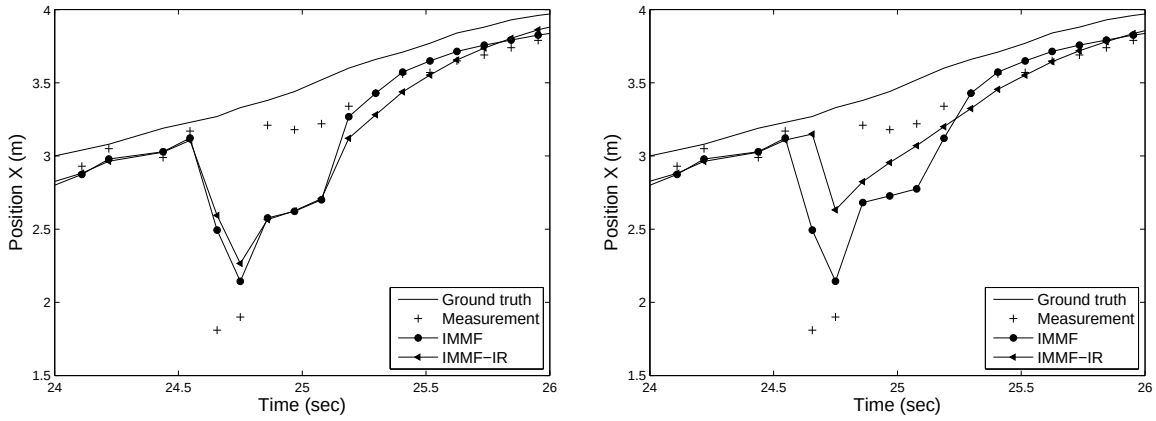

(a) Before (b) After

Figure 6.4: An unsuccessful example of filtering two consecutive measurement outliers, possibly due to their initial resemblance to a dynamic impulse.

Chapter 7

Conclusions

This dissertation investigated the possibility of an impulse model in dynamic noise in the presence of large measurement noise. By analyzing some real 2D human tracking data, it was experimentally demonstrated that human motion can exhibit a multimodal distribution caused by occasional impulses in velocity. A new dynamic model was proposed to model this phenomenon. A new filter that implements the new dynamic model was developed in the MMKF framework. Its performance was initially evaluated using simulations to test its efficacy across a wide range of measurement and dynamic noises. In these experiments, the new filter showed about 4% improvement over existing methods.

The performance of the new filter was examined for two different applications. First, UWB tracking data was collected in the Riggs test facility using a camera network system to measure ground truth. The performance of the new filter on the UWB tracking data was measured. The new filter showed the best performance among the applied filters with about 2.8% average improvement over existing methods. Second, the new filter was applied on a power system state estimation problem using simulated power system data obtained from the Real-Time Power and Intelligent Systems Laboratory at Clemson University. Its performance was evaluated over the typical range of measurement noise standard deviations. In this case, the new filter showed about 4% relative improvement.

Finally, the idea of the impulse model in dynamic noise was extended to measurement noise to address outlier measurements. A new measurement model was proposed to model the outlier measurement noise, and then an outlier handling algorithm was developed using the pro-

posed measurement model. The new filter with the outlier handling algorithm was applied on the UWB tracking data again. The performances of the applied filters have been improved about 4.2% compared to the previous performances.

7.1 Future Works

Further work could investigate the performance of the IMMF-IR in other contexts. For example, the core of the problem in this dissertation is how to detect and respond to an impulse in dynamic motion. It may be interesting to investigate the relation of IMMF-IR to classic impulse response filters in other domains of digital signal processing.

Acronyms

AKF Adaptive Kalman filter

AMM Autonomous multiple model

AOA Angle of arrival

EKF Extended Kalman filter

GNSS Global navigation satellite system

GPB Generalized pseudo Bayesian

GPS Global positioning system

IMMF Interacting multiple model filter

IMMF-IR Interacting multiple model filter with impulse response

IMU Inertial measurement unit

INS Inertial navigation system

KF Kalman filter

LPS Local positioning system

MMKF Multiple-model Kalman filter

MMKF-IR Multiple model Kalman filter with impulse response

NLOS Non-line of sight

RF Radio frequency

RMSE Root mean square error

TDOA Time difference of arrival

TOA Time of arrival

UWB Ultra-wide band

WLS Weighted least square

Bibliography

[1] A. Abur and A. Exposito. *Power system state estimation: theory and implementation.* CRC Press, January 2004.

[2] G. Ackerson and K. Fu. On state estimation in switching environments. *IEEE Trans. on Automatic Control*, 15(1):10–17, February 1970.

[3] A. Almagbile, J. Wang, and W. Ding. Evaluating the performances of adaptive Kalman filter methods in GPS/INS integration. *Journal of Global Positioning Systems*, 9(1):33–40, 2010.

[4] M. Arulampalam, S. Maskell, N. Gordon, and T. Clapp. A tutorial on particle filters for online nonlinear non-Gaussian Bayesian tracking. *IEEE Trans. on Signal Processing*, 50(2):174–188, February 2002.

[5] S. Banerjee. *Improving Accuracy in Ultra-Wideband Indoor Position Tracking through Noise Modeling and Augmentation.* PhD thesis, Clemson University, December 2012.

[6] L. Bao and S. Intille. Activity recognition from user-annotated acceleration data. *Pervasive Computing*, 3001:1–17, 2004.

[7] C. Barrios, H. Himberg, Y. Motai, and A. Sadek. Multiple model framework of adaptive extended Kalman filtering for predicting vehicle location. *IEEE Intelligent Transportation Systems Conference*, pages 1053–1059, September 2006.

[8] A. Bayat, M. Pomplun, and D. Tran. A study on human activity recognition using accelerometer data from smartphones. *Procedia Computer Science*, 34:450–457, 2014.

[9] P. Blom. An efficient filter for abruptly changing systems. *IEEE Conf. on Decision and Control*, pages 656–658, December 1984.

[10] Y. Boers and J. Driessen. Interacting multiple model particle filter. *IEE Proc. of Radar, Sonar and Navigation*, 150(5):344–349, October 2003.

[11] P. Bokare and A. Maurya. Acceleration-deceleration behaviour of various vehicle types. Technical report, Indian Institute of Technology, Guwahati, India, July 2014.

[12] P. Casale, O. Pujol, and P. Radeva. Human activity recognition from accelerometer data using a wearable device. *Pattern Recognition and Image Analysis*, 6669:289–296, 2011.

[13] C. Chang and M. Athans. State estimation for discrete systems with switching parameters. *IEEE Trans. on Aerospace and Electronic Systems*, 14(3):418–425, May 1978.

[14] DataGenetics. World's fastest man. `http://datagenetics.com/blog/july32013/index.html`, July 2013.

[15] B. Davies. Satellite based on-board vehicle navigation system including predictive filtering and map-matching to reduce errors in a vehicular position. U.S. Patent 6,615,135 B2, September 2003.

[16] J. Diaz, R. de A Maues, R. Soares, E. Nakamura, and C. Figueiredo. Bluepass: an indoor bluetooth-based localization system for mobile applications. *IEEE Symposium on Computer and Communications*, pages 778–783, June 2010.

[17] W. Ding, J. Wang, and C. Rizos. Improving adaptive Kalman estimation in GPS/INS integration. *Journal of Navigation*, 60(3):517–529, September 2007.

[18] H. Durrant-Whyte. Multisensor data fusion. Technical report, The University of Sydney, NSW 2006 Australia, January 2001.

[19] H. Dyckmanns, R. Matthaei, M. Maurer, B. Lichte, J. Effertz, and D. Stuker. Object tracking in urban intersections based on active use of a priori knowledge: Active interacting multi model filter. *IEEE Intelligent Vehicles Symposium*, pages 625–630, June 2011.

[20] K. El Mokhtari, S. Reboul, M. Azmani, and J. Choquel. A circular interacting multi-model filter applied to map matching. *Int'l Conf. on Information Fusion*, pages 1473–1478, July 2013.

[21] M. Farmer, R. Hsu, and A. Jain. Interacting multiple model (IMM) Kalman filters for robust high speed human. *International Conf. on Pattern Recognition*, 2:20–23, 2002.

[22] FCC. Revision of part 15 of the commissions rules regarding ultra-wideband transmission systems. Report and order, adopted February 14, 2002, released July 15, 2002.

[23] M. Fischler and R. Bolles. Random sample consensus: a paradigm for model fitting with applications to image analysis and automated cartography. *Communications of the ACM*, 24(6):381–395, June 1981.

[24] R. Fisher. CAVIAR Test Case Scenarios. `http://groups.inf.ed.ac.uk/vision/CAVIAR/CAVIARDATA1/`, May 2011.

[25] D. Ganjali. Filtering noise caused by sensor selection for an ultra-wide band position tracking system. Master's thesis, Clemson University, December 2009.

[26] E. Ghahremani and I. Kamwa. Dynamic state estimation in power system by applying the extended Kalman filter with unknown inputs to phasor measurements. *IEEE Trans. on Power Systems*, 26(4):2556 – 2566, June 2011.

[27] O. Haraz. Why do we need ultra-wideband? `http://www.vlsiegypt.com/home/?p=518`, November 2012.

[28] A. Hero, C. Kreucher, and K. Kastella. Multiple model particle filtering for multi-target tracking. Technical report, Electrical and Computer Engineering, University of Michigan, Ann Arbor, MI, December 2004.

[29] C. Hide, T. Moore, and M. Smith. Adaptive Kalman filtering for low cost INS/GPS. *Journal of Navigation*, 56(1):143–152, January 2003.

[30] A. Hoover and B. D. Olsen. A real-time occupancy map from multiple video streams. *IEEE International Conf. on Robotics and Automation*, 3:2261 – 2266, May 1999.

[31] C. Hu, W. Chen, Y. Chen, and D. Liu. Adaptive Kalman filtering for vehicle navigation. *Journal of Global Positioning Systems*, 2(1):42–47, November 2003.

[32] Y.-F. Huang, S. Werner, J. Huang, N. Kashyap, and V. Gupta. State estimation in electric power grids: Meeting new challenges presented by the requirements of the future grid. *IEEE Signal Processing Magazine*, 29(5):33 – 43, September 2012.

[33] Z. Huang, K. Schneider, and J. Nieplocha. Feasibility studies of applying Kalman filter techniques to power system dynamic state estimation. *International Power Engineering Conference*, pages 376 – 382, December 2007.

[34] M. Isard and A. Blake. A mixed-state condensation tracker with automatic model-switching. *Int'l Conf. on Computer Vision*, pages 107–112, January 1998.

[35] J. Jordan, N. Hirsenkorn, F. Klanner, and M. Kleinsteuber. Vehicle mass estimation based on vehicle vertical dynamics using a multi-model filter. *Int'l Conf. on Intelligent Transportation Systems*, pages 2041–2046, October 2014.

[36] S. Julier and J. Uhlmann. Unscented filtering and nonlinear estimation. *Proc. of the IEEE*, 92(3):401–422, March 2004.

[37] R. Kalman. A new approach to linear filtering and prediction problems. *Journal of Fluids Engineering*, 82(1):35–45, March 1960.

[38] Y. Kim and K. Hong. An IMM algorithm for tracking maneuvering vehicles in an adaptive cruise control environment. *Int'l Journal of Control, Automation, and Systems*, 2(3):310–318, September 2004.

[39] R. Kuffel, J. Giesbrecht, T. Maguire, R. Wierckx, and P. McLaren. RTDS-a fully digital power system simulator operating in real time. *IEEE WESCANEX 95. Communications, Power, and Computing. Conference Proceedings*, 2:300 – 305, May 1995.

[40] W. Lechner and S. Baumann. Global navigation satellite systems. *Computers and Electronics in Agriculture*, 25(1):67–85, January 2000.

[41] J. Lee and S. Choi. Through-material propagation characteristic and time resolution of UWB signal. *Int'l Workshop on Ultra Wideband Systems*, pages 71–75, May 2004.

[42] L. Letham. *GPS Made Easy: Using Global Positioning Systems in the Outdoors*. Mountaineers Books, 5th edition edition, May 2008.

[43] X. Li and V. Jilkov. Survey of maneuvering target tracking. Part V. multiple-model methods. *IEEE Trans. on Aerospace and Electronic Systems*, 41(4):1255–1321, October 2005.

[44] H. Liu, H. Darabi, P. Banerjee, and J. Liu. Survey of wireless indoor positioning techniques and systems. *IEEE Trans. on Systems, Man, and Cybernetics*, 37(6):1067–1080, November 2007.

[45] J. Liu, R. Chen, and T. Logvinenko. A theoretical framework for sequential importance sampling with resampling. In A. Doucet, N. de Freitas, and N. Gordon, editors, *Sequential Monte Carlo Methods in Practice*, Statistics for Engineering and Information Science, pages 225–246. Springer New York, 2001.

[46] D. Magill. Optimal adaptive estimation of sampled stochastic processes. *IEEE Trans. on Automatic Control*, 10(4):434–439, October 1965.

[47] J. Mantyjarvi, J. Himberg, and T. Seppanen. Recognizing human motion with multiple acceleration sensors. *IEEE Int'l Conf. on Systems, Man, and Cybernetics*, 2:747–752, October 2001.

[48] E. Mazor, A. Averbuch, Y. Bar-Shalom, and J. Dayan. Interacting multiple model methods in target tracking a survey. *IEEE Trans. on Aerospace and Electronic Systems*, 34(1):103–123, January 1998.

[49] S. McGinnity and G. W. Irwin. Multiple model bootstrap filter for maneuvering target tracking. *IEEE Trans. on Aerospace and Electronic systems*, 36(3):1006–1012, July 2000.

[50] R. Mehra. On the identification of variances and adaptive Kalman filtering. *IEEE Trans. on Automatic Control*, 15(2):175–184, April 1970.

[51] A. Mohamed and K. Schwarz. Adaptive Kalman filtering for INS/GPS. *Journal of Geodesy*, 73(4):193–203, May 1999.

[52] NSTB/WAAS T&E Team. Global positioning system (GPS) standard positioning service (SPS) performance analysis report. Technical report, William J. Hughes Technical Center, Atlantic City International Airport, NJ 08405, July 2014.

[53] B. Pal and B. Chaudhuri. *Robust Control in Power Systems*. Springer Science & Business Media, July 2006.

[54] B. Parkinson and J. Spilker. *Global Positioning System: Theory and Applications*. The American Institute of Aeronautics and Astronautics, 1st edition edition, January 1996.

[55] V. Pavlovic, J. Rehg, and J. MacCormick. Learning switching linear models of human motion. *Annual Conference on Neural Information Processing Systems*, pages 981–987, 2000.

[56] H. Qi and J. Moore. Direct Kalman filtering approach for GPS/INS integration. *IEEE Trans. on Aerospace and Electronic Systems*, 38(2):687–693, April 2002.

[57] N. Samama. *Global Positioning: Technologies and Performance*. Wiley-Interscience, 1st edition edition, March 2008.

[58] M. Scherhaufl, M. Pichler, E. Schimback, D. Muller, A. Ziroff, and A. Stelzer. Indoor localization of passive UHF RFID tags based on phase-of-arrival evaluation. *IEEE Trans. on Microwave Theory and Techniques*, 61(12):4724–4729, November 2013.

[59] F. Schweppe and J. Wildes. Power system static-state estimation, part i: Exact model. *IEEE Transactions on Power Apparatus and Systems*, PAS-89(1):120 – 125, January 1970.

[60] O. Shimizu, K. Tenmoku, Y. Doi, and K. Mito. Vehicle location detecting system. U.S. Patent 5,119,301, June 1992.

[61] W. Suski. *A Study of Environment Noise in Ultra-Wideband Indoor Position Tracking*. PhD thesis, Clemson University, May 2012.

[62] W. Suski, S. Banerjee, and A. Hoover. System-level noise of an ultra-wideband tracking system. *Int'l Conf. on Information Science, Signal Processing and their Applications*, pages 634–639, July 2012.

[63] S. Taghipour, M. Meybodi, and A. Taghipour. An algorithm for map matching for car navigation system. *Int'l Conf. on Information and Communication Technologies: From Theory to Applications*, pages 1–5, April 2008.

[64] P. Turaga, R. Chellappa, V. Subrahmanian, and O. Udrea. Machine recognition of human activities: A survey. *IEEE Trans. on Circuits and Systems for Video Technology*, 18(11):1473–1488, September 2008.

[65] Ubisense Inc. Series 7000 compact tag. http://www.ubisense.net/en/media/pdfs/products_pdf/uk/80553_series_7000_compact_tag.pdf.

[66] Ubisense Inc. Series 7000 ip sensors. http://www.ubisense.net/en/media/pdfs/products_pdf/uk/29512_series_7000_ip_sensors_combined.pdf.

[67] Ubisense Inc. System infrastructure. http://www.ubisense.net/en/media/pdfs/products_pdf/uk/76493_smart_factory_technology_english.pdf.

[68] G. Valverde and V. Terzija. Unscented Kalman filter for power system dynamic state estimation. *IET Generation, Transmission, and Distribution*, 5(1):29 – 37, January 2011.

[69] J. Wang, M. Stewart, and M. Tsakiri. Online stochastic modeling for INS/GPS integration. *Int'l Technical Meeting of the Satellite Division of The Institute of Navigation*, pages 1887–1896, September 1999.

[70] G. Welch and G. Bishop. An introduction to the Kalman filter. Technical report, University of North Carolina at Chapel Hill, Chapel Hill, NC, USA, 1995.

[71] S. Weng, C. Kuo, and S. Tu. Video object tracking using adaptive Kalman filter. *Journal of Visual Communication and Image Representation*, 17(6):1190–1208, December 2006.

[72] F. Wu. Power system state estimation: a survey. *Internation Journal of Electrical Power and Energy Systems*, 12(2):80 – 87, April 1990.

[73] K. Wu, J. Xiao, Y. Yi, D. Chen, X. Luo, and L. Ni. CSI-based indoor localization. *IEEE Trans. on Parallel and Distributed Systems*, 24(7):1300–1309, July 2012.

[74] L. Yang and G. Giannakis. Ultra-wideband communications: an idea whose time has come. *IEEE Signal Processing Magazine*, 21(6):26–54, November 2004.

[75] K. Yu, N. Watson, and J. Arrillaga. An adaptive Kalman filter for dynamic harmonic state estimation and harmonic injection tracking. *IEEE Trans. on Power Delivery*, 20(2):1577–1584, April 2005.